Use and Fabrication of Microfluidic Circuits Formed with Submerged Microjets

LTJG Nicholas Stovall-Kurtz, United States Navy
Hertford College
Oxford University
Department of Engineering Science

Supervised by Dr. Edmond Walsh

Thesis submitted to fulfill the requirements for the degree MSc of Engineering Science (by Research)

TABLE OF CONTENTS

1 Abstract

We have developed a method to fabricate microfluidic circuits that facilitate static and dynamic assays in cell biology. These microfluidic arrangements are made on standard tissue-culture Petri dishes in a manner analogous to pressure washing a patio: a submerged impinging microjet (SIM) of bioinert, transparent, and gas-permeable fluorocarbon (FC-40) displaces a dish-wetting aqueous solution (typically cell media) in any predetermined 2D pattern. The media left wetting the substrate is now uniquely confined by liquid FC-40 (not solid!) walls in the desired circuit pattern. SIM fabrication brings many benefits to biomedical scientists including rapid fabrication from familiar materials, real-time circuit accessibility, excellent optics (there are no solid walls to obscure an observer's view), bubble-free operation, and – most importantly – easy incorporation into existing workflows. SIM-printing provides great control over the fabrication resolution of microfluidic circuits and is studied first in this thesis. Varying user input parameters such as microjet velocity, flow rate, and height above the substrate provides a thorough validation of SIM-printing and highlights its resolution limitations. The main focus of this thesis, however, is studying flows *inside* SIM-printed circuits. In our bodies, cells are often bathed in flowing interstitial liquids. Therefore, to assay cell activity *in vitro* accurately, we need to predict flows precisely. As these circuits have fluid walls that morph during flow in accordance with changes in local pressure, we develop an analytical solution to this new flow problem and validate it experimentally. The unique liquid-liquid interface between commonly used aqueous-based cell media solutions and FC-40 is also examined in an effort to determine slip characteristics and effective interfacial tensions.

Acknowledgements

I have grown as a student, a researcher, and a person thanks to following:

To my supervisor Dr. Edmond Walsh, who patiently guided me to find *explanations*, not merely answers. You challenged me to discover deeper meaning, to question myself, and to simplify complex problems to fundamental principles. Your supervision will be missed.

To Dr. Peter Cook, who graciously allowed me to share his laboratory spaces. Your priceless biological perspective to my research and your passion for perfection have led to countless hours of enlightening, and entertaining, conversation.

To Cyril, my laboratory partner, my training partner, and my friend. Our combined pursuit to be the best versions of ourselves has proven to me there is no limit to what we can accomplish. To Cristian, who has led by example and was always available to lend a helping hand. To Federico, whose addition to the lab has brought smiles and friendship that will last a lifetime. Cyril, Cristian, and Federico, my happiest memories at Oxford revolve around you.

2 Introduction

2.1 What is Microfluidics?

The rapidly growing interdisciplinary field of microfluidics is typically comprised of fluid application on the length scale of tens to hundreds of microns and working fluid volumes between 10^{-9} to 10^{-18} litres [1]. Due to the relatively small length scales found in microfluidic devices, viscous and interfacial forces tend to dominate inertial and gravitational forces respectively, leading to unique advantages (and challenges) when integrating microfluidic technology into workflows. Heralded as the "game changer in life sciences research and industry" [2], microfluidic application in a range of diverse fields such as national security [3], microprocessor cooling [4], forensic DNA analysis [5], and cell biology [6] (the focus of this thesis) has boasted remarkable advantages over its traditional *macro*fluidic counterpart. In cell biology specifically, microfluidic application has significantly increased the speed and precision of micro/nano volume manipulation in bioassays, reduced experimental sample sizes and reagent volumes (thus decreasing costs), and considerably decreased experimental processing times when integrated into existing workflows [6], [7].

2.2 The Evolution of Microfluidic Devices

Richard Sweet's inkjet printer is regarded as the first microfluidic system ever designed and is responsible for kick starting rapid interdisciplinary innovation in the field [2]. Although Sweet's paper introducing the inkjet printer [8] was published in 1965, the microfluidic theory behind Sweet's novel device had already been around for nearly 100 years. Walter Rayleigh in his seminal paper '*On the capillary phenomena of jets'* [9] outlined a continuous stream of liquid's tendency to separate into droplets in order to minimize surface energy depending on the

free stream's relative inertial and interfacial forces [10]. Sweet's inkjet printer took advantage of this phenomena in order to create an array of small ink droplets to pattern paper [8].

The next major advancement in microfluidics was proposed by Manz et al. in 1990. In his paper '*Miniaturized total chemical analysis systems: a novel concept for chemical sensing*' [11], he proposed designing stand-alone microfluidic devices solely capable of carrying out all tasks required in microfluidic analysis. According to Manz, sample preparation, data acquisition, and data analysis can all be integrated into a single miniaturized Total Analysis System (later known as μ-TAS) [11]. While this revolutionary design ideology kick-started a surge of microfluidic interest across a variety of disciplines, important μ-TAS design characteristics were not yet optimized for widespread application; the material upon which μ-TAS devices were fabricated was one such design flaw which prevented widespread μ-TAS integration. Many of the first μ-TAS devices were designed on silicon or glass, both of which share various material disadvantages. For instance, both silicon and glass devices are brittle, experience difficulty bonding to other substrates, and have expensive production processes [6]. Additionally, silicon is opaque to visible and ultraviolet light making certain biological analysis tools such as microscopy difficult [6]. To address these material deficiencies, Polydimethylsiloxane (PDMS) microfluidic devices fabricated using soft lithography [12] became increasingly popular [13], [14].

2.2.1 Microfluidic Application in Cell Biology

Cell culturing, or the growth and study of cells in an *in vitro* environment [15], is one field where microfluidic application presents many benefits [1], [6], [13]. PDMS-based Organ-on-a-Chip (OoC) technology has given rise to a series of microfluidic devices capable of closely replicating *in vivo* organ functions such as gut-on-a-chip [16], lung-on-a-chip [17], kidney-on-a-chip [18], and blood vessel-on-a-chip [19]. These microfluidic devices are specifically useful in replicating fluid dynamic phenomena experienced *in vivo* and can lead to important biological advances with less animal testing and human trials [20]. The blood vessel-on-a-chip device in Figure 1, for instance, mimics *in vivo* blood vessel fluid dynamics such as blood flow rate and endothelial cell shear stress and has been used clinically to diagnose sickle cell disease [19]. A theoretical combination of OoCs mimicking cooperative organ function can potentially form a "human-on-a-chip" [21], although this pinnacle microfluidic prototype is still a work in progress.

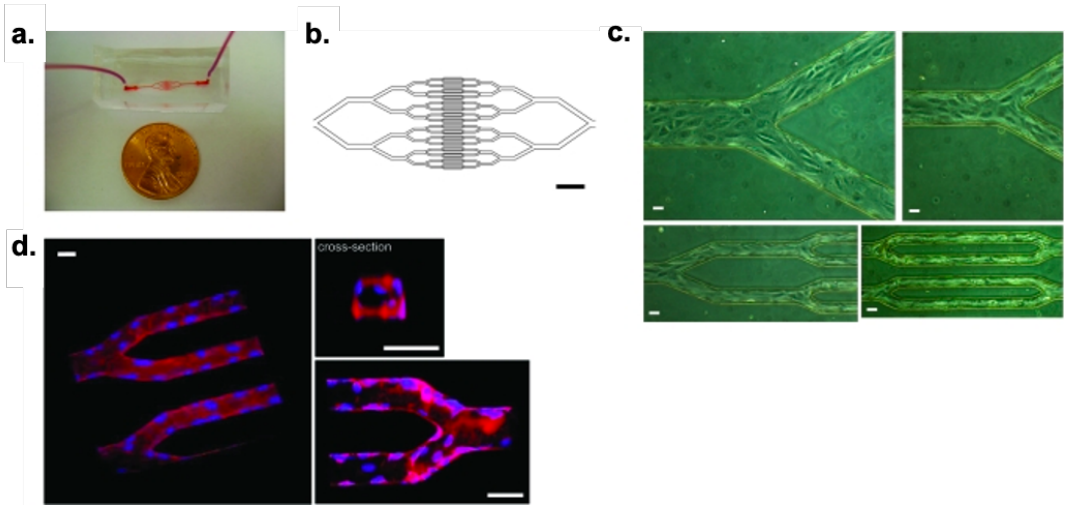

Figure 1. Images from Tsai et al. '*In vitro modeling of the microvascular occlusion and thrombosis that occur in hematologic diseases using microfluidic technology*' [19]. Blood Vessel-on-a-Chip microfluidic device used to clinically diagnose sickle cell disease. **a**. PDMS microdevice. **b**. Software-generated image of the photolithography mask that defines microfluidic channel geometry. [Scale bar: 600 μm] **c**. Brightfield images showing human endothelial cell culture after 48 hours [Scale bars: 30 μm] **d**. 3D renderings of multiple confocal microscopy using fluorescent cell membrane (red) and cell nuclear (blue) dyes show that endothelial cells line the entire inner surface of the channels. [Scale bars: 30 μm]

Despite successful microfluidic application in OoC technology, the magnitude of microfluidic application in cell biology does not match its widely claimed advantages; only 6% of all microfluidic publications in 2002 were in biology or medical journals [6]. Again, material incompatibility was to blame. PDMS is a preferred microfluidic material to earlier silicon and glass devices since PDMS is a transparent elastomer allowing for real time experimental analysis and is much easier to bond to other substrates [6], [22]. However, PDMS devices reportedly lack biocompatibility (PDMS leaches toxins harmful to cell growth [22] and absorbs molecules necessary for cell signaling [23]), has reduced real-time accessibility, and also requires expensive manufacturing methodology [22]. Additionally, PDMS's vapor-permeability allows for cell media evaporation which can lead to osmolarity shifts that effect cell differentiation [24].

2.3 Open Microfluidics

"Microfluidics should be able to interact with such substrates in the open space, essentially in their native state, which will facilitate the study of biological samples. To succeed in these endeavors, microfluidics needs to eliminate one of their major constraints: the walls." [25]

Direct manipulation and visualization of microfluidic circuits (and the living cells which they bear) are experimental necessities when working with cell-based assays. Traditionally *closed* PDMS microfluidic devices, among other material deficiencies discuss above, prevent direct fluid/cell manipulation since their channels are completely constructed of solid walls. *Open* microfluidic devices, however, are comprised of microfluidic systems with at least a single solid boundary removed thus exposing the device's working fluid to a second, immiscible fluid [26]. Working fluids can be open to the atmosphere or (more common in cell biology to avoid evaporation) open to an inert immiscible liquid. Open microfluidics allows for seamless integration onto biocompatible materials (say Petri dishes), bubble-free microfluidic operation, and perhaps most importantly real time liquid/cell manipulation [26], [27].

2.3.1 Freestyle Fluidics

An open microfluidic approach named 'Freestyle Fluidics' [27] has demonstrated a versatile microsystem fabrication technique capable of quick and seamless integration into any cell biologist's laboratory (see Figure 2).

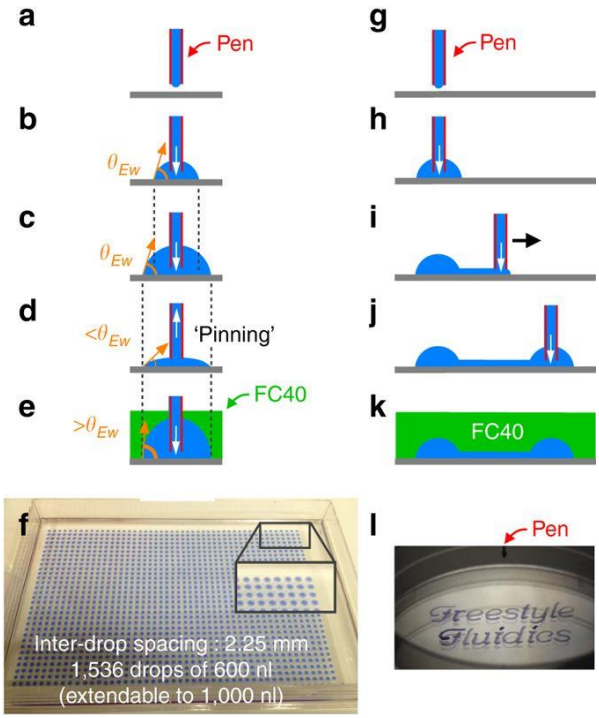

Figure 2. Images from Walsh et al. '*Microfluidics with fluid walls*' [27]. 'Forward Printing' circuits without solid walls (freestyle fluidics). **a**. Pen hovers over substrate's surface. **b**. Cell media is deposited onto the surface via an external syringe pump. **c**. Media is added, increasing the footprint of the deposited media and pushing the droplet's pinning lines radially from the pen's centre line. **d**. Media is removed, although the footprint remains unchanged. **e**. Media is overlayed with FC-40. This increases the media's equilibrium contact angle ($\boldsymbol{\theta_{Ew}}$) and thus increases the volume the drop is able to hold compared to when open to the atmosphere. **f**. A forward printed array of 1536 drops of media (plus blue dye) under FC-40 in a flat microtiter plate. **g–k**. Steps to print a simple circuit capable of passive flow connecting two adjacent droplets.

This "forward printing" method involves dispensing cell media from a traverse-controlled capillary onto a clean substrate's surface in any desired two-dimensional design, and then overlaying the printed microcircuit with an immiscible fluorocarbon (typically FC-40) to prevent

media evaporation. Intricate and precise microfluidic circuits can be printed in seconds, thus significantly reducing fabrication time and need for specialized equipment when compared to traditional fabrication techniques such as soft lithography. Moreover, 'Freestyle Fluidic' fabrications are performed on substrate surfaces that have been used in cell biology labs for decades; tissue culture Petri dishes. This approach empowers cell biologists with the ability to transform typical Petri dishes into ready-to-use microfluidic devices in the confines of their own laboratories.

Similarly, 'Freestyle Fluidic' arrangements can also be formed by *reshaping* fluids already present on the surface of a Petri dish in an approach called "reverse printing" [28]. Instead of dispensing cell media onto a clean substrate (forward printing), reverse printing fabrication "cuts" though a thin layer of media that is already deposited on a substrate's surface using a hydrophobic/fluorophilic polytetrafluoroethylene (Teflon) drawing stylus. "Cuts" are created when the traverse controlled drawing stylus is dragged across a wetted substrate's surface. Whilst the media is being displaced by the drawing stylus, overlaying FC-40 immediately fills the media's place along the cut.

2.4 Microfluidic Circuits Formed with Submerged Microjets

In this thesis we introduce a novel non-contact approach to reverse printing microfluidic circuits using a submerged impinging microjet: SIM-printing. Known for their high heat and mass transfer rates, impinging liquid jets have been used as pressure washers to clear liquids, biofilms, cells, and soils from substrate surfaces [29]–[32]. In this approach, a liquid FC-40 microjet acts as a small pressure washer, capable of precisely displacing substrate-anchored cell media in virtually any predetermined two-dimensional pattern (see Figure 3a). Vast arrays of cell media chambers, each mimicking an independent *in vitro* well in a microtiter plate (Figure 3b,i) or complex asymmetrical fluid circuit geometries (Figure 3b,ii) take only minutes to fabricate using a triple axis traverse and an external pump driving the jetting system.

This thesis addresses the impact of user input parameters such as microjet traverse speed, volumetric flow rate, and height above impinged substrate on SIM-printed circuit geometry (namely FC-40 "wall" widths). Firstly, an experimental facility capable of SIM-printing is established and validated. To demonstrate this method's application in cell biology, focus is placed on printing surfaces (Petri dishes) and fluids (cell media) common in cell biologist's laboratories. Next, SIM-printing capabilities for a range of clean and biological fluids are studied and the unique "elastic film" which develops at the bioliquid-fluorocarbon interface is examined using Pendant Drop Tensiometry. Finally, the flexible nature of SIM-printed circuits contained by fluid walls presented the novel and challenging problem of characterizing fluid dynamic phenomena in these microsystems. Both an analytical and numerical solution to fluid flow through SIM-printed circuits is derived and validated experimentally, thus giving cell biologists the ability to develop microfluidic circuits with specific flow and shear profiles for various application involving dynamic environments.

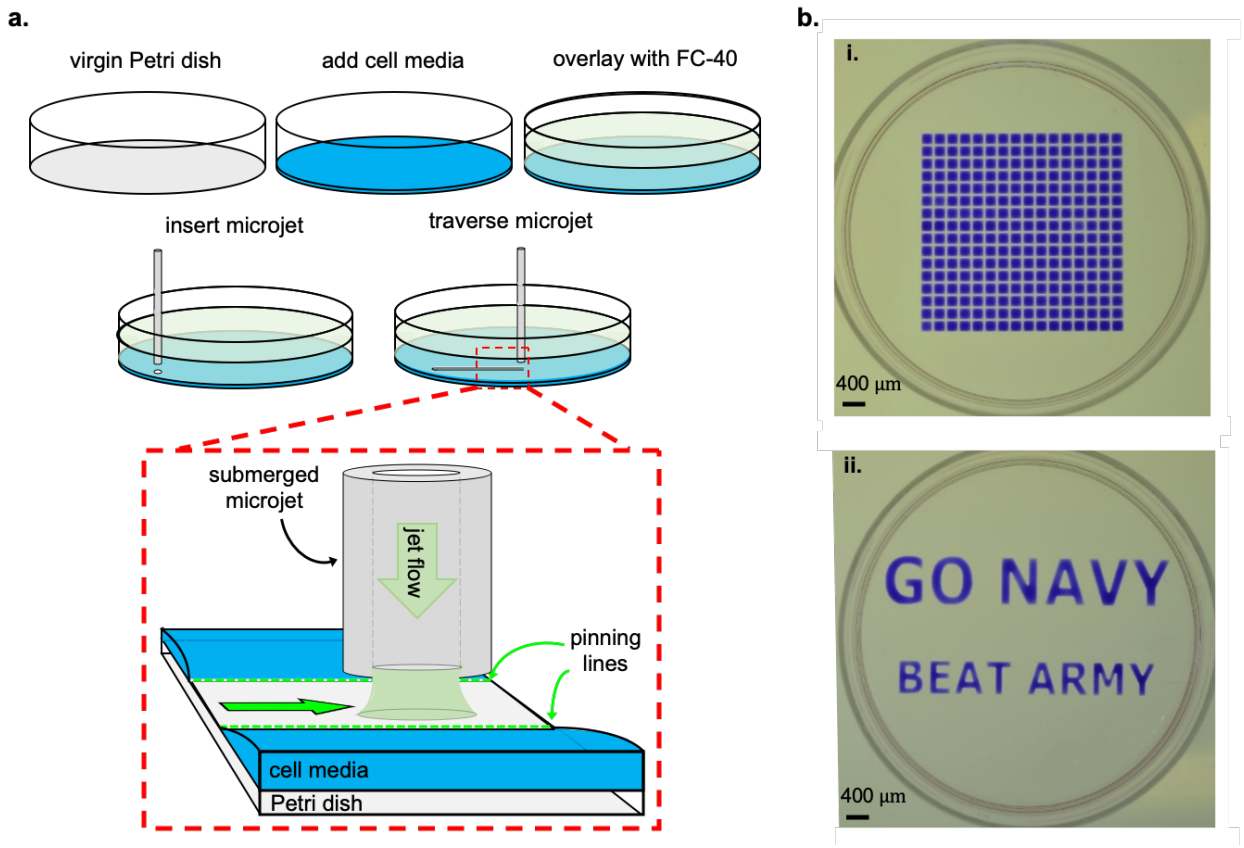

Figure 3. Submerged impinging microjet (SIM) printing **a.** Sample preparation and printing technique. First acquire a sterile, virgin 60 mm x 15 mm polystyrene tissue culture treated Petri dish. Cover the Petri dish with a thin, uniform layer of aqueous-based cell media solution and then overlay with 1 mL of FC-40. Completely submerge the microjet orifice in FC-40 and begin jetting FC-40 via an external syringe pump to displace media from the wetted Petri dish. Moving the microjet with a three-axis traverse across the Petri dish's surface creates FC-40 "walls" which confine regions of media (the circuit) by interfacial forces along pinning lines. **b.** A demonstration of the versatile capabilities of SIM-printing within a 60 mm tissue culture Petri dish. Each dish, wetted with DMEM cell media +10% by volume Fetal Bovine Serum (FBS), is overlayed with FC-40 before jetting. The SIM-printed circuit(s), following fabrication, were subsequently infused with blue dye to increase visibility. **i.** SIM-printed 16x16 cell assay grid (1.9 mm distance between the centres of adjacent square chambers) mimicking tradition static cell assays utilized by biologists. **ii.** SIM-printed United States Naval Academy moto, demonstrating the fabrication technique's ability to develop complex and asymmetrical microcircuit geometries.

3 Research Objectives

The focus of this research is to provide a better physical understanding of the jetting process for fabrication of microfluidic arrangements, extend an analytical solution for accurately predicting conduit flow dynamics, and provide design rules for future implementation of the method to biological applications. The following outlines this research's primary objectives:

1. Set up experimental programme for the development, and quantification, of submerged impinging microjet (SIM) printing technology.
2. Experimentally quantify the sensitivity of SIM-printed FC-40 wall widths when varying SIM traverse speed, flow rate, height above substrate, and orifice diameter.
3. Experimentally elucidate the boundary condition to apply to the analytical model at the SIM-printed circuit interface.
4. Demonstrate the physical variation in drop dynamics/interfaces when subject to biological fluid media.
5. Contribute to development of theory for flow in simple circuits and validate this theory using experiments.
6. Develop methodology and theory to control shear stress gradient in flexible-walled conduits.

4 Theory

4.1 Submerged Impinging Microjet (SIM) Physics

Liquid jets are typically split into two categories: free-surface jets and submerged jets. A free-surface jet's flow exits the jet's orifice into some volume of gas (typically the atmosphere) whereas a submerged jet's orifice is completely submerged in a volume of liquid [33]. Although the liquid flow from both free and submerged jets share many similarities, the following chapter will be primarily focused on submerged jets due to the nature of this paper's microfluidic circuit fabrication technique (SIM-printing). For similar reasons, only circular jet nozzle geometries will be considered in the following chapters.

4.1.1 Jet Formation Before Exiting Microjet Nozzle

As Figure 4a displays, the jet used for SIM-printing microfluidic circuits is a 34G needle (although needles with larger or smaller internal diameters can also be used for SIM printing so long as the jet's volumetric flow rate is adjusted). Liquid flow through the 10 cm long, 70 μm inner diameter needle before reaching its submerged orifice obeys classical pipe fluid dynamics. Liquid is actively pumped through the jet with a fixed volumetric flow rate $\mathbf{Q}$ via an external syringe pump. With a known volumetric flow rate and jet diameter $\mathbf{d_i}$, the jet's average flow velocity $\mathbf{u_{avg}}$ can be determined by the following relationship:

$$\mathbf{u_{avg}} = \frac{4\mathbf{Q}}{\pi \mathbf{d_i^2}} \tag{1}$$

When flow inside of the jet is fully developed (see Figure 4b), the flow's velocity field will maintain a parabolic profile according to Equation 2 [34]:

$$\mathbf{u(r)} = 2\mathbf{u_{avg}}\left(\mathbf{1} - \frac{4\mathbf{r}^2}{\mathbf{d_i^2}}\right) \tag{2}$$

To ensure that flow within the jet is indeed fully developed before reaching the orifice, the jet's entry length $\boldsymbol{l_e}$ based on the criteria for laminar pipe flow must be considered [34].

$$\frac{\boldsymbol{l_e}}{\mathbf{d_i}} = 0.06\mathbf{Re} \tag{3}$$

The jet's Reynolds number, **Re**, is a dimensionless number which compares the significance between inertial and viscous forces for a given dynamic system. A circular jet's Reynold's number is calculated as follows:

$$\mathbf{Re} = \frac{\boldsymbol{\rho}\mathbf{d_i}\mathbf{u_{avg}}}{\boldsymbol{\mu}} \tag{4}$$

where $\boldsymbol{\rho}$ and $\boldsymbol{\mu}$ are the jetting liquid's density and dynamic viscosity respectively. Reynolds numbers less than 2300 characterize flows in the laminar regime in which layers of fluid tend to flow perfectly parallel to one another (see velocity vector field in Figure 4b). Conversely, flows with Reynolds numbers greater than 2900 are predominately turbulent and have chaotic and unpredictable flow patterns; 2300< **Re** < 2900 define flows which are transitioning between laminar and turbulent flows. In microfluidic systems, viscous forces tend to dominate due to small characteristic lengths and relatively slow flow velocities resulting almost always in perfectly laminar flow. During nominal flow conditions using the submerged microjet shown in Figure 4a-b, $\mathbf{Re_{jet}} \approx 80$ (see Table 1 in Appendix 1 for more information).

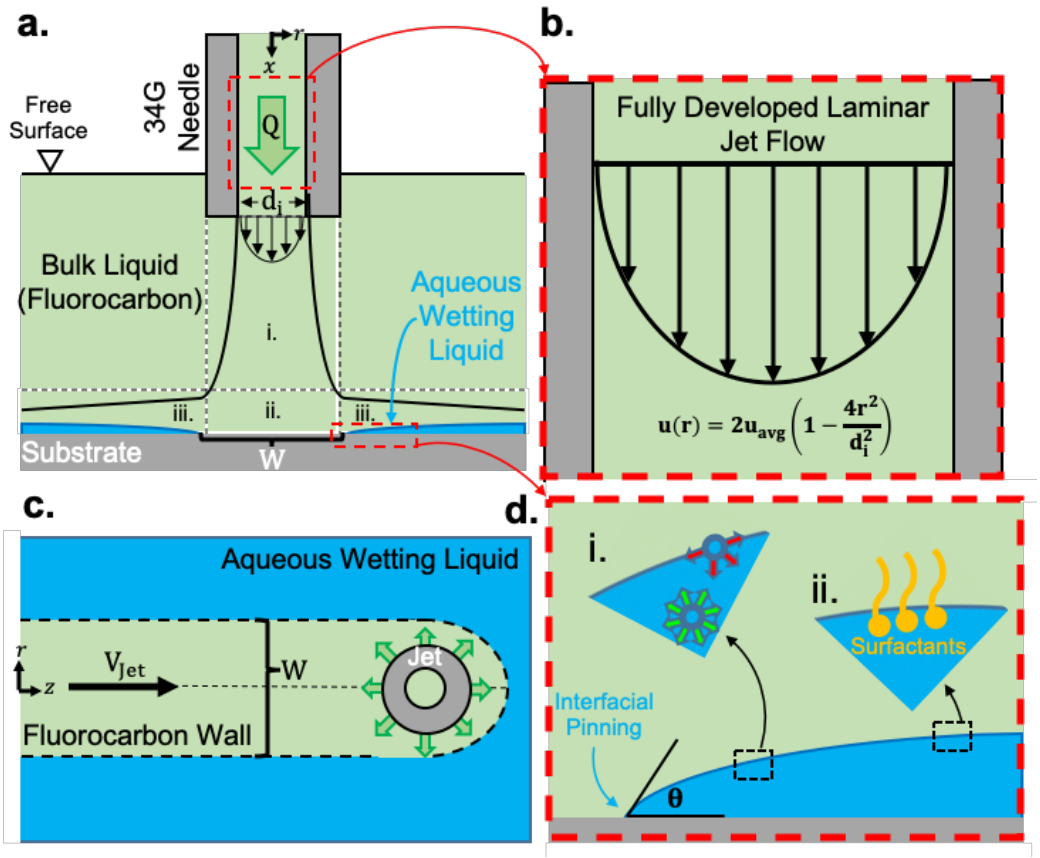

Figure 4. Submerged Impinging Microjet (SIM) Theory. **a.** Submerged impinging microjet of internal diameter $\mathbf{d_i}$ and volumetric flow rate **Q** displaying SIM-printing capabilities in a biocompatible environment. The wetting liquid (blue) is a thin (~ 25 μm) aqueous phase which completely covers the solid substrate (typically a tissue culture Petri dish) whereas the bulk liquid (green) is an immiscible fluorocarbon open to ambient conditions. The jetting liquid and the bulk liquid are both the same fluorocarbon (FC-40) to ensure easy mixing of microjet-discharged liquid with the submerged environment. The wetting fluid is radially displaced a distance $\frac{\mathbf{W}}{2}$ from the jet's centreline due to a combination of pressure and viscous forces analogous to the operation of a pressure washer. The primary regions of submerged jet flow are **(i)** The Free Jet Region. **(ii)** The Impingement Region. **(iii)** The Wall Jet Region. **b.** Flow within the jet (34G needle) is assumed to be fully developed laminar. **c.** Top view of a submerged microjet moving at a traverse-controlled speed of $\mathbf{V_{jet}}$ across a substrate's surface creating a fluorocarbon "wall" of width **W** in the direction of traverse motion. **d.** An FC-40 wall's pinning lines are held in place by interfacial forces between the aqueous and fluorocarbon phases. **i.** Energetically unfavorable molecules at the immiscible liquid-liquid interface (molecule with red intermolecular force arrows) tend to have a net "pulling" force towards fellow molecules of the same species in the bulk of the wetting liquid. The molecules in the bulk fluid (molecule with green intermolecular force arrows) experience equal intermolecular pull in all directions and thus experience no net pull. This phenomenon causes a tension-like force across the liquid-liquid interface called interfacial tension. **ii.** Amphiphilic molecules called surfactants attach to immiscible interfaces and decrease a system's interfacial tension. Surfactants found in this system would commonly have hydrophilic heads and hydrophobic tails, leading to the preferred orientation depicted above.

4.1.2 Jet Formation After Exiting Microjet Nozzle

The liquid of a laminar, submerged jet can exit the jet's orifice with a variety of flow profiles [35], [36]. Nozzle characteristics such as length, internal cross-sectional geometry, and edge sharpness [36] are the primary factors which determine the jet's flow profile immediately following liquid ejection. For the jets covered in this study (34G needles with long, circular "nozzles"), perfectly parabolic, fully developed flow profiles are expected as fluid exits the jet orifice (Figure 4a).

After exiting the nozzle, a submerged impinging jet enters three distinct flow regions as described in Figure 4a,i-iii [35]. The free jet region (i) begins as soon as liquid exits the jet's orifice. Upon ejection, the flow's fully developed parabolic velocity profile immediately begins flattening due to external shear and expands radially proportional to the flow's flight distance normalized by the jet's nozzle diameter $\left(\frac{\mathbf{x}}{\mathbf{d_i Re}}\right)$; flow slows and expands as the distance from the jet orifice increases as described by Kashi et. al [37]. Next flow enters the impingement region (ii), at which point the jet stream changes its direction due to the solid wall (in this case the surface of a Petri dish). Finally jet flow enters the wall jet region (iii), which is characterized by a thin axisymmetric layer of fluid flowing radially from the point of impingement. The wall jet's flow slows with increased distance from the impingement region and eventually mixes freely with the bulk fluorocarbon which originally submerged the tip of the jetting needle [35].

4.1.3 Cleaning Surfaces with Impinging Jets

Impinging liquid jets can be used as pressure washers to clear thin liquid films (or solid sediment) from substrate surfaces[31], [32], [38]–[40]. In the impingement region (Figure 4a,ii), a fluorocarbon jet displace substrate-anchored aqueous solution (typically cell media in SIM-printing applications) by the pressure force exerted onto the normal surface from the jet's

momentum. Media displacement also occurs in the Wall Jet Region (Figure 4a,iii) due to the wall jet's shear which "drags" the aqueous film radially away from the point of impingent. After media displacement, surrounding bulk fluorocarbon immediately takes its place by wetting the substrate. When the jet moves across the substrate's surface in the *r*-*z* plane, a "fluorocarbon wall" replaces the cleared media film (see Figure 4c) in any two-dimensional design necessary for the desired microfluidic application.

When making static microfluidic arrangements, patterns can be "drawn" by tracing a closed chamber of appropriate shape. When creating circuits that support dynamic system flows, two parallel lines are often traced with the SIM-printer to form an aqueous conduit confined by two fluorocarbon walls. The fluorocarbon walls' pinning lines shown in Figure 4d are held in place by interfacial forces between the immiscible fluorocarbon and aqueous solution. The interfacial tension between the two fluids prevents the aqueous solution from advancing until a critical contact angle ($\boldsymbol{\theta_{adv}}$) is reached.

4.2 Surface/Interfacial Tension Between Immiscible Fluids

In the absence of gravity or other external forces, liquid volumes tend to form perfect spheres [41] in an attempt to minimize free surface energy. For instance, consider a small water droplet of volume $\mathbf{V}$ on the surface of a Petri dish covered by FC-40. The H_2O molecules in the bulk liquid of the droplet have mutual attractions to neighboring H_2O molecules in all directions equally. H_2O molecules on the surface of the droplet in contact with the surrounding immiscible fluorocarbon, however, experience a non-uniform pull *into* the direction of the bulk droplet; the cohesive forces between fellow H_2O molecules is much greater than the intermolecular forces between molecules of an immiscible liquid, thus creating an inward pull felt by H_2O molecules at the droplet-fluorocarbon interface. To increase the droplet's surface area (e.g., by infusing

more H_2O into the droplet) work is required to increase the number of H_2O molecules located on the drop's energetically unfavorable surface. The expenditure of energy required to increase the drop's surface area is commonly referred to in terms of force per unit length and is called *interfacial tension* due to the "tension-like" force which pulls inward on the H_2O molecules on the drop's interface [42]. This phenomena explains why SIM-printed microfluidic circuits have a curved profile at the aqueous-fluorocarbon pinning lines such as in Figure 4d,i.

Surfactants, otherwise known as 'surface-active agents' [43]–[45], are amphiphilic molecules whose structure (consisting of both a tail and a head) have opposite affinities for immiscible fluids. Commonly, surfactants have hydrophilic heads and hydrophobic tails, causing such surfactants to be attracted to the liquid-liquid interface of an aqueous-fluorocarbon environment (Figure 4d,ii). Surfactants at a liquid-liquid interface decreases the system's interfacial tension since they interfere with more energetically favorable connections between neighboring molecules of the same phase [45].

4.2.1 The Young-Laplace Equation

Curvature along an immiscible system's liquid-liquid interface due to interfacial tension gives rise to a pressure difference across the interface itself. The Young-Laplace Equation governs this pressure difference and is expressed as:

$$\mathbf{\Delta P_L = \gamma\left(\frac{1}{R_1} + \frac{1}{R_2}\right)} \quad \textbf{(5)}$$

$\mathbf{\Delta P_L}$, commonly referred to as the Laplace Pressure, is the pressure difference across a fluid-fluid interface, $\boldsymbol{\gamma}$ is the system's interfacial tension, and $\mathbf{R_1}$ and $\mathbf{R_2}$ are the interface's principal radii of curvature [43]. The smaller the radii of curvature of a given fluid element and the greater the system's interfacial tension, the higher the pressure difference across the liquid-liquid interface becomes. For a perfect sphere, which by definition results in a surface element geometry where $\mathbf{R_1 = R_2}$, the Young- Laplace Equation can be reduced to:

$$\mathbf{\Delta P_L = \frac{2\gamma}{R}} \quad \textbf{(6)}$$

Similarly, when a fluid exhibits a cylindrical profile in which one of the principal radii of curvature is infinite, the Young-Laplace equation simplifies to the following:

$$\mathbf{\Delta P_L = \frac{\gamma}{R}} \quad \textbf{(7)}$$

4.2.2 Measuring Interfacial Tension

There are numerous static techniques for measuring surface and interfacial tension between two immiscible fluids. Common techniques include direct methods using microbalances (Wilhelmy Plate [46] and Du Nouya Ring [47] techniques), capillary pressure measurement methods (maximum bubble pressure [48] and growing drop [49] techniques), analysis of capillary/gravity forces methods (capillary rise [50] and drop volume [51] techniques), and gravity-distorted drop methods (Pendant Drop Tensiometry [52] and Sessile Drop [53] techniques) [54]. Pendant Drop Tensiometry, however, is considered by current literature in colloidal and interface sciences as the most robust, versatile, accurate, and simple method currently available [52] and thus is the natural first choice for measuring interfacial tension.

4.2.2.1 Pendant Drop Tensiometry

Pendant Drop Tensiometry is used to measure the interfacial tension ($\boldsymbol{\gamma}$) between two immiscible fluids as gravity distorts an otherwise perfectly spherical drop. A drop of liquid (commonly referred to as the drop phase) is formed at the tip of a capillary while completely submerged in a second, immiscible fluid (the continuous phase) as in Figure 5a-c [52]. Once formed on the tip of a capillary, an image of the static axisymmetric drop is captured and analyzed in image analysis software in order to measure the drop's principal radii of curvatures.

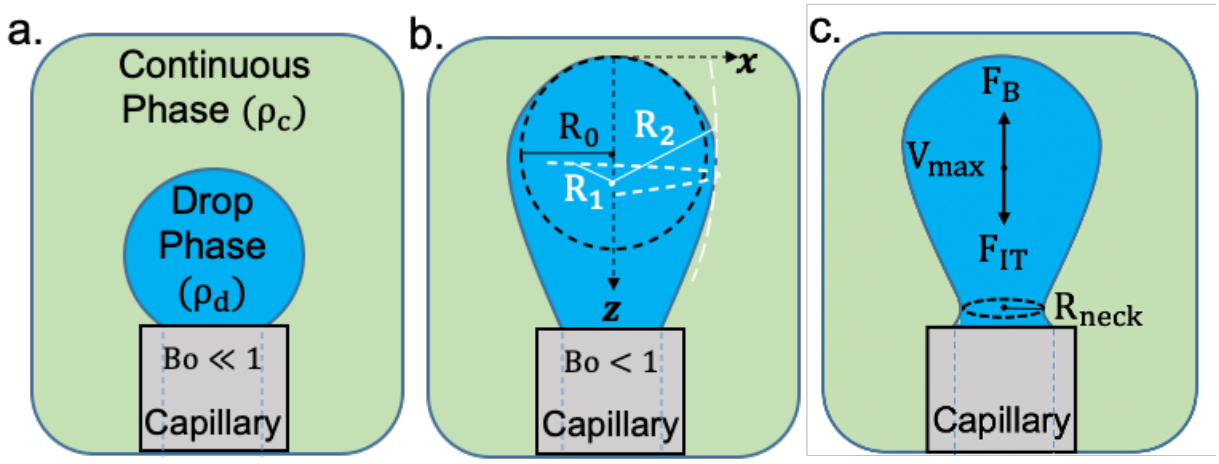

Figure 5. Pendant Drop Tensiometry orientation when continuous phase density is greater than drop phase density ($\boldsymbol{\rho_c > \rho_d}$). **a.** Drops with small volumes are dominated by interfacial forces ($\mathbf{Bo} \ll 1$) and thus tend to form perfectly spherical geometries; drops of this size are not useful for Pendant Drop image analysis. **b.** As the drop's volume increases, the buoyancy forces acting on the drop distort the drop's otherwise spherical geometry into a "teardrop" shape. Pendant Drop image analysis relies on this geometrical distortion to accurately measure interfacial tension between two immiscible fluids. A reference pressure for the drop's hydrostatic head is set at $z = 0$ at which point the drop's projected radius ($\mathbf{R_0}$) creates a perfect sphere. Two principle radii of curvatures ($\mathbf{R_1}$ and $\mathbf{R_2}$) are then determined via image analysis software in order to calculate interfacial tension. **c**. Known as Tate's Law, interfacial tension can also be calculated by evaluating the static force balance acting on the drop phase just before the drop departures its capillary. Gravity causes a buoyancy force ($\mathbf{F_B}$) which attempts to detach the drop from its capillary while interfacial forces ($\mathbf{F_{IT}}$) act to hold the drop together at its minimum radius $\mathbf{R_{neck}}$. While attached to the capillary, $\mathbf{F_{IT}} \geq \mathbf{F_B}$.

As mentioned, Pendant Drop Tensiometry relies on the gravitational distortion of a drop's geometry to produce accurate interfacial tension measurements. In the absence of strong gravitational forces (small drop volumes) a drop will form a near-perfect sphere (Figure 5a). As drop volume increase, however, gravity distorts the once spherical drop resulting in a teardrop shape (Figure 5b). The Bond number (**Bo**) is a dimensionless representation of the ratio of gravitational to interfacial forces acting on a fluid volume in a two-phase system:

$$\mathbf{Bo} = \frac{\boldsymbol{\Delta\rho g L^2}}{\boldsymbol{\gamma}} \tag{8}$$

$\boldsymbol{\Delta\rho}$ denotes the difference in density between the drop phase ($\boldsymbol{\rho_d}$) and continuous phase ($\boldsymbol{\rho_c}$) whereas $\mathbf{L}$ represents some characteristic length such as the drop's radius of curvature at its apex ($\mathbf{R_0}$) [52]. A system's capillary length ($\mathbf{L_c}$), or the length at which $\mathbf{Bo} = 1.0$, is a common benchmark to signify when gravitational forces begin to dominate. For a two-phase system containing water and FC-40, $\mathbf{L_c} = 2.5$ mm. Typically drops below the capillary length are studied during Pendant Drop Tensiometry tests. However, as a drop's Bond number nears zero, interfacial tension measurements become significantly more inconsistent and unreliable since the drop's geometrical distortion due to gravity is nearly unrecognizable [52], [55].

A drop's principle radii of curvature (obtained numerically from edge detection software) is used to calculate interfacial tension from a simple pressure balance experienced by the drop; while interfacial forces cause a pressure difference across a fluid-fluid interface (Laplace Pressure described in Equation 5), gravity gives rise to a hydrostatic pressure gradient along the z-axis. The drop's pressure balance is defined by the following equation:

$$\boldsymbol{\gamma\left(\frac{1}{R_1}+\frac{1}{R_2}\right)=\Delta\rho gz+C} \tag{9}$$

where $\mathbf{C}$ represents an arbitrary static pressure reference at some z location in Figure 5b. If the arbitrary reference pressure is set to be at $z = 0$ (or at the top of the drop as shown in Figure 5b), $\mathbf{R_1 = R_2 = R_0}$ since the top of a pendant drop can be projected to a perfectly spherical profile. After applying this boundary condition at $z = 0$, solving for $\mathbf{C}$ and then $\boldsymbol{\gamma}$ can be accomplished.

$$\boldsymbol{C=\frac{2\gamma}{R_0}} \tag{10}$$

$$\boldsymbol{\gamma = \frac{\Delta \rho g z}{\frac{1}{R_1} + \frac{1}{R_2} - \frac{2}{R_0}}} \quad \textbf{(11)}$$

This elegantly simple method of accurately measuring interfacial tension requires nothing more than a drop's radii of curvature(s) and the two phase's densities ($\boldsymbol{\rho_d}$ and $\boldsymbol{\rho_c}$ respectively) [56].

4.2.2.2 Drop Volume Technique

Pendant Drop Tensiometry setups can also calculate interfacial tension by considering the force balance between interfacial tension and gravity (Tate's Law) [51] acting on a static pendant drop before departure from its capillary. For a drop to remain attached to a capillary its interfacial forces at the drop's minimum radius about the *z*-axis ($\boldsymbol{R_{neck}}$ in Figure 5c) must be greater than or equal to the buoyancy forces due to gravity. Bereft of any external forces or agitations, the force balance between gravitational and interfacial forces can be equated as follows directly before a static drop begins to depart from its capillary:

$$\boldsymbol{(\rho_c - \rho_d) V_{max} g = 2\pi R_{neck} \gamma} \quad \textbf{(12)}$$

With a known infused volume, phase densities, and droplet neck radius, the system's interfacial tension can be calculated. Conversely, if a system's interfacial tension is known, the drop's theoretical maximum volume can be determined.

4.3 Flow Through Fluid-Walled Microfluidic Conduits

Using the SIM microcircuit fabrication technique discussed in Chapter 4.1, open microfluidic channels capable of mass transfer can be developed for a variety of applications in cell biology. The following theoretical discussion regards flow through a simple, linear "fluid" conduit only. While the following theory can be applied to more complex circuit geometries (and previous fabrication techniques such as forward [27] and reverse [28] printing), these will not be considered in the following chapter since all fluid dynamic phenomena in such circuits will be derivative of the following. Additionally, this theory was developed in a group consisting of Dr. Edmond Walsh, Dr. Peter Cook, Cyril Deroy (DPhil Candidate), Cristian Soitu (DPhil Candidate), and Federico Nebuloni (DPhil Candidate) and are included in our paper 'Flow dynamics in a fluid-walled conduit' which is currently in preparation.

4.3.1 Analytical Solution

The analytical solution to flow through flexible fluid-walled microcircuits is derived using the governing equations that dictate all fluid flows: the Navier-Stokes equations. Assuming fully developed laminar flow of an incompressible Newtonian liquid, the Momentum Equation in the direction of flow (the *x*-direction as depicted in Figure 6a-c) can be written as follows:

$$\mathbf{u}\frac{\partial \mathbf{u}}{\partial \mathbf{x}} + \mathbf{v}\frac{\partial \mathbf{u}}{\partial \mathbf{y}} + \mathbf{w}\frac{\partial \mathbf{u}}{\partial \mathbf{z}} = -\frac{\mathbf{1}}{\boldsymbol{\rho}}\frac{\partial \mathbf{P}}{\partial \mathbf{x}} + \boldsymbol{\nu}\left(\frac{\partial^2 \mathbf{u}}{\partial \mathbf{x}^2} + \frac{\partial^2 \mathbf{u}}{\partial \mathbf{y}^2} + \frac{\partial^2 \mathbf{u}}{\partial \mathbf{z}^2}\right) \quad \textbf{(13)}$$

u, **v**, and **w** each represent the magnitude of the flow's velocity in the by x, y, and z direction respectively. **ρ** is the fluid's density and **ν** is the fluid's kinematic viscosity, both of which are assumed to be constant with respect to time and location. **P** represents pressure due to flow.

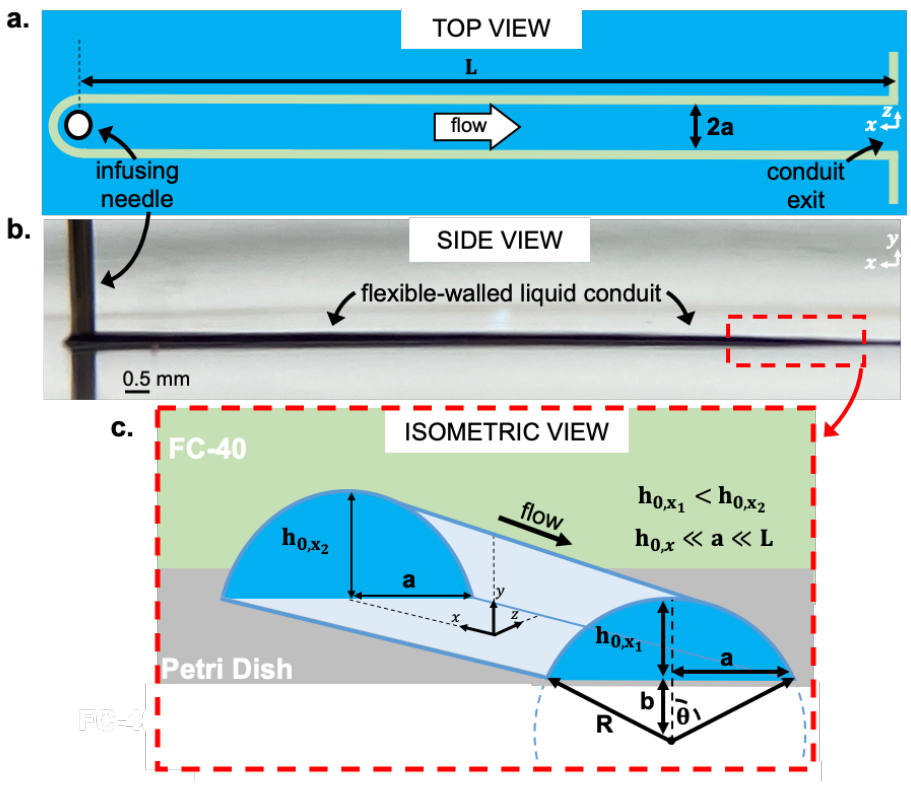

Figure 6. Flexible-walled fluid conduit experiencing flow. **a.** Plan of a simple SIM-printed microfluidic circuit on the surface of a Petri dish consisting of only a single conduit connected to the remainder of the dish's wetted surface. Aqueous liquid is actively pumped through a needle via an external syringe pump in the *x*-direction through conduits whose length **L** is much larger than its half width **a** and local cross-sectional height $\mathbf{h_{0,x}}$ ($\mathbf{L} \gg \mathbf{a} \gg \mathbf{h_{0,x}}$). **b.** Image of a flexible-walled conduit illustrating the decrease in conduit height ($\mathbf{h_{0,x}}$) in the direction of flow. Unlike flow through solid microcircuits which experience linear pressure drop in the direction of flow, the pressure gradient increases dramatically near the flexible-walled conduit's exit. **c.** An isometric view of flow through SIM-printed conduits highlighting key geometrical parameters.

Microfluidic systems typically operate at very low Reynolds numbers and thus experience nearly perfect unidirectional laminar flows. Since the Reynolds numbers of the microconduits covered in this study never exceeded 0.1 at even the highest flow rates used (see Table 2 in Appendix 1 for more details) unidirectional laminar flow is assumed; $\mathbf{v} = \mathbf{w} \approx 0$. Furthermore, these conduits' entry lengths (yet another artefact of a system's Reynolds number) are less than one micron, resulting in fully developed flow for the purposes of this analytical derivation; $\frac{\partial \mathbf{u}}{\partial \mathbf{x}} = \frac{\partial^2 \mathbf{u}}{\partial \mathbf{x}^2} \approx 0$. It is also convenient to combine **ρ** and **ν** into a single fluid property **μ** (dynamic viscosity) using the following relationship:

$$\boldsymbol{\mu = \nu\rho} \tag{14}$$

A simplified Momentum equation can now be written as:

$$\boldsymbol{\frac{\partial P}{\partial x} = \mu \frac{\partial^2 u}{\partial y^2}} \tag{15}$$

4.3.1.1 Cross-Sectional Geometry of Fluid Conduits

Figure 6c shows an isometric view of a SIM-fabricated, fluid-walled conduit whose geometry resembles the cap of a cylinder where $\mathbf{L \gg a \gg h_0}$. The conduit's cross section can be projected to a perfect circle due to interfacial forces since the flexible-walled conduits in this study are less than the conduit's capillary length (see Appendix 1). The conduit's projected radius **R** and the distance between the origin and the substrate's surface **b** are solved in terms of the cross section's centre height and half width ($\mathbf{h_0}$ and **a)** utilizing the following system of equations:

$$\boldsymbol{R = b + h_0} \tag{16}$$

$$\boldsymbol{b^2 + a^2 = R^2} \tag{17}$$

$$\boldsymbol{R = \frac{a^2 + h_0^2}{2h_0} \qquad b = \frac{a^2 - h_0^2}{2h_0}} \tag{18a-b}$$

It is also useful to derive a relationship to calculate the height of the conduit at any location across its half width, $\mathbf{h_z}$.

$$\boldsymbol{h_z = \sqrt{R^2 - z^2} - b} \tag{19}$$

At the centre of the conduit ($z = 0$) the conduit height is maximum and is represented as $\mathbf{h_0}$. At the conduit's pinning lines ($z = \pm \mathbf{a}$) its height is 0.

A conduit's footprint geometry (conduit half width **a** and length **L** in Figure 6a) are defined before SIM-printing and do not change when flow is applied. A conduit's centre-height $\mathbf{h_{0,x}}$, however, depends on the pressure gradient along a conduit's length due to flow. During

flow, a conduit's "flexible" walls (immiscible liquid-liquid interface) inflate locally according to the pressure drop defined in Equation 7 (see Figure 6b-c). Conduit heights increase with increased pressure and thus decrease in the direction of flow; $\mathbf{h_{0,x1}} < \mathbf{h_{0,x2}}$ (Figure 6c). Variable centre-heights along a conduit's length increases the difficulty of deriving important fluid dynamic characteristics such as local velocity and shear stress profiles. Unlike solid walled conduits traditionally used in PDMS-based microfluidics, open microfluidic conduit cross-sections change and cannot be modeled by existing methods.

4.3.1.2 Poiseuille Flow Between Two Infinite Parallel Plates

The conduit's only solid boundary in this study (the surface of a polystyrene Petri dish) satisfies the no-slip boundary condition for fluid flow (i.e., the magnitude of the flow's velocity along the dish's surface must be zero). The rest of the conduit, however, is confined by a layer of immiscible fluid (in the case of this study FC-40). Depending on the immiscible fluid's dynamic viscosity (as well as the fluid-fluid interface's rigidity), flow through the SIM-printed conduits can experience a varying level of slip along this non-solid interface. At one extreme, the liquid-liquid interface satisfies the no-slip boundary condition when the dynamic viscosity of the overlaying immiscible fluid nears infinity (see orange flow velocity field in Figure 7). At the other extreme, perfect-slip occurs when the dynamic viscosity of the overlaying immiscible fluid nears 0 (see purple flow velocity field in Figure 7). When both of these cases are solved for, a predicted conduit height profile for any possible ratio of dynamic viscosities must fall between these two extremes.

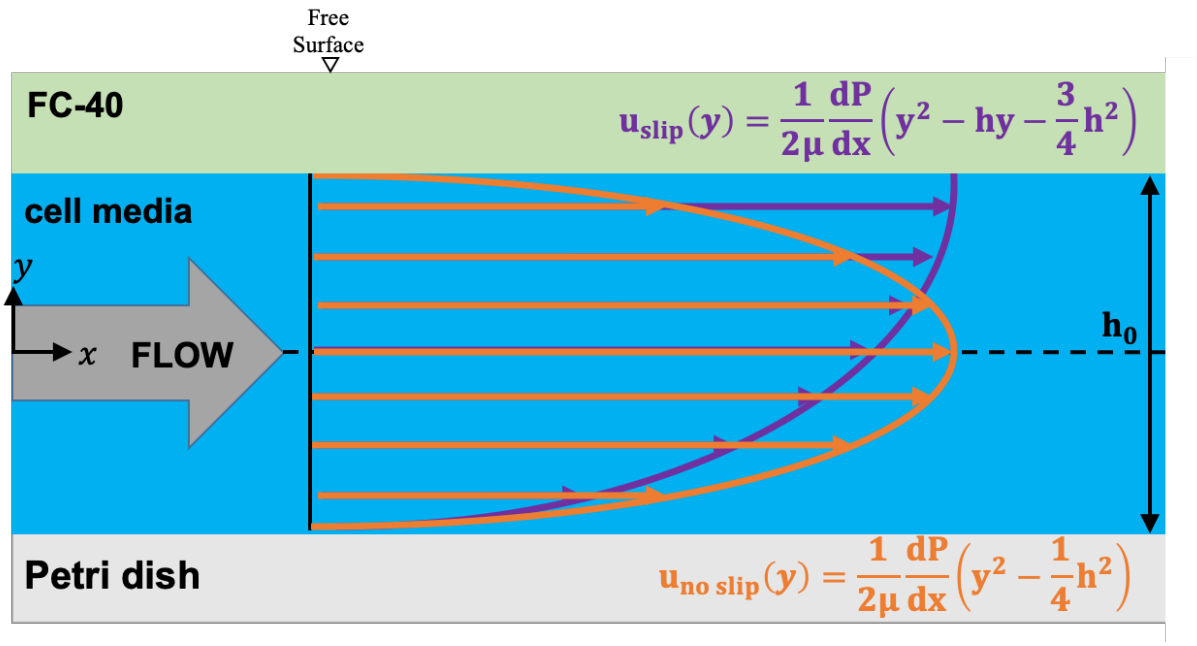

Figure 7. Schematic depicting flow velocity profile(s) within a SIM-printed conduit while applying two different boundary conditions. The orange velocity profile assumes no-slip at the media-fluorocarbon interface whereas the purple velocity profile assumes perfect-slip (for both cases, a no-slip boundary condition is applied at the Petri dish's surface). Experimental evidence supports the assumption of a no-slip boundary condition at the liquid-liquid interface.

4.3.1.2.1 No-Slip Boundary Condition at Media-Fluorocarbon Interface

Since there is ample experimental evidence that the media/fluorocarbon interface, albeit flexible in nature, is solid (see Supplemental Videos 3-5), the analytical solution will be derived assuming the media/fluorocarbon interface satisfies the no-slip boundary condition (for the case of perfect-slip, see Appendix 1). Furthermore, since conduits in this study are designed with the geometrical stipulation that $\mathbf{L} \gg \mathbf{a} \gg \mathbf{h_0}$, conduit flow can be approximated by modelling these microsystems as one-dimensional Poiseuille flow between two infinite parallel plates. Solving for a conduit's fully developed unidirectional velocity profile $\mathbf{u}(y)$ can be accomplished by integrating Equation 15 twice and applying the two following boundary conditions:

1. $\mathbf{u}\left(-\frac{\mathbf{h_0}}{2}\right) = \mathbf{u}\left(\frac{\mathbf{h_0}}{2}\right) = \mathbf{0}$
2. $\frac{\mathbf{du}}{\mathbf{dy}}(\mathbf{0}) = \mathbf{0}$

$\mathbf{u}(y)$ can then be expressed as follows:

$$\mathbf{u}(y) = \frac{\mathbf{1}}{\mathbf{2\mu}}\frac{\mathbf{dP}}{\mathbf{dx}}\left(\mathbf{y^2} - \frac{\mathbf{h_0^2}}{\mathbf{4}}\right) \tag{20}$$

In terms of the flow's maximum velocity $\mathbf{u_{max}} = -\frac{\mathbf{h_0^2}}{\mathbf{8\mu}}\frac{\mathbf{dP}}{\mathbf{dx}}$, the fluid velocity profile, gradient, and second derivative are defined as follows:

$$\mathbf{u(y)} = -\frac{\mathbf{4u_{max}}}{\mathbf{h_0^2}}\left(\mathbf{y^2} - \frac{\mathbf{h_0^2}}{\mathbf{4}}\right) \tag{21}$$

$$\frac{\mathbf{du}}{\mathbf{dy}} = -\frac{\mathbf{8u_{max}}}{\mathbf{h_0^2}}\mathbf{y} \tag{22}$$

$$\frac{\mathbf{d^2u}}{\mathbf{dy^2}} = -\frac{\mathbf{8u_{max}}}{\mathbf{h_0^2}} \tag{23}$$

Since Equation 15 states that $\frac{\mathbf{\partial P}}{\mathbf{\partial x}} = \mathbf{\mu}\frac{\mathbf{\partial^2 u}}{\mathbf{\partial y^2}}$ it follows that:

$$\frac{\mathbf{dP}}{\mathbf{dx}} = -\mathbf{\mu}\frac{\mathbf{8u_{max}}}{\mathbf{h_0^2}} \tag{24}$$

$$\frac{\mathbf{dP}}{\mathbf{dx}} \propto \frac{\mathbf{u_{max}}}{\mathbf{h_0^2}} \tag{25}$$

In the *z*-direction (across a conduit's width), $\frac{\mathbf{dP}}{\mathbf{dx}} = \mathbf{C}$ where $\mathbf{C}$ is some constant since the flow is assumed to be perfectly laminar (i.e., there is no pressure gradient, and thus no flow, in the *z*-direction). The following relationships can then be concluded to relate maximum flow velocities across a conduit's width to a conduit's maximum centre velocity:

$$\frac{\mathbf{u_{max(0)}}}{\mathbf{h_0^2}} = \frac{\mathbf{u_{max(z)}}}{\mathbf{h_z^2}} \tag{26}$$

$$\mathbf{u_{max(z)}} = \frac{\mathbf{u_{max(0)}}}{\mathbf{h_0^2}}\mathbf{h_z^2} \tag{27}$$

4.3.1.3 Normalized Flow Rate Coefficient

The volumetric flow rate $\mathbf{Q}$ through a conduit of any cross-sectional geometry is expressed by the following equation where $\bar{\mathbf{u}}$ is the mean flow velocity and $\mathbf{A}$ is the cross-sectional area of the conduit.

$$\mathbf{Q} = \bar{\mathbf{u}}\mathbf{A} \tag{28}$$

Volumetric flow rate can also be written in an integral form incorporating the flow's velocity profile defined in Equation 21.

$$\mathbf{Q} = \int_{-a}^{+a} \int_{-\frac{h_z}{2}}^{\frac{h_z}{2}} \mathbf{u}(y)\ \mathbf{dydz} \tag{29}$$

$$\mathbf{Q} = \int_{-a}^{+a} \frac{\mathbf{2}}{\mathbf{3}} \mathbf{u_{max(z)}} \mathbf{h_z}\ \mathbf{dz} \tag{30}$$

Substituting the relationship for $\mathbf{u_{max(z)}}$ from Equation 27:

$$\mathbf{Q} = \frac{\mathbf{2}}{\mathbf{3}} \frac{\mathbf{u_{max(0)}}}{\mathbf{h_0^2}} \int_{-a}^{+a} (\mathbf{h_z})^3\ \mathbf{dz} \tag{31}$$

Extracting constants from the integrand, utilizing the conduit's symmetry about its centre line, and substituting Equation 19 for $\mathbf{h_z}$ leaves the following relationship for volumetric flow rate:

$$\mathbf{Q} = \frac{\mathbf{4}}{\mathbf{3}} \frac{\mathbf{u_{max(0)}}}{\mathbf{h_0^2}} \int_{0}^{a} \left(\sqrt{\mathbf{R^2 - z^2}} - \mathbf{b}\right)^3\ \mathbf{dz} \tag{32}$$

As written in Equation 32, evaluating the integrand in order to solve for $\mathbf{h_0}$ can only be done so numerically in an iterative solution. Instead, the integrand can be normalized such that $\boldsymbol{\eta} = \frac{\mathbf{z}}{\mathbf{a}}$ and averaged over half-width to centre-height ratios which satisfy $\mathbf{a} \gg \mathbf{h_0}$:

$$Q = \frac{4}{3} h_0 u_{max} a \int_0^1 \frac{\left(\sqrt{R^2 - \eta^2 a^2} - b\right)^3}{h_0^3} d\eta \tag{33}$$

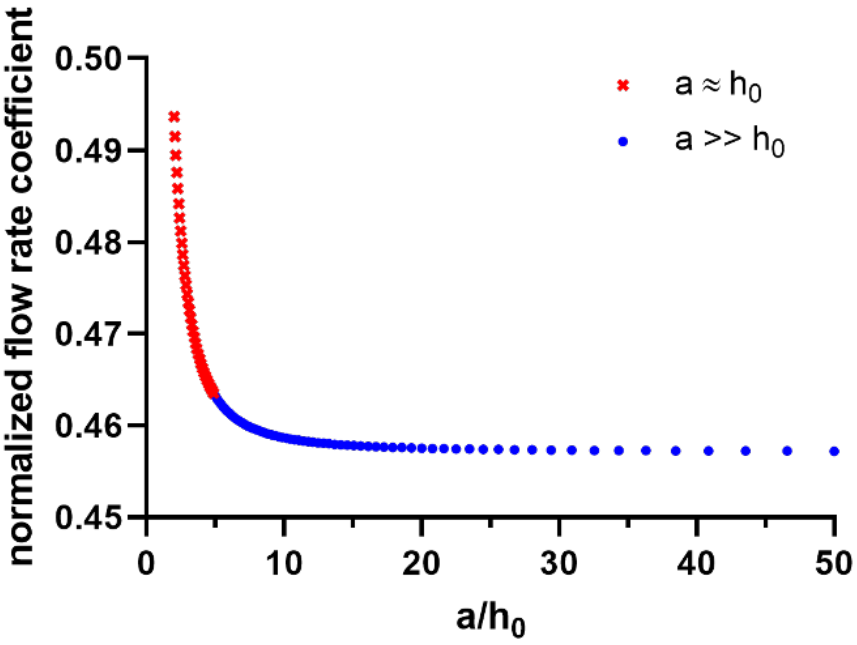

Figure 8. Numerically computed normalized volumetric flow rate coefficients across a range of fluid-walled conduit half width to height $\left(\frac{a}{h_0}\right)$ ratios. Conduit half width to height ratios less than 5 (conduits whose contact angle $\theta = 22.6^o$) are not considered in this derivation (see red symbols above). The blue symbols, however, represent conduit half width to height ratios typically experienced while operating the fluid-walled microcircuits studied in this thesis; this derivation assumes that $a >> h_0$.

The blue symbols in Figure 8 represent normalized flow rate coefficients in conduit's whose half width to height ratios satisfy $a >> h_0$. Conversely, the red symbols indicate half width to height ratios with contact angles approaching 90º; conduits of these geometries cannot be justifiably modeled as Poiseuille flow between two infinite parallel plates. Averaging the normalized coefficients across $\frac{a}{h_0}$ ratios which satisfy this flow approximation (0.4588) leaves the following evaluation of Equation 33:

$$Q = \frac{4}{3} h_0 u_{max} a(0.4588) \tag{34}$$

$$\mathbf{u_{max}} = \frac{\mathbf{Q}}{\mathbf{0.6118 h_0 a}} \tag{35}$$

Substituting the relationship for $\mathbf{u_{max}}$ derived from Poiseuille flow between two infinite parallel plates into Equation 35 produces:

$$\left(\frac{\mathbf{13.077 Q \mu}}{\mathbf{a}}\right)\mathbf{dx} = \left(\mathbf{h_0^3}\right)\mathbf{dP} \tag{36}$$

The radius of a conduit's cross-section is defined as $\mathbf{R} = \frac{\mathbf{a^2 + h_0^2}}{\mathbf{2h_0}}$ as derived in Equation 18a. However, since $\mathbf{a} \gg \mathbf{h_0}$ the following geometrical simplification can be made:

$$\mathbf{R} = \frac{\mathbf{a^2 + h_0^2}}{\mathbf{2h_0}} = \frac{\mathbf{a^2}}{\mathbf{2h_0}}\left(\mathbf{1} + \frac{\mathbf{h_0^2}}{\mathbf{a^2}}\right) \approx \frac{\mathbf{a^2}}{\mathbf{2h_0}} \tag{37}$$

The local pressure at any *x*-location along the length of a conduit can be characterized by the local Laplace pressure in accordance with the simplified Young-Laplace Equation for fluid volumes whose geometry represents the cap of long cylinders (see Equation 7). Utilizing the simplified cross-sectional radii of curvature expressed in Equation 37 produces the following equation defining local conduit pressure:

$$\mathbf{P} = \boldsymbol{\gamma}\left(\frac{\mathbf{1}}{\mathbf{R}}\right) \approx \boldsymbol{\gamma}\left(\frac{\mathbf{2h_0}}{\mathbf{a^2}}\right) \tag{38}$$

This remains true so long as the change is static pressure along the conduit's length is small relative to the change in Laplace pressure (see Appendix 1 for conduit capillary lengths). Local pressures from Equation 38 can then be solved in terms of local centre-heights $\mathbf{h_0}$, and then substituted into Equation 36 to allow for integration:

$$\left(\frac{\mathbf{13.077Q\mu}}{\mathbf{a}}\right)\mathbf{dx} = \left(\frac{\mathbf{a^6}}{\mathbf{8\gamma^3}}\mathbf{P^3}\right)\mathbf{dP} \tag{39}$$

Integrating produces the following solution:

$$\frac{\mathbf{13.077Q\mu x}}{\mathbf{a}} + \mathbf{C_1} = \frac{\mathbf{a^6}}{\mathbf{32\gamma^3}}\mathbf{P^4} \tag{40}$$

Reintroducing $\mathbf{P} \approx \boldsymbol{\gamma}\left(\frac{\mathbf{2h_0}}{\mathbf{a^2}}\right)$ back into Equation 40 and solving for $\mathbf{h_0}$:

$$\frac{\mathbf{26.154Q\mu ax}}{\boldsymbol{\gamma}} + \mathbf{C_1} = \mathbf{h_{0,x}^4} \tag{41}$$

Since at the conduit's exit ($x = 0$) $\mathbf{h} = \mathbf{h_{0,x=0}}$, $\mathbf{C_1} = \mathbf{h_{0,x=0}^4}$. Thus, the following equation predicting conduit centre-heights is produced.

$$\mathbf{h_{0,x}} = \left(\frac{\mathbf{26.154Q\mu ax}}{\boldsymbol{\gamma}} + \mathbf{h_{0,x=0}^4}\right)^{\mathbf{0.25}} \tag{42}$$

In terms of pressure drop down the length of a conduit:

$$\mathbf{P_x} = \left(\frac{\mathbf{418.464Q\mu\gamma^3 x}}{\mathbf{a^7}} + \mathbf{P_{x=0}^4}\right)^{\mathbf{0.25}} \tag{43}$$

Predicted conduit height profiles according to Equation 42 are depicted in Figure 9.

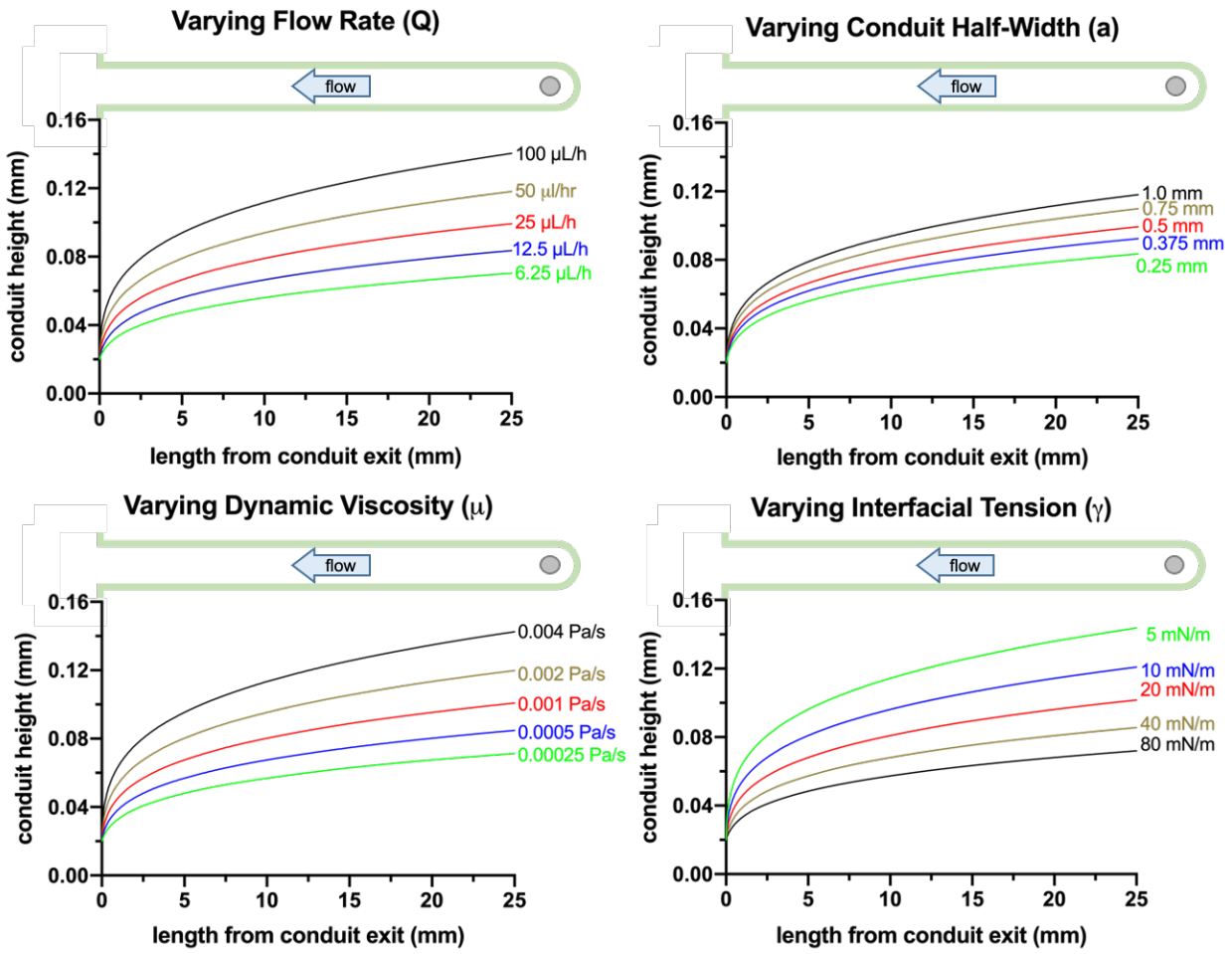

Figure 9. Analytical solution predictions of fluid-walled conduit centre heights while experiencing steady state active flow. Varying volumetric flow rate (top left), conduit half width (top right), or liquid characteristics such as dynamic viscosity (bottom left) and interfacial tension (bottom right) change predicted conduit height profiles in accordance with Equation 42. While one of the four variables is being changed above, all other variables are held constant at the median values represented by each respective variable's graph ($\mathbf{Q} = 25$ µl/h, $\mathbf{a} = 0.5$ mm, $\boldsymbol{\mu} = 0.001$ Pa·s, and $\boldsymbol{\gamma} = 22$ mN/m) Plots begin at the conduit's exit where the centre height is estimated to be 25 µm in agreement with average tissue culture Petri dish wetting thicknesses outlined in Appendix 2. Although only plotted for 25 mm, conduit height projections would continue indefinitely according to Equation 42 along the *x*-axis granted the conduit fits within its containment vessel (which in the case of this study is a 6 cm diameter tissue culture Petri dish). In practice, however, circuit failure would occur when a conduit's half width equaled its local centre height ($\mathbf{a} = \mathbf{h_{0,x}}$).

4.3.1.4 Importance of Conduit Exit Height ($\mathbf{h_{0,x=0}}$)

An ideal analytical solution that predicts flexible-walled flows through SIM-printed microcircuits requires as few difficult in-lab measurements (namely conduit height measurements) as possible. As written in Equation 42, conduit height profiles are predicted with only a single height measurement: the conduit's exit height ($\mathbf{h_{0,x=0}}$). To investigate if Equation 42 can be simplified further, consider the analytical solution's two individual terms which drive the conduit's height profile $\mathbf{h_{0,x}}$:

1. $\frac{\mathbf{26.154Q\mu ax}}{\boldsymbol{\gamma}}$
2. $\mathbf{h_{0,x=0}^4}$

When $\frac{\mathbf{26.154Q\mu ax}}{\boldsymbol{\gamma}} \gg \mathbf{h_{0,x=0}^4}$, the exit height (currently the only height measurement required to predict the rest of the conduit's height profile) becomes insignificant and can be set to zero. For a given fluid, flow rate, and conduit width, the location at which the two terms are equivalent should is determined using the following relationship:

$$\mathbf{x} = \frac{\mathbf{h_{0,x=0}^4 \gamma}}{\mathbf{26.154Q\mu a}} \tag{44}$$

For the flow modeled in Figure 10, $\mathbf{x} \approx 100$ μm when $\mathbf{h_{0,x=0}} = 25$ μm; the conduit's exit height only dominates height predictions for the first 100 microns! At a conservative distance from the conduit's exit (i.e., an order of magnitude greater than **x** from Equation 44) height predictions converge across a range of exit heights, including $\mathbf{h_{0,x=0}} = 0$ (see Figure 10). Thus, a simplified analytical solution requiring **no** in-lab height measurements can accurately predict flows:

$$\mathbf{h_{0,x}} = \left(\frac{\mathbf{26.154Q\mu ax}}{\boldsymbol{\gamma}}\right)^{\mathbf{0.25}} \tag{45}$$

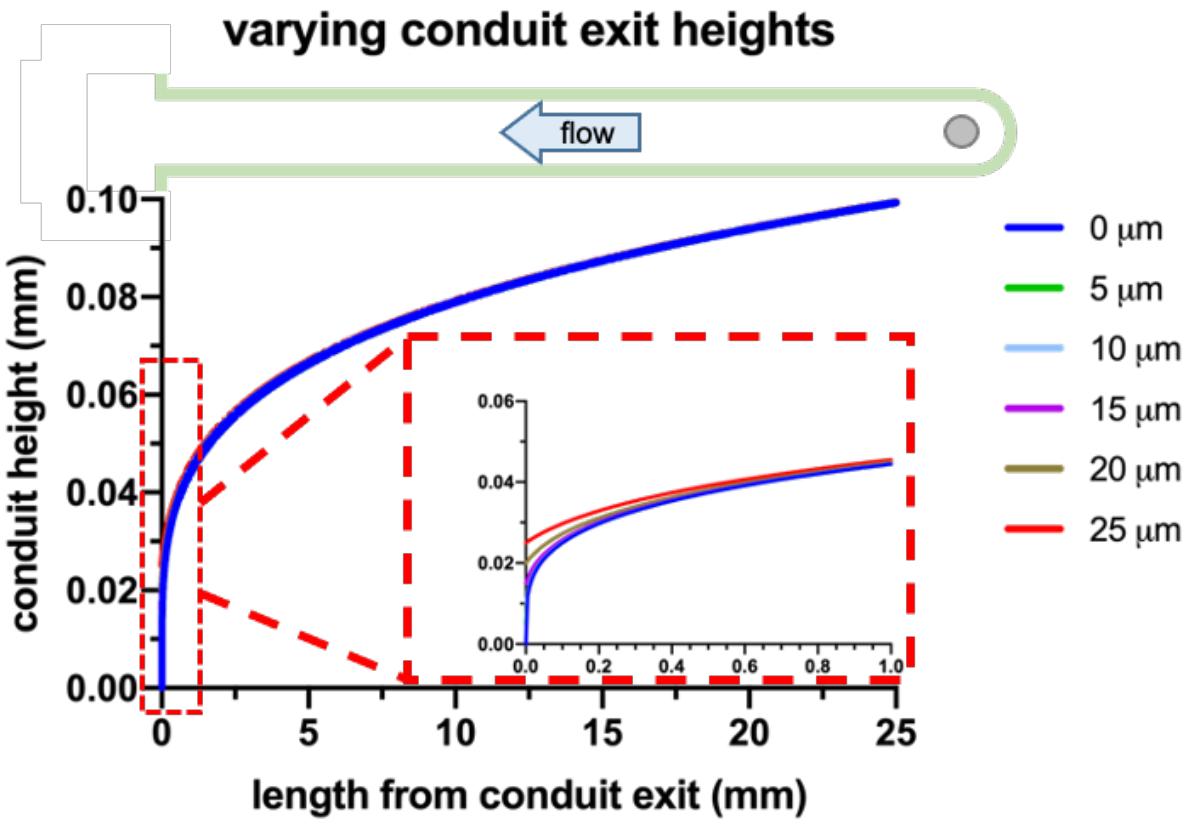

Figure 10. Analytically predicted conduit height profiles (Equation 42) using various exit heights ($\mathbf{h_{0,x=0}}$). All else being equal, conduit exit heights prove to be insignificant for a majority of a conduit's length if $\mathbf{h_{0,x=0}}$ is expected, at most, to be equal to average dish wetting thickness of cell media in tissue culture Petri dishes (~25 um). If $\mathbf{h_{0,x=0}}$ is assumed to be 0 um (although impossible in reality since this would cause a conduit to close at its end), height profile predictions tend to converge around 3 mm making $\mathbf{h_{0,x=0}}$ inconsequential to the majority of a conduit's height prediction. ($\mathbf{Q} = 25\,\frac{\mu L}{h}$, $\boldsymbol{\mu} = 0.00094$ Pa·s, $\mathbf{a} = 0.5$ mm, $\boldsymbol{\gamma} = 22$ mN/m)

4.3.1.5 Error from Conduit Geometry Simplifications

One source of error associated with the solution derived in the proceeding subchapters is error introduced during the geometrical simplification of a conduit's cross-sectional radius (Equation 37). Throughout the analytical derivation, a conduit's projected cross-sectional radius ($\mathbf{R}$) is calculated assuming $\mathbf{a} \gg \mathbf{h_0}$ which introduces an error term $\boldsymbol{\delta}$ equivalent to $\left(\mathbf{1} + \frac{\mathbf{h^2}}{\mathbf{a^2}}\right)$. This error ($\boldsymbol{\delta}$) can be implemented throughout the derivation from Equation 38 through the final analytical solution in Equation 42 resulting in the following familiar solution:

$$\mathbf{h_{0,x} = \left(\frac{26.154Q\mu a x}{\gamma}\delta + h_{0,x=0}^{4}\right)^{0.25}} \quad \textbf{(46)}$$

In terms of pressure drop down the length of a conduit, error associated with the conduit's radius simplification is as follows:

$$\mathbf{P_x = \left(\frac{418.464Q\mu\gamma^3 x}{a^7\delta^3} + P_{x=0}^{4}\right)^{0.25}} \quad \textbf{(47)}$$

The constant found in the analytical solution (26.154) is also subject to the error associated with the geometrical simplification of a conduit's cross-section as this constant is derived from the averaged normalized volumetric flow rate from Equation 33 only across half width to height ratios where $\mathbf{a \gg h_{0,x}}$.

4.3.2 Numerical Solution

The analytical solution derived in this chapter thus far is powerful for predicting height and shear profiles in simple flexible-walled conduits fabricated via SIM-printing. However, this solution is limited by geometrical assumptions made throughout its derivation (namely the averaged normalized volumetric flow rate used to produce the constant in Equation 34 and the conduit's cross-section radius simplification in Equation 37). A solution which is capable of numerically calculating cases where a conduit's geometry doesn't satisfy the approximation for Poiseuille flow between two parallel plates can be useful for examining conduits near failure (when $\mathbf{a = h_{0,x}}$) and can determine if the simplifications in the analytical derivation can be justified.

This flow problem's numerical solution used the same derivation as the analytical solution from Equation(s) 13-32 and only begins to deviate from the aforementioned solution at

Equation 33 when the volumetric flow rate is normalized. Instead, the following equation is solved for numerically at a given *x*-locations along the conduit's length (beginning at the conduit's exit when $\mathbf{h_{0,x} = h_{0,x=0}}$.

$$\mathbf{Q = \frac{2}{3}\frac{u_{max(0)}}{h_{0,x=0}^2}\int_{-a}^{a}\left(\sqrt{R^2 - z^2} - b\right)^3 dz} \tag{48}$$

The numerically determined value for the integrand in Equation 48 is a positive constant dependent only on the conduit's local cross-sectional geometry and will be represented by $\boldsymbol{\beta_{x=0}}$.

$$\mathbf{Q = \frac{2}{3}\left(\frac{u_{max(0)}}{h_{0,x=0}^2}\beta_{x=0}\right)} \tag{49}$$

Rearranging the equation above produces the following solution for a conduit's centre line maximum velocity $\mathbf{u_{max(0)}}$ at the conduit's exit:

$$\mathbf{u_{max(0)} = \frac{3}{2}\left(\frac{h_{0,x=0}^2 Q}{\beta_{x=0}}\right)} \tag{50}$$

4.3.2.1 An Iterative Solution to Conduit Height Predictions

The local pressure at any *x*-location along the length of a conduit can be characterized by the local Laplace pressure in accordance with the simplified Young-Laplace Equation for fluid volumes whose geometry represents the cap of long cylinders (see Equation 7). When substituting the conduit's radius of curvature at the conduit's exit ($\mathbf{R_{x=0}}$) from Equation 18a into the simplified Young-Laplace equation, the conduit's local pressure can be computed.

$$\mathbf{\Delta P_L = P_{x=0} = \frac{2\gamma h_{0,x=0}}{a^2 + h_{0,x=0}^2}} \tag{51}$$

After calculating the conduit's exit pressure, an iterative solution can be applied to solve for the local pressure an infinitesimally small distance $\mathbf{dx}$ upstream from the conduit's exit ($x = 0$).

$$\mathbf{P_{x=dx} = P_0 + \frac{dP}{dx} dx} \tag{52}$$

Substituting $-\frac{\mathbf{dP}}{\mathbf{dx}}$ from Equation 24,

$$\mathbf{P_{x=dx} = P_{x=0} + \mu \frac{8u_{max(0)}}{h_{0,x=0}^2} dx} \tag{53}$$

Substitute $\mathbf{u_{max(0)}}$ from Equation 50 produces the following expression for the conduit's local pressure at a distance **dx** from its exit ($\mathbf{P_{x=dx}}$):

$$\mathbf{P_{x=dx} = P_{x=0} + 12\mu \frac{Q}{\beta_{x=0}} dx} \tag{54}$$

Rearranging the Young-Laplace equation allows you to solve for the next cross-sectional radius some distance **dx** away from the conduit's exit ($\mathbf{R_{x=dx}}$). Following, the local pressure a distance **2dx** from the conduit's exit can be solved using the same principles outlined above.

$$\mathbf{R_{x=dx} = \frac{\gamma}{P_{x=dx}}} \tag{55}$$

$$\mathbf{P_{x=2dx} = P_{x=dx} + 12\mu \frac{Q}{\beta_{x=dx}} dx} \tag{56}$$

This iteration can continue for **n** steps (in the set $\mathbf{n} = \left\{1,2,3 \ldots \frac{L}{dx}\right\}$) along any conduit length **L** until the conduit's half width equals the conduit's local centre height (at which point the numerical solution, and the conduit, fail).

$$\mathbf{R_{x=dx(n-1)} = \frac{\gamma}{P_{x=dx(n-1)}}} \tag{57}$$

$$\mathbf{P_{x=n(dx)} = P_{x=dx(n-1)} + 12\mu \frac{Q}{\beta_{x=dx(n-1)}} dx} \tag{58}$$

Across geometries where $\mathbf{a \gg h_{0,x}}$ there is great agreement between the analytical and numerical solutions derived in this chapter (see Appendix 1).

4.3.3 Choked Conduit Height Predictions

Choking a conduit can be accomplished by attaching a smaller conduit known as a "choke" near a primary conduit's exit such that $\mathbf{a_{conduit} > a_{choke}}$ (see Figure 11a-b). Since the choke will bear a majority of the circuit's pressure drop, the primary conduit will have a relatively constant cross-sectional geometry along its length. While the choke and the primary conduit height profiles are defined by the analytical solution in Equation 42, the conduit-choke juncture requires further investigation. So long as the pressure head difference between the choke and the primary conduit is negligible, the Laplace pressure (and thus radii of curvatures) at the exit of the choke and the entrance of the primary conduit are assumed to be equal:

$$\mathbf{\Delta P_{L,conduit} = \Delta P_{L,choke} \quad \therefore \quad R_{conduit} = R_{choke}} \tag{59a-b}$$

Since both conduit's radii of curvatures are equal, the following can be concluded:

$$\mathbf{\frac{a_{conduit}^2 + h_{0,conduit}^2}{2h_{0,conduit}} = \frac{a_{choke}^2 + h_{0,choke}^2}{2h_{0,choke}}} \tag{60}$$

If the primary conduit and choke's half widths are known, as well as the choke's height, the conduit's height can be predicted using the following equation:

$$\mathbf{h_{0,conduit} = \frac{a_{choke}^2 + h_{0,choke}^2 - \sqrt{\left(a_{choke}^2 + h_{0,choke}^2\right)^2 - 4a_{condhit}^2 h_{0,choke}^2}}{2h_{0,choke}}} \tag{61}$$

When $\mathbf{a_{choke} \gg h_{0,choke}}$ and $\mathbf{a_{conduit} \gg h_{0,conduit}}$, $\mathbf{h_{0,conduit}}$ simplifies to:

$$\mathbf{h_{0,conduit} = \frac{a_{conduit}^2 h_{0,choke}}{a_{choke}^2}} \tag{62}$$

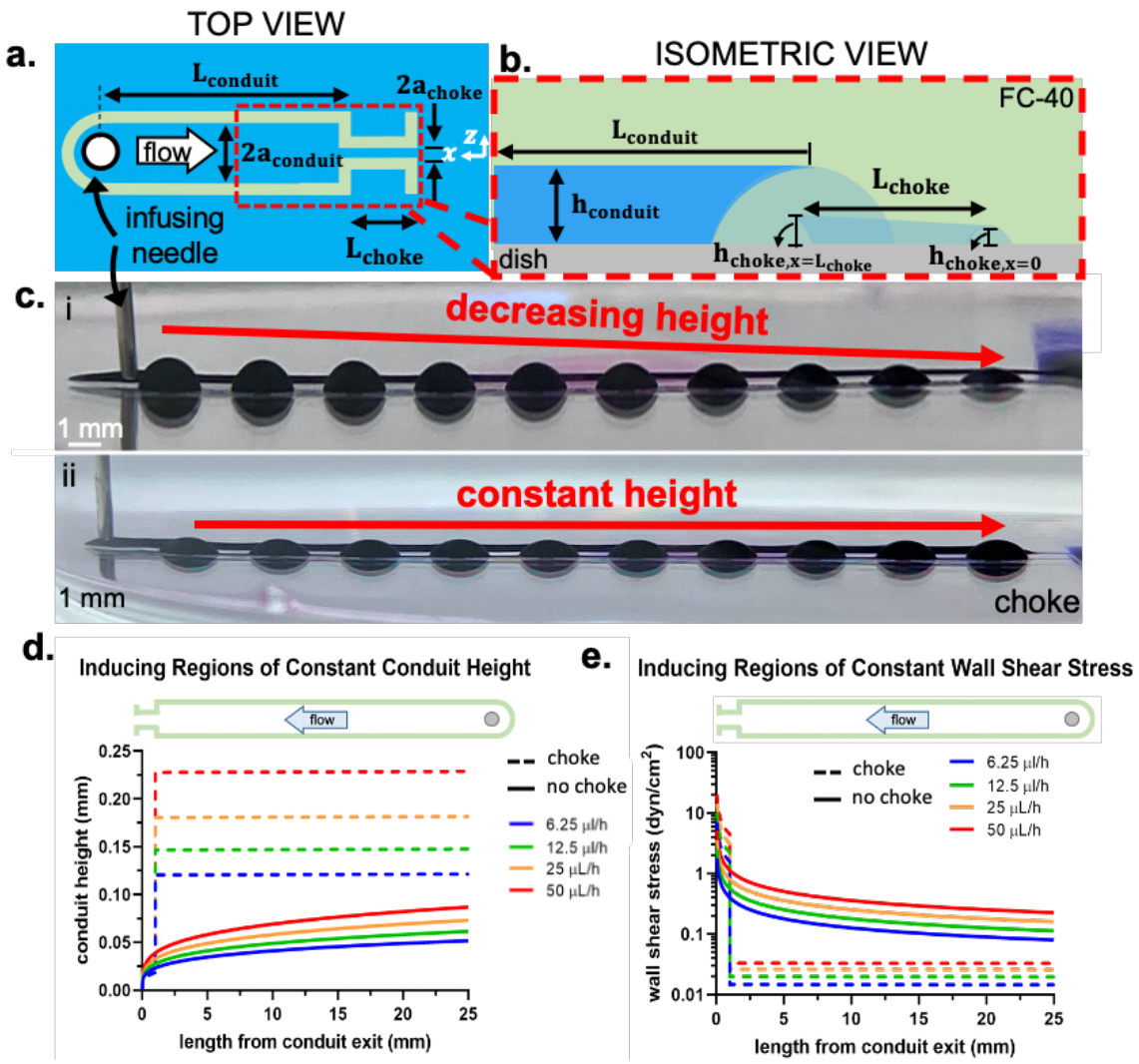

Figure 11. Choking circuits to create conduits of constant cross-sectional geometry. **a.** Plan of a SIM-printed choked conduit being pumped via an external syringe pump through an infusing needle. Flow exits the primary conduit into a smaller conduit (the "choke") where $\mathbf{a_{conduit}} > \mathbf{a_{choke}}$ and $\mathbf{L_{conduit}} > \mathbf{L_{choke}}$ to create a region of constant shear in the primary conduit. After exiting the choke ($x = 0$), flow joins the rest of the wetting fluid covering the surface of the Petri dish where $\mathbf{P_L} = 0$. **b.** Isometric view of choke attachment to the primary conduit. The choke's height changes in accordance with the flexible-walled conduit height profile defined in Equation 42 ($\mathbf{h_{choke,x=0}} < \mathbf{h_{choke,x=L_{choke}}}$). The height of the primary conduit, however, doesn't experience significant changes in height along its length ($\mathbf{h_{conduit}} \approx$ constant). **c.** Visual representation of conduit height changes in simple conduit (**i**) compared to choked conduit (**ii**) utilizing "pressure sinks" attached along the conduit's length. Each circular sink represents local conduit pressure (and thus cross-sectional geometry) along each conduit's length. The choked conduit shows a relatively constant height profile whereas the simple stand-alone conduit decreased in height in the direction of flow as expected. **d.** Plot of a 1 mm long choke ($\mathbf{a_{choke}} =$ 0.2 mm) attached at the exit of a primary conduit ($\mathbf{a_{conduit}} = 0.5$ mm) actively pumped with flow rates of 6.25, 12.5, 25, and 50 µL/h. Stand-alone conduit height profiles are included for comparison. **e.** Plot comparing center line wall shear profiles along a 25 mm long conduit.

5 Experimental Methods

5.1 Microfluidic Circuit Fabrication using a Submerged Impinging Microjet (SIM)

All microfluidic circuits discussed in this study are fabricated on sterile Corning® 6 cm tissue culture treated polystyrene Petri dishes using an iota Sciences fluidic printer. Although the fluidic printer is capable of forward and reverse printing (see Chapter 2.3), submerged impinging microjet (SIM) printing was the only printing technique used throughout all experiments presented in this thesis.

5.1.1 Dish Preparation

Identical operating procedure was conducted for the preparation of every Petri dish to ensure maximum repeatability. First, 1 ml of an aqueous-based wetting fluid (typically cell media) is deposited onto a virgin Petri dish. The dish is then gently shaken by hand until the dish's surface is completely wetted by a thin layer of the aqueous solution. Tilting the dish to a 30° angle, the excess wetting fluid pools to the dish's lower end due to gravity and is quickly removed with a pipette. Left behind on the Petri dish's surface is a thin, uniform coating of wetting fluid ~25 um thick (see Figure 27 in Appendix 2). This thin film is then overlaid by 1 ml of the immiscible, bioinert, and transparent fluorocarbon FC-40. (These dish preparation steps are depicted in Figure 3a)

5.1.2 Circuit Printing

The fluidic printer is a programmable three-axis traverse capable of fabricating almost any two-dimensional microfluidic circuit design on the surface of standard 6 cm Petri dishes. The traverse controls the movement of a submerged impinging microjet (70 μm needle) operating as a pressure washer which displaces regions of dish-wetting media. The microjet ejects the same fluorocarbon (FC-40) which overlays the thin aqueous wetting layer during dish

preparation and thus mixes freely with the bulk FC-40 after ejection from the microjet. Displacing regions of wetting media with the FC-40 microjet leaves liquid FC-40 "walls" which hold the remaining media in place via interfacial tension. (SIM-printing is depicted in Figure 3a.)

It is important to note that all fluids and materials used in the printing process are properly sterilized whether cells were incorporated into an experimental assay or not to ensure consistency between all tests. Likewise, an open flame is ideally present during dish preparation and circuit printing to preserve the system's sterility.

5.3.1 SIM-Print Resolution Experiments

The widths of SIM-printed FC-40 walls, defined as **w** in Figure 12a, are important when determining exact microfluidic circuit geometries. To understand the effects of user-controlled variables on SIM-printing resolution, FC-40 "walls" are measured while varying parameters such as microjet traversing speed across the *x*-*y* plane ($\mathbf{V_{jet}}$**),** volumetric flow rate (**Q**), height above a Petri dish's surface (**H**), and microjet inner diameter ($\mathbf{d_i}$). Linear FC-40 walls (15 mm in length) of alternating directionality with 2.0 mm gaps between each succeeding line are constructed in the pattern depicted in Figure 12a. For each subsequent 15 mm line, $\mathbf{V_{jet}}$ varies between 1 and 10 mm/s in increments of 1 mm/s and between 10 and 40 mm/s in increments of 5 mm/s. Three separate speed regimes (Table 3 in Appendix 2) were tested in separate dishes due to the size constraints of a single Petri dish. Three FC-40 walls constructed at a single $\mathbf{V_{jet}}$ speed were averaged on a single dish and each dish was repeated three times, thus resulting in nine total data points for every traverse speed considered. This not only accounts for differences across a single dish's surface, but also differences between independent dish preparations (primarily wetting thickness). Analogous test matrices were conducted for varying volumetric flow rates (**Q**) and microjet heights (**H**) in the same experimental fashion (see Table 3 in Appendix 2).

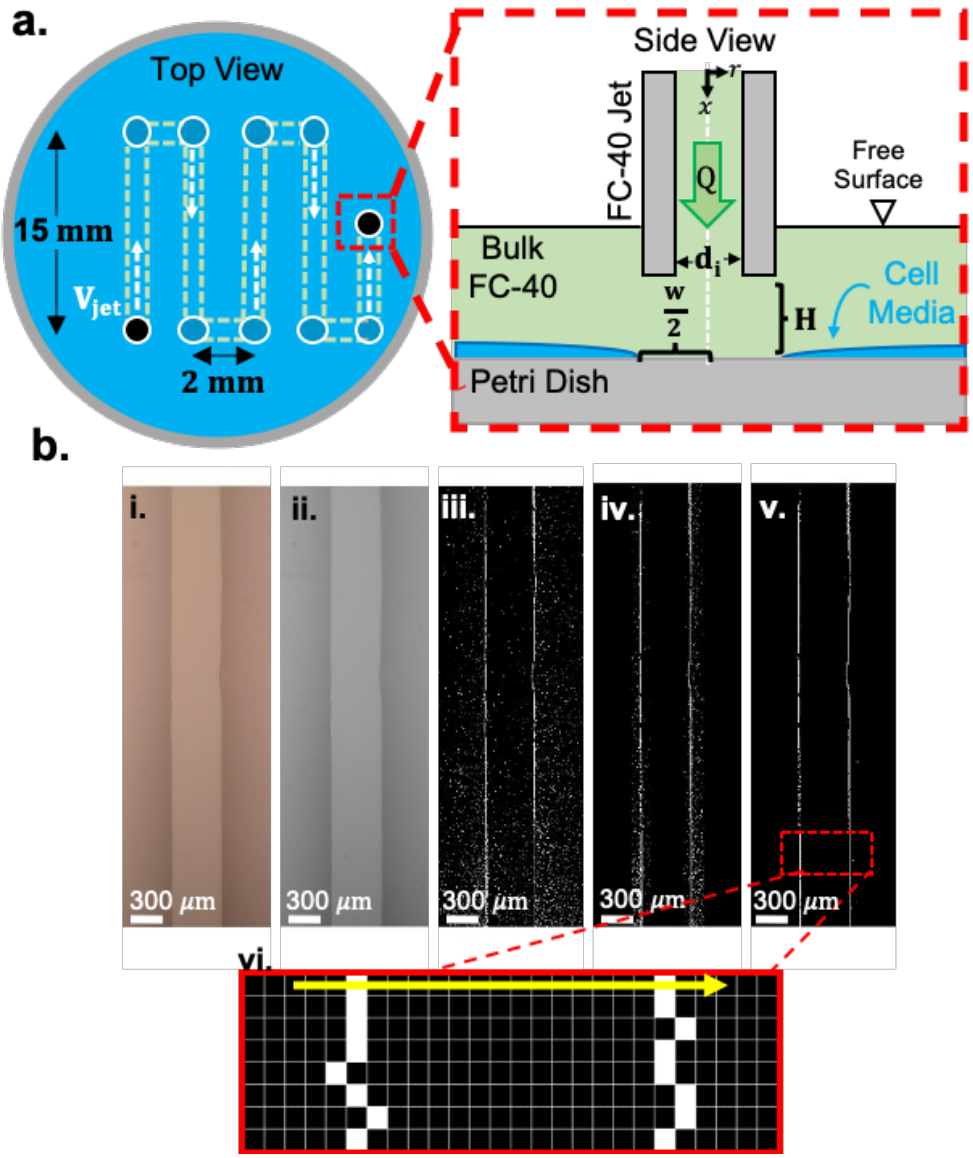

Figure 12. SIM-printing resolution measurements. **a.** SIM-printing technique used to determine average FC-40 wall widths (**w**) while varying user-controlled printer inputs. Top view image (left) shows the jet's traversing path across the surface of a Petri dish (*x*-*y* plane) with a speed $\mathbf{V_{jet}}$. 15 mm long lines are SIM-printed 2 mm away from one another in alternating directionality to determine average print resolution (i.e., FC-40 wall widths) for a specific jet traverse speed $\mathbf{V_{jet}}$, volumetric flow rate **Q**, height **H**, and microjet diameter $\mathbf{d_i}$. The side view (right) shows the microjet traversing into the page creating a 15 mm long FC-40 wall. **b.** SIM-printed FC-40 wall width image analysis **i.** After 15 mm FC-40 walls are constructed using the method outlined in **a**, an image is taken on a microscope. **ii.** Image is converted into grayscale. **iii.** A vertical Sobel Operator kernel convolutes the grayscale image into a binary image. **iv.** A new image is generated focusing on pixels closest to the perceived media-fluorocarbon pinning lines. **v.** Noise surrounding the pinning lines is removed. **vi.** Distances between the leftmost and rightmost white pixels are iteratively measured and then averaged along the FC-40 wall's length.

After jetting has concluded in a particular dish, FC-40 wall widths are immediately photographed using a DMK 41BU02 USB Camera attached to an Olympus CK40 microscope. A phase contrast (10x magnification) microscope objective and condenser annulus were used to maximize image quality. To determine FC-40 wall widths (**w**), the line detection image analysis approach outlined in Figure 12b was used. First, an image of each FC-40 wall is converted into grayscale. In this grayscale format, each individual pixel is given a value between 0 and 1.0 to represent a specific pixel's relative intensity compared to neighboring pixels. Attributing pixel intensities allows for pixel gradient detection to find pinning lines (areas with the highest rates of change in pixel intensity correspond to lines in an otherwise clear image). A vertical Sobel Operator kernel is then applied to convert the image from greyscale to binary. After surrounding noise is removed, widths are iteratively measured and averaged to determine **w**.

5.2 Pendant Drop Tensiometry

Pendant Drop Tensiometry was the first method used to measure interfacial tension between FC-40 and various aqueous-based cell media solutions. A First Ten Angstroms' 1000B Manual Drop Shape Analyzer (Model B 23A 110) along with a Point Grey Firefly® MV USB camera shown in Figure 13a,i-ii are the pendant drop tensiometry rig and camera respectively. A PhD Ultra Harvard Apparatus pump was added to the rig in lieu of the less accurate manually controlled pump shown in Figure 13a,iii to control drop setting for all experiments.

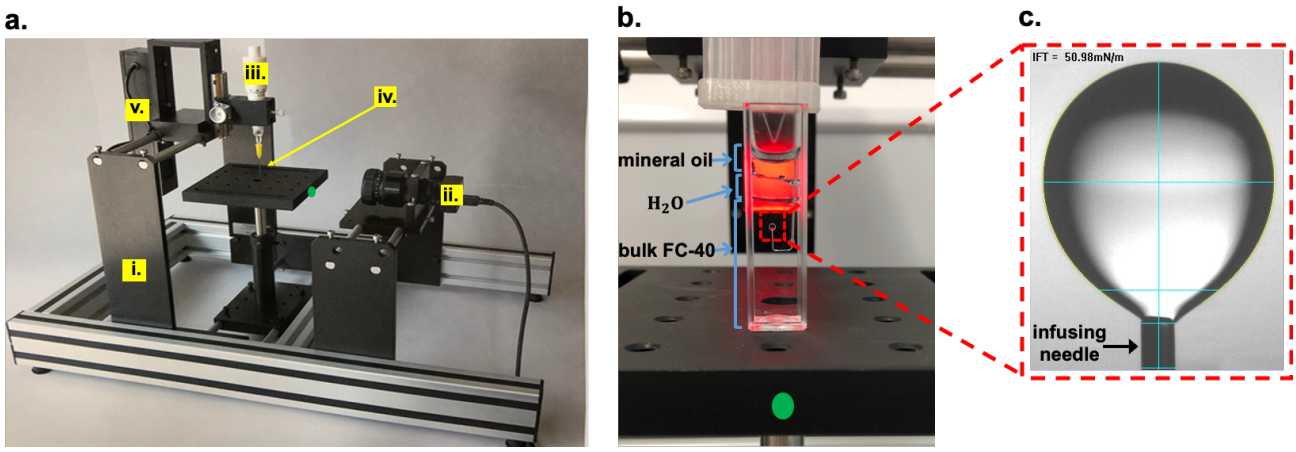

Figure 13. Pendant Drop Tensiometry. **a.** Experimental rig. **i.** First Ten Angstroms' 1000B Manual Drop Shape Analyzer (Model B 23A 110). **ii**. Point Grey Firefly® MV USB camera. **iii.** Manually controlled drop infuser (replaced by a PhD Ultra Harvard Apparatus pump for increased accuracy). **iv.** Capillary tip. **v.** Red LED Backlight. **b.** Pendant drop control setup (floating up orientation). A 1.4 µL H_2O droplet, dispensed by a 34G needle, is completely submerged in bulk FC-40 which is contained by a 2.5 mL translucent cuvette. A layer of water, covered by a layer of mineral oil, is deposited on top of the FC-40 bulk to prevent long term evaporation. **c.** Image analysis of the droplet in **b**; $\boldsymbol{\gamma} = 50.98$ mN/m. The outside diameter of the infusing 34G needle ($\mathbf{d_o} = 0.25$ mm) is used as a length scale for image analysis software.

As outlined in Chapter 4.2.2.1 the continuous phase and the drop phase used in Pendant Drop Tensiometry need to be strategically selected to yield the desired drop orientation (hanging down or floating up). In this study, FC-40 was selected as the continuous phase whereas various aqueous-based cell media solutions (primarily DMEM + 10% FBS) was the drop phase. Consequently, the "drop floating up" orientation (Figure 13c) was utilized since $\boldsymbol{\rho_{FC40} > \rho_{media}}$.

Experimental setup begins with depositing 1.5 mL FC-40 in a translucent 2.5 mL disposable cuvette. A layer of water is added to the top of the bulk FC-40 and then a layer of mineral oil is added on top of the water to help prevent evaporation over long testing periods; although FC-40 slows the evaporation of a covered aqueous-based solution significantly compared to leaving the solution open to the atmosphere, evaporation does become significant for tests that last days or weeks (see Figure 28 in Appendix 2). Sterile aqueous media solution is then carefully loaded into a 50 µL Hamilton syringe. For accurate interfacial tension results, it is

crucial that the syringe is bereft of any dust particles and the fluid it contains is absent of all bubbles. To ensure a clean fluid exchange system, anything which comes in contact with the drop fluid is thoroughly cleansed by a 70% ethanol solution and set to dry. Once dry, a systematic syringe loading procedure is conducted to ensure no bubbles are left within the system. The syringe is then attached to a 34G needle ($\mathbf{d_o}$ = 0.25 mm, $\mathbf{d_i}$ = 70 μm) via chemically inert Polytetrafluoroethylene (PTFE) sub-light walled tubing. Once the syringe is properly loaded into the Harvard Apparatus pump and the needle is fully submerged into the FC-40 (with the needle tip a safe distance from the insulating water/mineral oil layers) a drop can be set by infusing a desired volume.

Once a drop is set, camera focus and LED backlight intensity can be adjusted; high contrast along the edge of the drop and needle tip (see Figure 13c) is necessary for accurate interfacial tension measurements. Both software and rig calibrations are required to ensure accurate drop analysis, and thus, accurate interfacial tension readings. The software calibrates to the length scale of the experimental setup by analyzing an image of the needle tip. With a known needle tip's outer diameter and the two liquid phase's densities, the software is able to accurately calculate the system's interfacial tension. FC-40 and sterile-filtered H_2O suitable for cell culture are used as control fluids for system calibration since their interfacial tension (52.06 ± 0.66 mN/m) and liquid densities (1855 kg/m^3 and 997 kg/m^3 respectively) are widely accepted in the literature [57]. Interfacial tension measurements from three separate H_2O drops in FC-40 are averaged and compared to interfacial tension measurements accepted in literature to ensure the system is operating correctly.

5.3 Active Flowing Circuit Experimentation

After a circuit is fabricated on the surface of a Petri dish using SIM-printing, media can be pumped through the fluid-walled arrangement analogous to how fluid is pumped through a traditional solid-walled PDMS-based microfluidic device. Pumping can either be accomplished passively by engineering a predetermined pressure gradient throughout the circuit (see Figure 26 in Appendix 1) or actively via an external syringe pump. In order to study the fundamental fluid dynamics in these fluid-walled microsystems, active flow is induced to ensure a constant volumetric flow rate, pressure gradient, and height geometry over time once steady state flow is achieved.

A Petri dish with a linear, 30 mm long SIM-printed conduit is placed onto the stage of a Zeiss Axio Observer inverted microscopy system as in Figure 14a. The microscope's stage is attached to a three-axis traverse and is controlled manually by a joystick. A digital readout of the stage's x, y and z coordinates directly under the objective gives users the ability to accurately measure conduit geometries; the x and z directions gives single micron accuracy whereas the y coordinate (driven by focusing the objective) provides sub-micron accuracy. A Zeiss Definite Focus system is also attached to the microscope to minimize objective drift and ensure precise focusing, especially in the y direction. Once the dish is secured onto the stage, an infusing needle attached to an external Harvard Apparatus syringe pump is carefully inserted into the centre of the conduit's closed end. Much care is taken in the placement of this needle since failure during infusion is more likely to occur if accidentally placed onto the conduit's pinning lines. Once the position of the needle is verified via the microscope, infusing can begin. The external pump is loaded with a 250 µL syringe containing a 1/1000 concentration of 0.5 µm diameter red-fluorescing FluoSphere® beads in carboxylate solution mixed with sterile DMEM + 10% FBS.

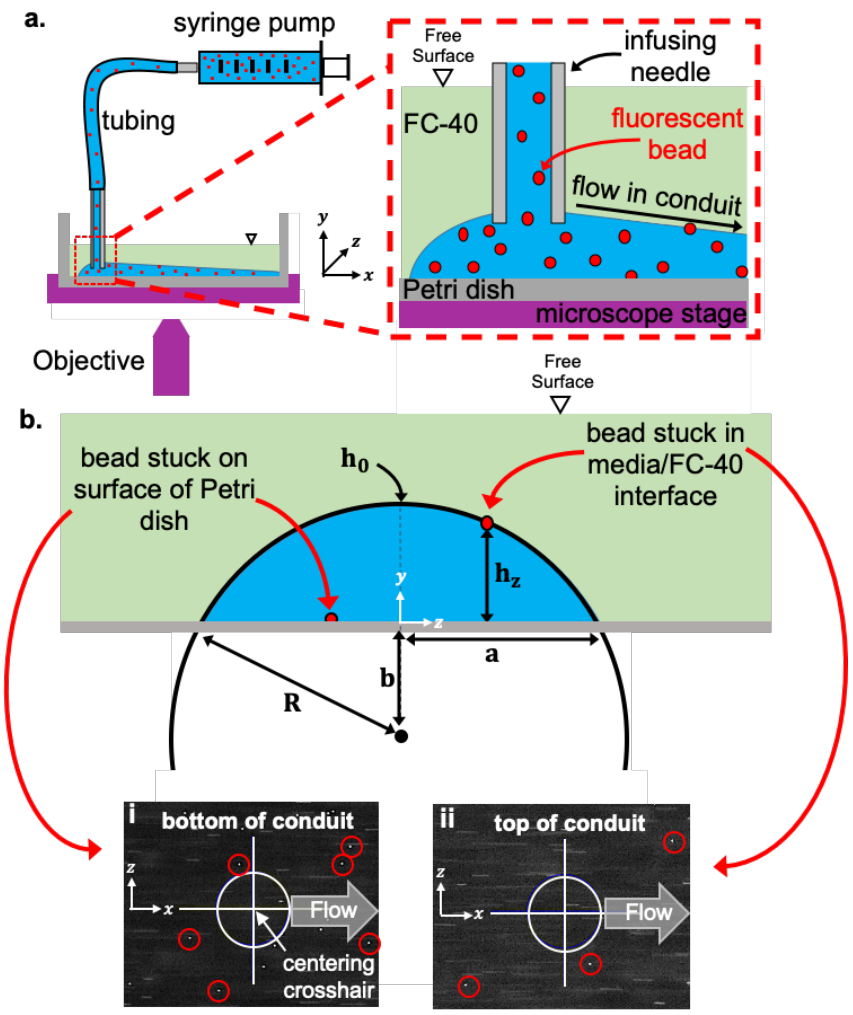

Figure 14. Experimental setup to characterize active flowing SIM-printed circuit geometries. **a.** A Petri dish containing a SIM-printed conduit is placed onto a Zeiss Axio Observer inverted microscope stage whose three-dimensional movement is manually controlled via a joystick. A needle attached to an external syringe pump is placed into the closed end of the conduit and pumped with a 1/1000 solution of 0.5 μm diameter red fluorescent beads in cell media until steady state is achieved; conduit height decreases in the direction of flow. **b.** Conduit heights are measured by focusing the microscope objective on (**i**) beads stuck on the surface of the Petri dish and (**ii**) beads stuck in the fluorocarbon-media interface. The *y* coordinates of each pair of beads are subtracted from one another, giving $\mathbf{h_z}$ for a given *x* location along the conduit's length. Due to conduit symmetry about the *y*-axis, a geometrical adjustment is then applied to this measurement to give the centre-height of the conduit ($\mathbf{h_0}$).

While the time required to reach steady state is dependent on flow rate and conduit geometry, a conservative threshold of thirty minutes after beginning infusion was allotted for each experiment to reach equilibrium. This also provided sufficient time for beads to stick to the media-fluorocarbon interface and the surface of the Petri dish. Once active flow has persisted

without interruption for thirty minutes, conduit height measurements are recorded. Flow is continually pumped during the entirety of data acquisition to ensure steady state is properly maintained.

5.3.1 Conduit Height Measurements

First, the conduit's exit coordinate is recorded; measurements down the conduit's length will be in reference to this exit location ($x = 0$). Then, the stage is moved in 0.5 mm increments down the length of the conduit finding static fluorescent beads which have become stuck to the media-fluorocarbon interface during flow (see Figure 14b). Once a bead near the 0.5 mm step is in focus, its *x*, *y*, and *z* coordinates are recorded. Without moving in the *x* or *z* direction, the stage is raised in the *y* direction to now focus on the surface of the dish **directly** below the bead stuck to the interface; the *y* coordinate is recorded once a bead stuck on the surface of the dish is perfectly in focus. The difference between the *y* coordinates of these two beads produces the conduit's height $\mathbf{h_z}$. The measured heights are subsequently multiplied by a constant to account for the mismatch between cell media and air's refractive indices. Finally, the left and right bounds of the conduit (its footprint pinning lines) are recorded to give a precise conduit half width (**a**) at this location.

This process is repeated in 0.5 mm increments for the first 5 mm of the conduit length, and then in 1.0 mm increments for the next 20 mm. Data resolution is twice as high during the first 5 mm because a conduit's height gradient is greatest near its exit (see Chapter 4.3.1.3). Although all conduits in this study are 30 mm long, sufficient distance is given from the *x*-location of the infusing needle (around 5 mm) as to not include height variations due to the needle itself (as the needle is hydrophilic, the aqueous-based circuit tends to climb the needle via capillary action).

6 Results

6.1 SIM-Printing Resolution

One advantage SIM-printing boasts over existing open-microfluidic fabrication techniques (i.e., forward [27] and reverse [28] printing) is its control over print resolution. While the widths of fluid walls constructed by forward and reverse printing are limited by the diameter of the infusing needle and the size and shape of the stylus respectively, wall widths constructed by SIM-printing can be controlled by varying the following SIM parameters:

1. The microjet's volumetric flow rate (**Q**)
2. The microjet's traverse-controlled velocity across the substrate's surface ($\mathbf{V_{jet}}$)
3. The microjet's height above substrate's surface (**H**)

The volumetric flow rate (**Q**) is the most sensitive variable in determining SIM-print resolution and varies linearly with wall widths (Figure 15a). As discussed in Chapter 4.1.3, the primary mode of a SIM's liquid-film displacement in the impingement region is the pressure force created by the jet's flow; the higher the flow rate (and thus the higher the jet stream's momentum), the higher the jet's media-displacement power. Wall widths vary according to microjet diameters for similar reasons; for a given flow rate, a jet stream's average velocity (and thus momentum) increases with decreasing internal diameter (Equation 28). Although an increase in jet-stream velocity increases the jet's media-displacement power, it also reduces repeatability; the standard deviation of SIM-printed FC-40 wall widths increases significantly with a 60 μm microjet at flow rates greater than 15 μl/s (Figure 15a).

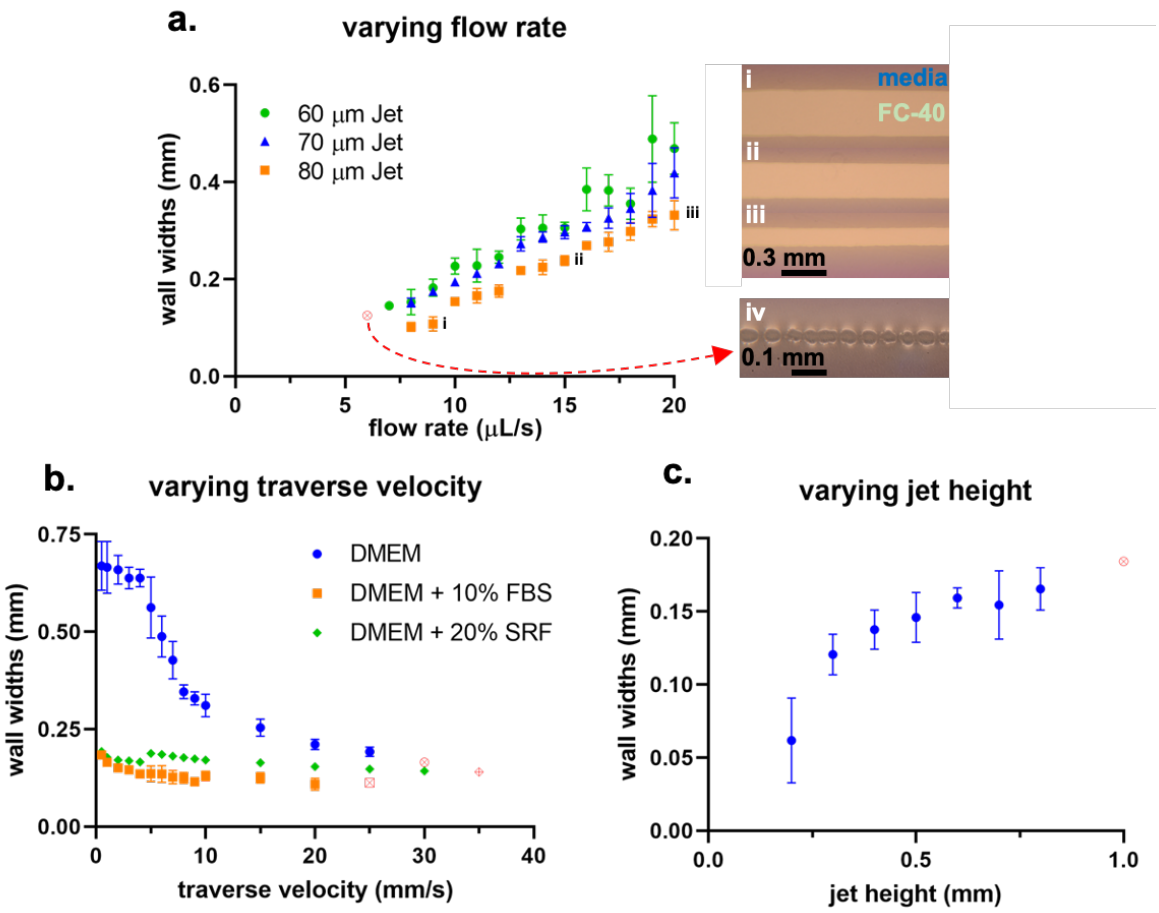

Figure 15. Widths of fluid FC-40 walls created by SIM-printing. All tests unless specified otherwise were conducted using a 70 µm jet and DMEM + 10% FBS wetted substrates. While one printing variable is altered, the others are held constant at the following volumetric flow rate, traverse velocity and jet height: 10 µl/s, 8 mm/s and 0.5 mm respectively. **a.** Varying volumetric flow rate using jet nozzles with different diameters. Insets: example images of wall widths using the 80 µm nozzle. Wall widths increase with increasing flow rate (inset **i-iii**) and decreasing nozzle diameter. SIM-printing fails with the 60 µm nozzle at $\mathbf{Q} = 7$ µl/s (inset **iv**). **b.** Varying traverse velocity and dish-wetting media solution. Increasing the jet's traversing velocity and adding serum (or serum replacement) decreases widths. **c.** Varying jet height above the Petri-dish surface. Increasing the jet's height increases (until failure) wall widths.

Print-failure occurs at low flow rates when the jet is unable to consistently produce constant, linear FC-40 walls. For example, at least half of the walls printed with the 60 µm needle at 7 µl/s produced fragmented walls (red symbol in Figure 15a). As aqueous phase leaks through such fragmented walls, such flow rates should not be used for fabricating microfluidic arrangements. No continuous walls were fabricated below the values shown in Figure 15a.

FC-40 wall widths decrease as the SIM's traversing speed ($\mathbf{V_{jet}}$) increases (Figure 15b) and depends on the presence of serum (or serum replacement) in the media. With media containing serum, walls are successfully fabricated using traverse speeds as great as 20 mm/s; use of higher traverse velocities increases the risk of print-failure significantly and so is not recommended. When serum or serum replacement is not added to media, FC-40 wall geometry becomes more unpredictable and lacks repeatability. Several other media used in cell biology, as well as blue dye solution not suitable for cell culture, were also tested (Figure 29 in Appendix 2).

Jet height (measured from the jet orifice to the surface of the Petri dish) also affects wall widths; as jet heights increase, wall widths increase (Figure 15c). As Figure 4a shows, a submerged jet spreads radially the farther it travels from the orifice. This radial spreading subsequently increases the impingement zone, enabling the jet to sweep media off a larger area of the substrate. At 1 mm from the surface, jet velocity slows sufficiently so that continuous walls do not form. When printing with a 70 μm needle through DMEM + 10% FBS, the following "nominal" SIM-parameters are recommended to avoid print failure (i.e., broken FC-40 walls leading to leaks and cross-contamination): $\mathbf{Q} = 10$ μl/s, $\mathbf{V_{jet}} = 8$ mm/s and $\mathbf{H} = 0.5$ mm.

Error between tests (each datum in Figure 15a-c are averaged between 9 wall widths) is primarily due to differences between individual Petri dish preparation and surface geometries. The average media wetting thickness across a Petri dish's surface is sensitive to the dish preparation procedure outline in Chapter 5.1.1; a dish's tilt angle, time of media-wetting, and evaporation all play a role in film thickness (see Figure 27 in Appendix 2). Additionally, media thickness (although assumed constant across the dish's surface) is affected by Petri dish surface concavity which leads to media pooling along a dish's perimeter. Moreover, surface concavity is not consistent between identical Petri dishes (see Figure 30 in Appendix 2).

6.2 Shear in Wetting Fluids

To investigate the boundary condition at the media-fluorocarbon interface, wetting fluids were seeded with 3-10 μm glass beads, and movies were made (using a microscope) to examine flow within the various wetting fluids as a microjet ejects FC-40 (see Supplemental Videos 1-5).

6.2.1 Media without Serum

For wetting solutions without serum (or serum replacement), there is ample evidence of slip at the media-fluorocarbon interface. While observing a stationary FC-40 microjet impinging through a layer of DMEM seeded with beads, the beads spin due to shear-induced vorticity (Supplemental Video 1); two of the observed vortices (diagonal from one another) spin clockwise, while the remaining two vortices spin counter-clockwise akin to Taylor-Green vortices. Similar vortices form when SIM-printing DMEM circuits. For instance, if you place the microjet in the centre of a grid such as in Figure 16, the vortices will form in their typical quadrants, although this time constrained by the chamber's pinning lines (Supplemental Video 2). For wetting fluids which do not contain serum, jetting can be used as an effective method for mixing the contents of SIM-printed chambers (i.e., beads, cells, etc.).

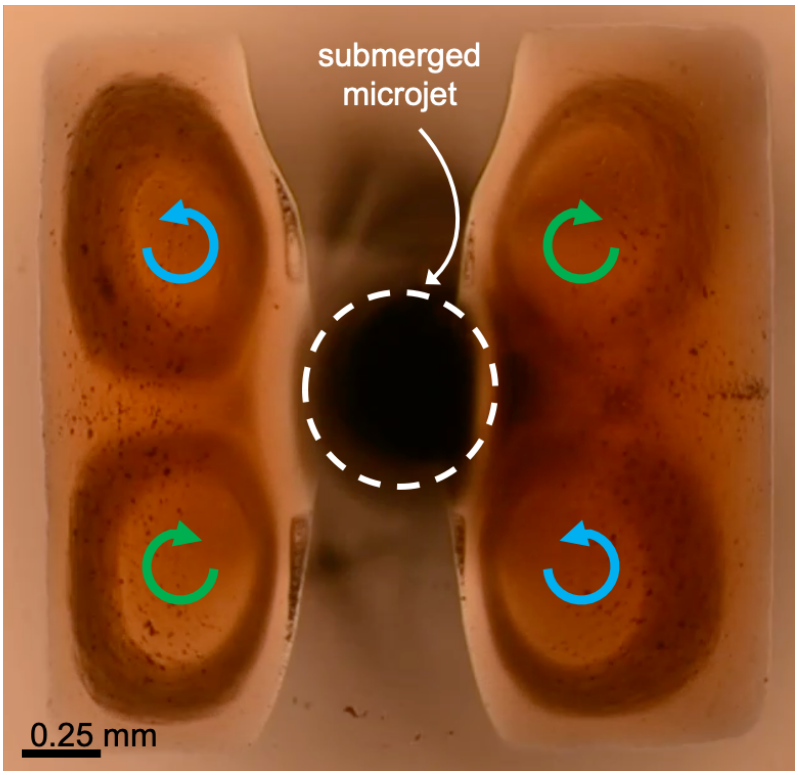

Figure 16. Shear induced vorticity within SIM-printed 1.9 x 1.9 mm DMEM chamber (3-10 µm beads and red dye added for visibility) observed from underneath a tissue culture Petri dish. A submerged 70 µm jet ejecting FC-40 impacts the Petri dish's surface at the centre of the image above, and then flows radially as the jet enters the 'Wall Jet' regime. As ejected FC-40 flows across the surface of the DMEM chamber, the beads circulate in four distinct vortices of alternating directionality (green arrows represent clockwise vorticity while blue arrows represent counter-clockwise vorticity). For full video, see Supplemental Video 2.

6.2.2 Media with Serum

The addition of serum (or serum replacement) to DMEM eliminates all shear-induced flow within the dish-wetting solution by producing a no-slip boundary condition at the media-fluorocarbon interface. As Supplemental Video 3 shows, there is no evidence of vorticity in the aqueous phase (DMEM + 10% FBS) as the beads now remain stationary upon jet impingement. Similarly, if the microjet is again positioned centrally above a chamber (now made of DMEM + 10% FBS), beads also remain stationary. Instead of mixing the contents of a chamber, traversing

the jet across a chamber's surface causes beads to congregate along the jet's path and thus provides users with a method of patterning the contents of chambers (see Supplemental Video 4).

The no-slip boundary condition serum creates is not a product of time or environment (i.e., incubation) as shear-induced flow within a DMEM chamber stops almost immediately after adding serum. In Supplemental Videos 5, an FC-40 microjet is placed between two adjacent DMEM chambers seeded with beads (no serum) and shear-induced flow is observed as expected. However, seconds after adding 0.5 μL of DMEM + 10% FBS to the bottom chamber, flow within that chamber stops.

6.3 Interfacial Tension Measurements

When examining two immiscible liquids using pendant drop tensiometry, droplet geometry (and thus interfacial tension) remain constant over time. For instance, a water droplet in FC-40 (Figure 17a) remains attached to its capillary indefinitely in the absence of external agitation while interfacial tension remains constant in the absence of contamination (i.e., addition of surfactants). The geometry of a DMEM + 10% FBS droplet in FC-40, however, changes significantly, tending to "neck" over time reminiscent a ductile metal's tensile deformation under axial strain (Figure 17b). In addition to the absence of shear experienced in DMEM + 10% FBS wetting films (Chapter 6.2.2), this necking is consistent with a semi-elastic membrane forming at the media-fluorocarbon interface. Instead of forming a liquid-liquid interface with FC-40, DMEM + 10% FBS droplets behave as elastic capsules (i.e., two phase systems which form elastic, solid-like membranes at liquid-liquid interfaces [58]–[62]). Since pendant drop tensiometry fails to consider the elastic stresses within a capsule's membrane, interfacial tension measurements using this method are inaccurate [62]. From pendant drop tensiometry, $\boldsymbol{\gamma_{PDT}} = 34.82 \pm 0.74$ mN/m when a DMEM + 10% FBS droplet is first formed in FC-40.

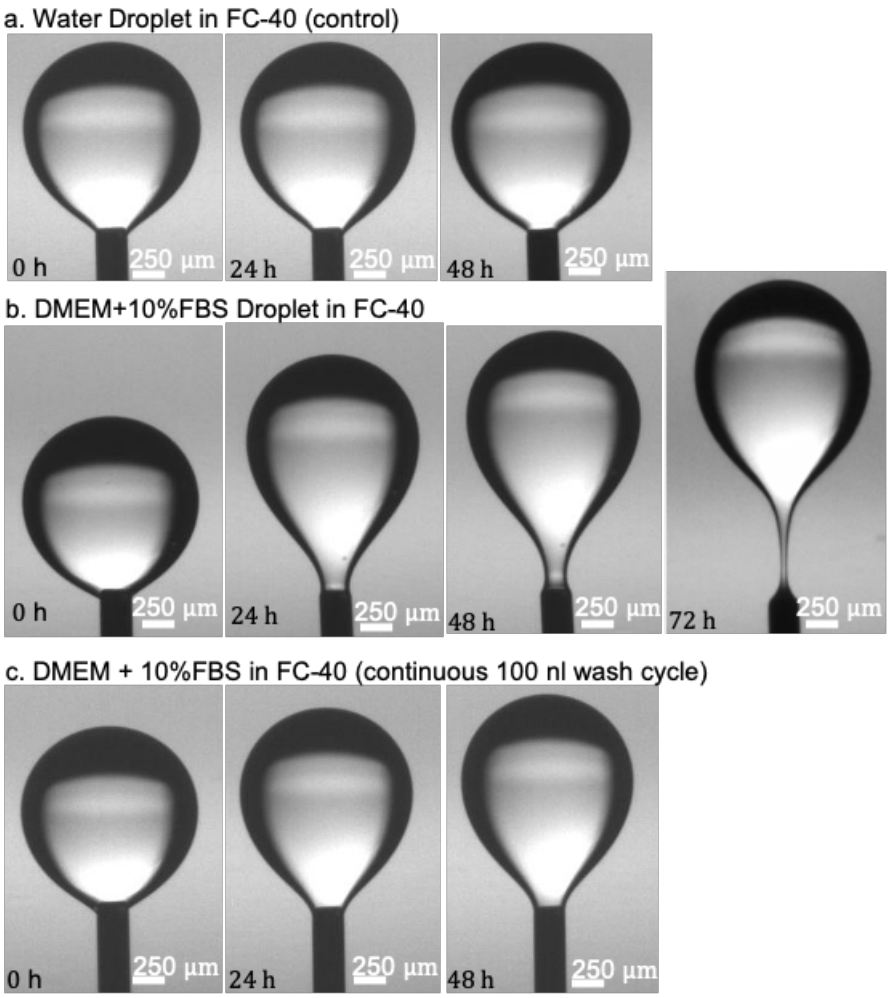

Figure 17. Effects of serum detected by Pendant Drop Tensiometry. **a.** Control: sterile-filtered water droplet (1.4 µL) in FC-40 bulk. $\boldsymbol{\gamma} = 52.06 \pm 0.66$ mN/m as expected from literature [57] and remains unchanged over 48 h. **b.** DMEM + 10% FBS droplet (1.4 µL) in FC-40 bulk. Drop shape changes over time and displays semi-elastic interfacial properties as the droplet "necks" due to buoyancy. **c.** Same as (**b**), but 100 nL DMEM + 10% FBS was constantly withdrawn/infused every 30 min over 48 h. This flow slows the change in drop shape.

It is more useful to investigate an elastic capsule's *effective* interfacial tension ($\boldsymbol{\gamma_{eff}}$) [61], [62] using the "drop volume" technique to incorporate the membrane's elastic stresses. Immediately before drop departure, the droplet's total tensile stress ($\boldsymbol{\gamma_{eff}}$) can be calculated from the force balance in Equation 12. Averaged from five distinct DMEM + 10% FBS drops which remained attached to the needle for at least 48 hours, $\boldsymbol{\gamma_{eff}} = 63.8 \pm 19.1$ mN/m. Although $\boldsymbol{\gamma_{eff}} > \boldsymbol{\gamma_{PDT}}$ as expected since pendant drop tensiometry fails to include the membrane's elastic stresses,

the standard deviation of a drop's effective interfacial tension is too large to conclusively determine the system's $\boldsymbol{\gamma_{eff}}$. Moreover, drops departed at unpredictable times and with inconsistent necking radii ($\mathbf{R_{neck}}$).

Cycling 100 nL out of, and back into, a suspended 1.4 µL DMEM + 10% FBS drop continuously (30 min withdrawal, 30 min infusion) slows the necking significantly (Figure 17c). Such cycling is consistent with the washing away of proteins aggregated at the media-fluorocarbon interface [63], but more research is required to characterize this extraordinary interface.

6.4 Conduit Height Measurements

Unlike conduits in traditional solid-walled circuits, those constructed via SIM-printing have cross sections that vary depending on flow (see Chapter 4.3). The simplified analytical solution (Equation 45) indicates that a simple way to alter a conduit's height profile is to vary the volumetric flow rate **Q** pumped into the conduit via an external syringe pump; increasing flow rate increases local Laplace pressures (and thus centre heights according to Equation 7) along a conduit's length (Figure 18a). Similarly, conduit height profiles can be altered by varying conduit footprint geometry (specifically the conduit's half width **a**); increasing a conduit's half width increases conduit heights (Figure 18b).

The theoretical curves over-laying experimental data in Figure 18a-b are developed using the simplified analytical solution defined in Equation 45. All but one variable necessary for predicting a conduit's height profile is known experimentally: volumetric flow rate (**Q**) is user-set via the external syringe pump, dynamic viscosity (**µ**) is a known fluid property before experimentation, and conduit half-width (**a**) is determined by the SIM-operator and verified via microscopy. Interfacial tension (**γ**) between DMEM + 10% FBS and FC-40, however, is difficult

to determine by traditional methods (i.e., Pendant Drop Tensiometry) due to the formation of a semi-elastic membrane at the liquid-liquid interface. Thus, theory curves are fitted to experimental data by varying $\boldsymbol{\gamma_{eff}}$; the best fit to data from all flow rates and conduit half-widths considered was given by $\boldsymbol{\gamma_{eff}} = 22$ mN/m (Figure 18a-b). Error propagation using the root sum of the squares (RSS) method ensures the fitted $\boldsymbol{\gamma_{eff}}$ falls within an acceptable margin of error (see Figure 25 in Appendix 1).

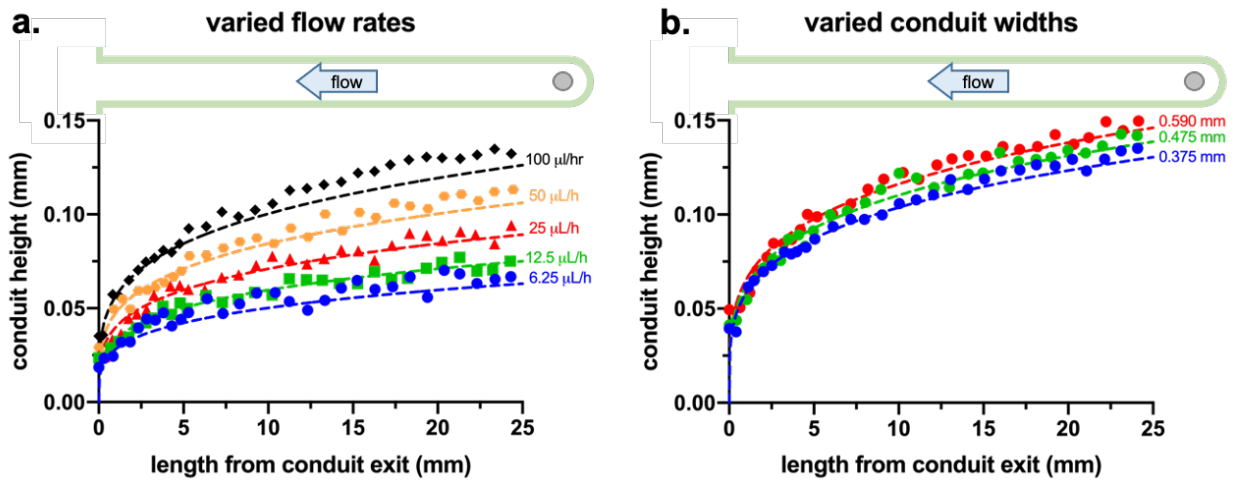

Figure 18. The effect of flow on the centre height, $\mathbf{h_0}$, along the length of an open-ended conduit with flexible walls. 30 mm long conduits were SIM-printed using DMEM + 10% FBS in 6 cm Petri dishes. Infusing needles were inserted at the closed end of the conduit and DMEM + 10% FBS with fluorescent 0.5 µm diameter beads solution was actively pumped via an external syringe pump. Top: schematic of conduit. Bottom: in plots, symbols represent measured heights while dotted curves represent analytical predictions (Equation 45) while $\boldsymbol{\gamma_{eff}} = 22$ mN/m. **a.** The effect of volumetric flow rate ($\mathbf{Q}$) on conduit heights ($\mathbf{a}$ = 0.325 mm). Conduit heights increase with increased volumetric flow rate. **b.** The effect of conduit half width ($\mathbf{a}$) on conduit heights ($\mathbf{Q}$ = 100 µL/h). Conduit heights increase with decreased half width.

Conduit flows remain stable over times long enough for cell culture (e.g., flowing over 24 h does not alter conduit-height profiles). Similarly, if a conduit is left static for 24 h before media is actively pumped through it, the conduit-height profile is nearly identical to that obtained if pumping begins immediately after fabrication (see Figure 31a in Appendix 2). With no temporal effect on flows, cell biologists are able to culture cells for days in static or dynamic

environments with no substantial change to flow physics. For example, HUVECs were cultured in conduits as a proof of concept for biocompatibility in dynamic environments.

Additionally, biologists are able to flow different aqueous solutions through circuits originally built using DMEM + 10% FBS (or DMEM + 20% SR) while maintaining a conduit's no-slip boundary condition, as the flexible membrane is not washed away. For instance, distilled water can be flowed through a conduit built using DMEM + 10% FBS with no change in conduit heights/flows (see Figure 31b in Appendix 2). Therefore, Biologists can apply any aqueous solution to these systems to fit their specific research needs without sacrificing the accuracy of flow predictions.

6.4.1 Choked Conduits

Characterizing wall shear stresses in SIM-printed conduits is important to cell biologists [64]–[66] since shear stresses profoundly influence the physiology of cells attached to Petri dishes [66]. Although shear will always vary across a conduit's width due to its rounded cross-sectional geometry, chokes create regions of constant centre heights (and thus uniform shear profiles) along a circuit's length (Figure 19a-b). Introducing a choke has two major effects; $\mathbf{h_{0,conduit}}$ increases upstream of the choke proportional to $\frac{\mathbf{a_{conduit}^2}}{\mathbf{a_{choke}^2}}$ (see Equation 62), and the primary conduit's heights remain almost constant since pressure drop in the primary conduit is minimal. Increasing flow rate increases primary conduit heights by a characteristic amount (Figure 19a). Similarly, the longer the choke, the higher the primary conduit's centre height (Figure 19b).

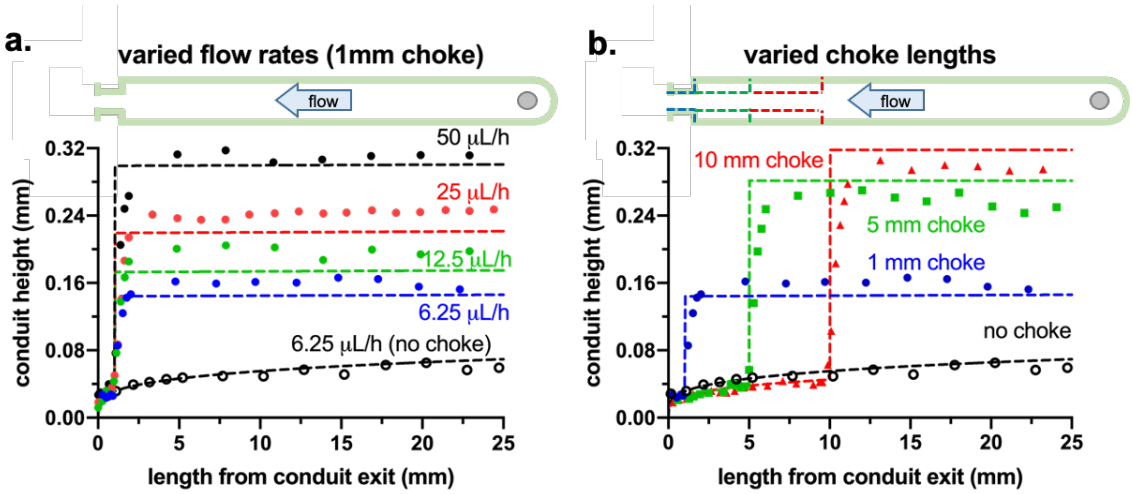

Figure 19. Choking conduits to create regions of constant cross-sectional geometry. 30 mm long primary conduits attached to smaller "choke" conduits were SIM-printed using DMEM + 10% FBS in 6 cm Petri dishes. Infusing needles were inserted at the closed end of the primary conduit and DMEM + 10% FBS with fluorescent 0.5 μm diameter beads solution was actively pumped via an external syringe pump. Top: schematic of conduit. Bottom: in plots, symbols represent measured heights while dotted curves represent analytical predictions (Equation 45) while $\boldsymbol{\gamma_{eff}} = 22$ mN/m. **a.** A 1 mm long choke of half width $\mathbf{a_{choke}} = 0.2$ mm is attached at the exit of a primary conduit of half width $\mathbf{a_{conduit}} = 0.5$ mm actively pumped with flow rates of 6.25, 12.5, 25, and 50 μL/h. A conduit's height profile with identical footprint geometry, without the addition of a choke, is included for comparison. **b.** Choked conduit profiles with 1, 5, and 10 mm long chokes where $\mathbf{a_{choke}} = 0.2$ mm and $\mathbf{a_{conduit}} = 0.5$ mm ($\mathbf{Q} = 6.25$ μL/h).

6.5 Bifurcating Conduits

The flow theory derived in this thesis can be applied to more complex circuit formations such as bifurcating conduit networks (see Figure 20). Conduit heights in bifurcating circuits still decrease in the direction of flow following the analytical solution in Equation 45. However, differences in flow rates experience by parent/daughter conduits must be considered. Due to continuity, each daughter conduit in Figure 20a experiences 12.5 μL/h whereas the daughter conduit in Figure 20b experiences 50 μL/h since each needle is infusing with a flow rate of 25 μL/h. Since pressure drop within the junction is small compared to pressure drop down a conduit, the total pressure drop within each junction is assumed to be zero. Flows through more complex tree bifurcations with several "generations" of branches can also be accurately predicted (Figure 20c).

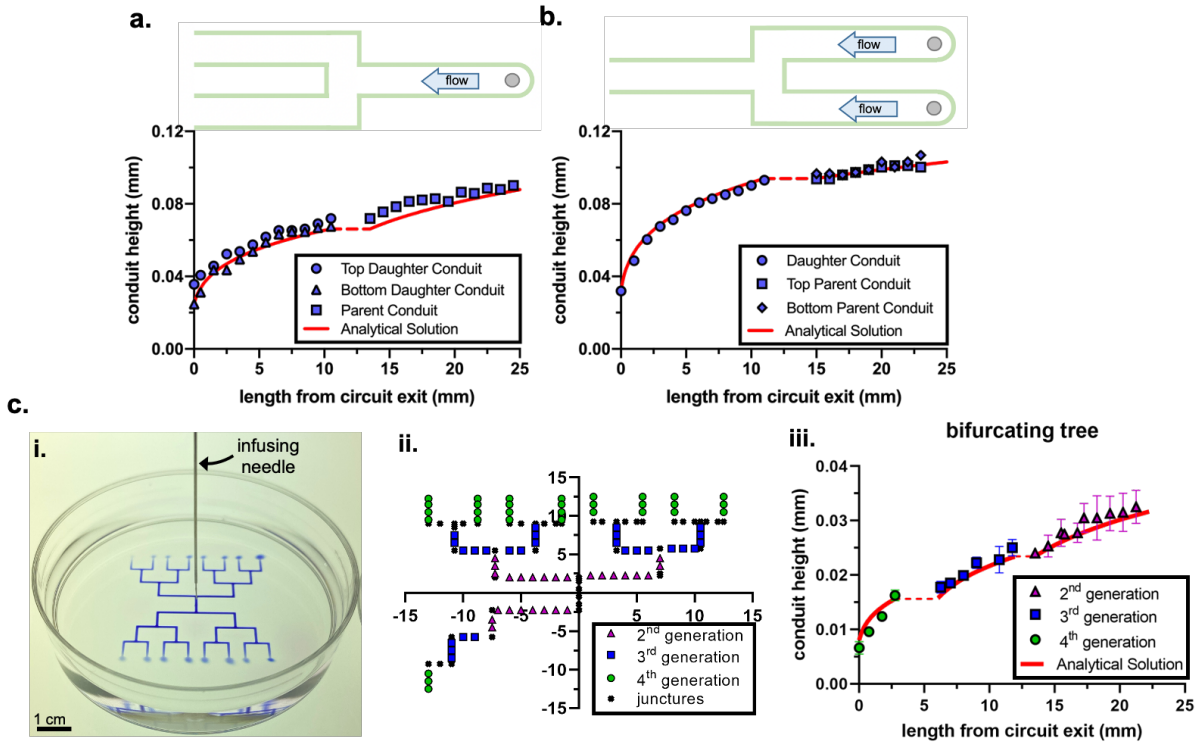

Figure 20. Centre-height profiles of bifurcating conduits. 30 mm long circuits (12.5 mm daughter conduits and 17.5 mm parent conduits) were SIM-printed using DMEM + 10% FBS in 6 cm Petri dishes; all conduits have half widths of 0.5 mm. Infusing needle(s) were inserted at the closed end of the conduit and DMEM + 10% FBS with fluorescent 0.5 µm diameter beads solution was actively pumped via an external syringe pump. All needles depicted above are pumping at 25 µL/h. In plots, symbols represent measured heights while dotted curves represent analytical predictions made using $\boldsymbol{\gamma_{eff}} = 22$ mN/m. Pressure drop in the bifurcating junction is small compared to pressure drop due to flow in conduits and is thus assumed to be zero (dotted analytical curve). **a.** Single parent conduit bifurcating into two daughter conduits ($\mathbf{a} = 0.5$ mm). **b.** Two parent conduits converging into a single daughter conduit ($\mathbf{a} = 0.5$ mm). **c.** Bifurcating tree with single infusion point and 16 exit locations (all branches have half width $\mathbf{a} = 0.2$ mm). **i.** Image of media (dyed blue) reaching exits of tree. **ii.** Plot showing locations where conduit heights were measured. **iii.** Plot of tree heights from exit(s) to infusion point. Heights on analogous branch generations were averaged and error bars were applied to denote standard deviation between equidistant points from circuit exits.

8 Conclusion

Submerged impinging microjet (SIM) printing provides a versatile, accessible, and biocompatible alternative to fabricating open-microfluidic devices. SIM-printing's ability to quickly transform a typical Petri dish containing culture media into an intricate microfluidic device with virtually any two-dimensional geometry makes SIM-printing attractive to cell biologists. Controlling the microjet's traversing speed, volumetric flow rate, and height above the impinged substrate allows users to vary the width of SIM-printed FC-40 walls, whilst giving insight into the technique's limitations. Unique flow patterns in wetting films during printing highlight differences between media solutions with and without serum (or serum replacement); serum prevents shear-induced flow within the aqueous phase due to the formation of an "elastic membrane" at the media-fluorocarbon interface. This membrane simplifies the derivation of an analytical solution to accurately predict flows by applying a no-slip boundary condition at the media-fluorocarbon interface. Our analytical solution enables us to predict conduit heights, streamline flow velocities, local Laplace pressures, and shear stresses in SIM-printed circuits. Effective interfacial tension was determined by fitting experimental data to analytically-generated conduit heights; $\boldsymbol{\gamma_{eff}} = 22$ mN/m fit experimental results within acceptable error margins. Examples of more complex microfluidic circuitry such as chokes and bifurcations also adhere to our flow theory and highlight its breadth; our solution applies to any circuit design so long as the circuit abides by the geometrical restrictions outlined here. The theoretical work that should continue includes experimentally validating conduit failure ($\mathbf{a = h_0}$), passive flowing systems, and further investigation of the membrane which forms between media and FC-40.

Appendix 1: Supplemental Theory

Reynolds Number Calculations

Jet Flow

Recalling Equation 4 from chapter 4.1.1, a circular jet's Reynolds number is

$$\mathbf{Re} = \frac{\boldsymbol{\rho} \mathbf{d_i} \mathbf{u_{avg}}}{\boldsymbol{\mu}} \tag{63}$$

where $\boldsymbol{\rho}$ is the fluid density, $\mathbf{u_{avg}}$ is the average fluid velocity, $\mathbf{d_i}$ is the characteristic length of the flow system (which for circular jets is simply the inner diameter of the jet), and $\boldsymbol{\mu}$ is the fluid's dynamic viscosity. Also recall from Equation 3 the entry length ($\boldsymbol{l_e}$) required for laminar pipe flow to become fully developed:

$$\frac{\boldsymbol{l_e}}{\mathbf{d_i}} = \mathbf{0.06Re} \tag{64}$$

The following jet Reynolds numbers and entry lengths are calculated for a 34g ($\mathbf{d_i} = 70$ µm) needle. Standard flow rates for jet printing with this needle is 10 µL/s, although as low as 5 µL/s and as high as 20 µL/s have been used to successfully print (see Figure 15a in Chapter 6.1 for more details).

Table 1: Reynolds Numbers for Submerged Impinging Microjet

Flow Rate [uL/s]	u_{avg} [m/s]	Re [unitless]	l_e [mm]
5	1.299	41	0.174
10	2.598	83	0.347
20	5.197	165	0.694

Conduit Flow

For flow through the flexible-walled conduits discussed in this study,

$$\mathbf{Re} = \frac{\boldsymbol{\rho d_h u_{avg}}}{\boldsymbol{\mu}} \tag{65}$$

where $\mathbf{d_h}$ is the conduit's hydraulic diameter. The hydraulic diameter is often used as the characteristic length for flow through non-circular ducts or pipes in lieu of a traditional circular pipe's diameter in Reynolds number calculations. A duct's hydraulic diameter is defined as:

$$\mathbf{d_h} = \frac{\mathbf{4A}}{\mathbf{p}} \tag{66}$$

where **A** is the duct's cross sectional area and **p** is the duct's wetted perimeter. In the case of the fluidic microconduits in this study (see Figure 6c in chapter 4.3.1 for conduit geometry nomenclature), the hydraulic diameter is

$$\mathbf{d_h} = \frac{\mathbf{2}\left(\mathbf{R^2}\,\mathbf{sin^{-1}}\left(\frac{\mathbf{a}}{\mathbf{R}}\right) - \mathbf{ab}\right)}{\mathbf{R}\,\mathbf{sin^{-1}}\left(\frac{\mathbf{a}}{\mathbf{R}}\right) + \mathbf{a}} \tag{67}$$

The following Reynolds Numbers are calculated from the experimental data in Figure 18a.

Table 2: Reynolds Numbers for SIM-Printed Conduits

Flow Rate [uL/h]	Distance from Conduit Exit [mm]	A [mm^2]	d_h [µm]	u_{avg} [mm/s]	Re [unitless]
6.25	0	0.00624	18.274	0.27805	0.00542
	25	0.02189	65.732	0.07933	0.00556
12.5	0	0.00789	23.096	0.43986	0.01083
	25	0.02355	71.475	0.14746	0.01124
25	0	0.00833	24.356	0.83412	0.02166
	25	0.03051	91.010	0.22763	0.02209
50	0	0.00979	28.619	1.41922	0.04330
	25	0.03824	113.209	0.36318	0.04384
100	0	0.01179	34.463	2.35575	0.08656
	25	0.04524	132.832	0.61404	0.08700

Conduit Capillary Length

The liquid conduits in this thesis are assumed to be dominated by interfacial forces and unaffected by gravity. To justify this assumption, recall the Bond number which representants the ratio of gravitational to interfacial forces acting on a fluid volume (Equation 8). The capillary length $\mathbf{L_c}$ of the conduits in this study (i.e., the characteristic length **L** at which gravitational and interfacial forces are equal), is 3.0 mm. To neglect gravity completely, a conduit's characteristic length should be much less than its capillary length; $\mathbf{L \ll L_c}$.

The characteristic length used for pendant drops (i.e., the drop's radius of curvature at its apex) cannot be used for conduit analysis; instead, a new characteristic length must be determined by investigating the Bond number. Written as the ratio of hydrostatic to Laplace pressures:

$$\mathbf{Bo = \frac{\Delta \rho g h_0}{\frac{\gamma}{R}}} \tag{68}$$

where $\mathbf{h_0}$ is the conduit's centre height and **R** is the conduit's cross-sectional radius of curvature. For the conduit's in this study, $\mathbf{h_0 \ll a}$ so the simplified radius of curvature $\mathbf{R = \frac{a^2}{2h_0}}$ can be substituted above.

$$\mathbf{Bo = \frac{\Delta \rho g a^2}{\gamma}} \tag{69}$$

When Equation 69 above is compared to the original definition of Bond number in Equation 8, the conduit's characteristic length is obvious; $\mathbf{L = a}$. The largest conduit half width in this study (0.5 mm, see Figure 18b) corresponds to a characteristic length of 0.35 mm, six times smaller than the conduit's capillary length.

Perfect-Slip at Media-Fluorocarbon Interface

The analytical solution outlined in Chapter 4.3.1 assumes the media-fluorocarbon interfaces of SIM-printed conduits, albeit flexible in nature, are solid. Thus, a no-slip boundary condition was applied to this interface throughout the solution's derivation. In the context of liquid-liquid interfaces, this is analogous to assuming the ratio of the immiscible fluid's viscosity ($\boldsymbol{\mu_{imm.\ fluid}}$) to the media's viscosity ($\boldsymbol{\mu_{media}}$) is infinite; $\boldsymbol{\lim_{\mu_{imm.\ fluid}\to\infty}\left(\frac{\mu_{imm.\ fluid}}{\mu_{media}}\right)=\infty}$. To predict flows for two-phase systems with any possible ratio of dynamic viscosities, the other extreme must be considered: perfect-slip. In this case, $\boldsymbol{\lim_{\mu_{imm.\ fluid}\to 0}\left(\frac{\mu_{imm.\ fluid}}{\mu_{media}}\right)=0}$.

Perfect-Slip Analytical Solution

The following section mirrors Chapters 4.3.1 (and associated Equations 20-43); the only difference is the boundary condition applied to the media-fluorocarbon interface.

In the case of perfect-slip, the same governing equation derived the Navier-Stokes equations should be applied: $\boldsymbol{\frac{\partial P}{\partial x}=\mu\frac{\partial^2 u}{\partial y^2}}$. Solving for a conduit's fully developed unidirectional velocity profile $\mathbf{u}(y)$ can be accomplished by integrating the governing equation twice and applying the two following boundary conditions:

3. $\boldsymbol{u\left(-\frac{h_0}{2}\right)=0}$
4. $\boldsymbol{\frac{du}{dy}\left(\frac{h_0}{2}\right)=0}$

$\mathbf{u}(y)$ can then be expressed as follows:

$$\mathbf{u(y)=\frac{1}{2\mu}\frac{dP}{dx}\left(y^2-h_0y-\frac{3}{4}h_0^2\right)} \qquad \textbf{(70)}$$

In terms of the flow's maximum velocity $\boldsymbol{u_{max}=-\frac{h_0^2}{2\mu}\frac{dP}{dx}}$, the fluid velocity profile, gradient, and second derivative are defined as follows:

$$\mathbf{u(y) = u_{max}\left(\frac{3}{4} + \frac{y}{h_0} - \frac{y^2}{h_0^2}\right)} \tag{71}$$

$$\mathbf{\frac{du}{dy} = \frac{u_{max}}{h_0} - \frac{2u_{max}}{h_0^2}\, y} \tag{72}$$

$$\mathbf{\frac{d^2u}{dy^2} = -\frac{2u_{max}}{h_0^2}} \tag{73}$$

Since $\mathbf{\frac{\partial P}{\partial x} = \mu\, \frac{\partial^2 u}{\partial y^2}}$ it follows that:

$$\mathbf{\frac{dP}{dx} = -\mu \frac{2u_{max}}{h_0^2}} \tag{74}$$

$$\mathbf{\frac{dP}{dx} \propto \frac{u_{max}}{h_0^2}} \tag{75}$$

In the *z*-direction (across a conduit's width), $\mathbf{\frac{dP}{dx} = C}$ where $\mathbf{C}$ is some constant since the flow is assumed to be perfectly laminar (i.e., there is no pressure gradient, and thus no flow, in the *z*-direction). The following relationships can then be concluded to relate maximum flow velocities across a conduit's width and a conduit's maximum centre velocity:

$$\mathbf{\frac{u_{max(0)}}{h_0^2} = \frac{u_{max(z)}}{h_z^2}} \tag{76}$$

$$\mathbf{u_{max\,(z)} = \frac{u_{max\,(0)}}{h_0^2} h_z^2} \tag{77}$$

Volumetric flow rate can also be written in an integral form incorporating the flow's velocity profile defined in Equation 71.

$$\mathbf{Q = \int_{-a}^{+a} \int_{-\frac{h_z}{2}}^{\frac{h_z}{2}} u(y)\ dydz} \tag{78}$$

$$\mathbf{Q} = \int_{-a}^{+a} \frac{2}{3}\mathbf{u_{max}}\mathbf{h_z}\,\mathbf{dz} \tag{79}$$

Substituting the relationship for $\mathbf{u_{max(z)}}$ from Equation 77:

$$\mathbf{Q} = \frac{2}{3}\frac{\mathbf{u_{max(0)}}}{\mathbf{h_0^2}}\int_{-a}^{+a}(\mathbf{h_z})^3\,\mathbf{dz} \tag{80}$$

Extracting constants from the integrand, utilizing the conduits symmetry about its centre line, and substituting Equation 19 for $\mathbf{h_z}$ leaves the following relationship for volumetric flow rate:

$$\mathbf{Q} = \frac{4}{3}\frac{\mathbf{u_{max}}}{\mathbf{h_0^2}}\int_{0}^{a}\left(\sqrt{\mathbf{R^2 - z^2}} - \mathbf{b}\right)^3\,\mathbf{dz} \tag{81}$$

As written in Equation 81, evaluating the integrand in order to solve for $\mathbf{h_0}$ can only be done so numerically in an iterative solution. Instead, the integrand can be normalized such that $\boldsymbol{\eta} = \frac{\mathbf{z}}{\mathbf{a}}$ and averaged over half-width to centre-height ratios which satisfy $\mathbf{a} \gg \mathbf{h_0}$:

$$\mathbf{Q} = \frac{4}{3}\,\mathbf{h_0}\mathbf{u_{max}}\mathbf{a}\int_{0}^{1}\frac{\left(\sqrt{\mathbf{R^2 - \eta^2 a^2}} - \mathbf{b}\right)^3}{\mathbf{h_0^3}}\mathbf{d\eta} \tag{82}$$

Using same method as before (see Figure 8), the average value of the normalized integrand above is calculated (0.4588) resulting in the following:

$$\mathbf{Q} = \frac{4}{3}\,\mathbf{h_0}\mathbf{u_{max}}\mathbf{a}(\mathbf{0.4588}) \tag{83}$$

$$\mathbf{u_{max}} = \frac{\mathbf{Q}}{\mathbf{0.6118 h_0 a}} \tag{84}$$

Substituting the relationship for $\mathbf{u_{max}}$ derived from Poiseuille flow between two infinite parallel plates into Equation 84 produces:

$$\left(\frac{\mathbf{3.269Q\mu}}{\mathbf{a}}\right)\mathbf{dx} = \left(\mathbf{h_0^3}\right)\mathbf{dP} \tag{85}$$

The local pressure at any *x*-location along the length of a conduit can be characterized by the local Laplace pressure in accordance with the simplified Young-Laplace Equation for fluid volumes whose geometry represents the cap of long cylinders (see Equation 7). Utilizing the simplified cross-sectional radii of curvature produces the following equation defining local conduit pressure:

$$\mathbf{P} = \boldsymbol{\gamma}\left(\frac{\mathbf{1}}{\mathbf{R}}\right) \approx \boldsymbol{\gamma}\left(\frac{\mathbf{2h_0}}{\mathbf{a^2}}\right) \tag{86}$$

This remains true so long as the change is static pressure along the conduit's length is small relative to the change in Laplace pressure. Local pressures from Equation 86 can then be solved in terms of local centre-heights $\mathbf{h_0}$, and then substituted into Equation 85 to allow for integration:

$$\left(\frac{\mathbf{3.269Q\mu}}{\mathbf{a}}\right)\mathbf{dx} = \left(\frac{\mathbf{a^6}}{\mathbf{8\gamma^3}}\mathbf{P^3}\right)\mathbf{dP} \tag{87}$$

Integrating produces the following solution:

$$\frac{\mathbf{3.269Q\mu x}}{\mathbf{a}} + \mathbf{C_1} = \frac{\mathbf{a^6}}{\mathbf{32\gamma^3}}\mathbf{P^4} \tag{88}$$

Reintroducing $\mathbf{P} \approx \boldsymbol{\gamma}\left(\frac{\mathbf{2h_0}}{\mathbf{a^2}}\right)$ back into the equation above and solving for $\mathbf{h_0}$:

$$\frac{\mathbf{6.583Q\mu ax}}{\boldsymbol{\gamma}} + \mathbf{C_1} = \mathbf{h_{0,x}^4} \tag{89}$$

Since at the conduit's exit ($x = 0$), $\mathbf{h} = \mathbf{h_{0,x=0}}$ and $\mathbf{C_1} = \mathbf{h^4_{0,x=0}}$. Thus, the following equation predicting conduit centre-heights is produced.

$$\mathbf{h_{0,x}} = \left(\frac{\mathbf{6.562Q\mu ax}}{\boldsymbol{\gamma}} + \mathbf{h^4_{0,x=0}}\right)^{0.25} \tag{90}$$

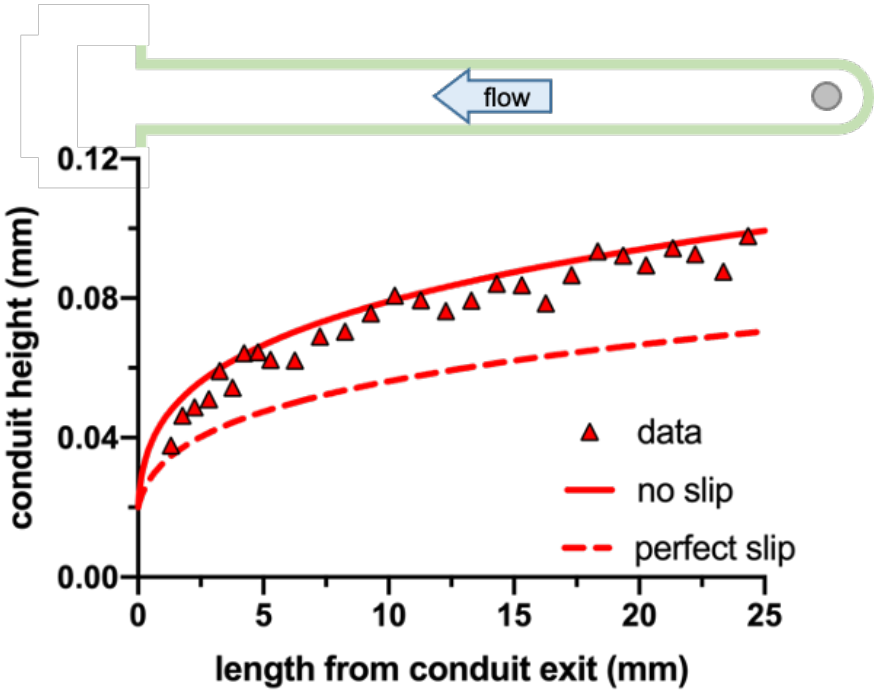

Figure 21. Comparing analytically-derived conduit height predictions assuming no-slip (bold curve) and perfect-slip (dotted curve) boundary conditions at a conduit's media-fluorocarbon interface to experimental results (30 mm long SIM-printed conduit using DMEM + 10% FBS; $\mathbf{Q} = 25$ uL/h, $\mathbf{a} = 0.325$ mm, $\boldsymbol{\gamma}_{\mathbf{eff}} = 22$ mN/m). When conduits are built using serum, there is excellent agreement between experimental data and predicted results when assuming no-slip.

Conduit Failure Criterion

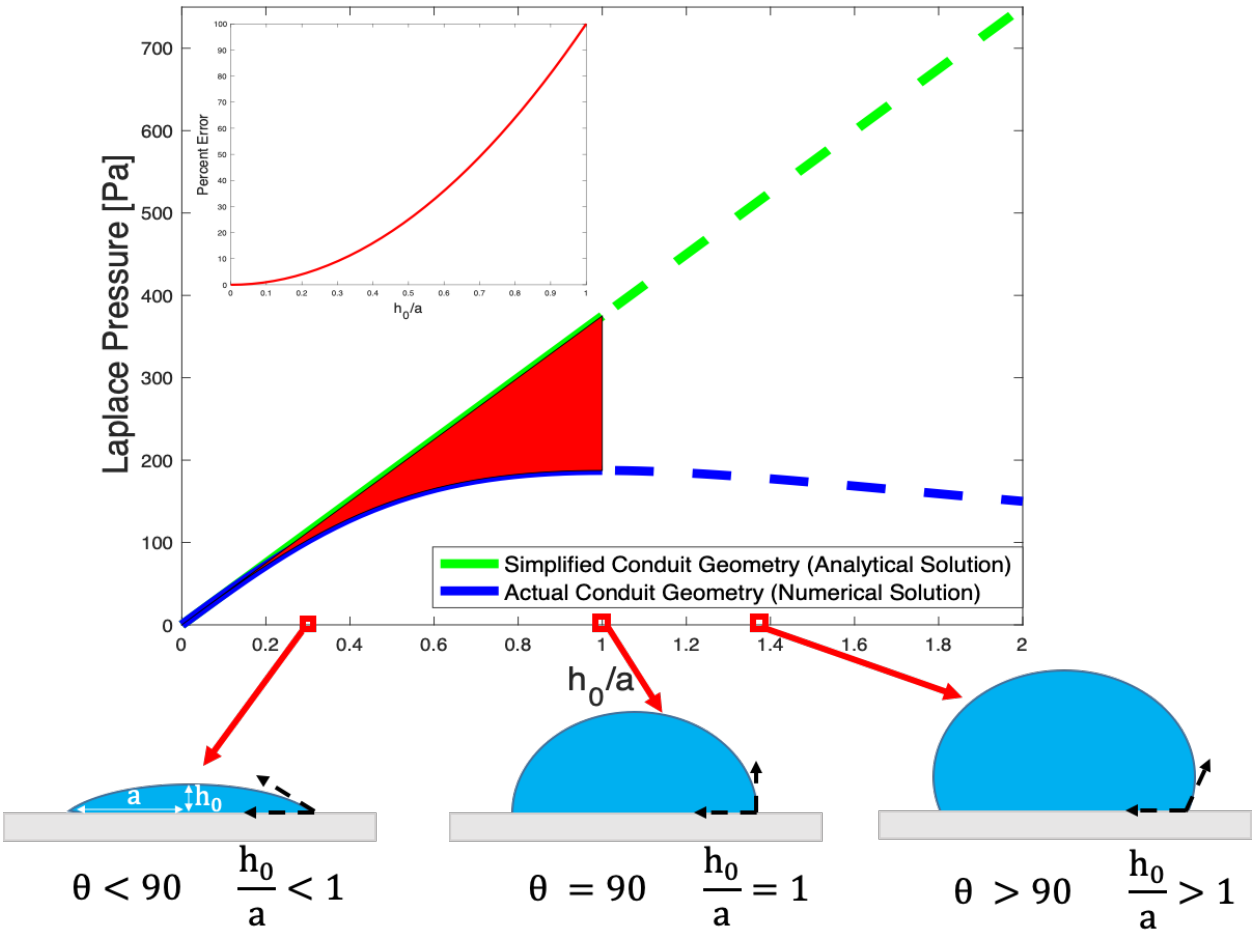

Figure 22. Comparing conduit Laplace pressures from the derived analytical (Equation 42) and numerical (Equation 48-58) solutions over a range of centre height to half width $\left(\frac{\mathbf{h_0}}{\mathbf{a}}\right)$ ratios. Agreement between the analytical and numerical solutions is found only at low $\frac{\mathbf{h_0}}{\mathbf{a}}$ ratios in agreement with simplifications made during the analytical derivation; when $\frac{\mathbf{h_0}}{\mathbf{a}} \leq 0.2$, the percent error between solutions is $\leq \mathbf{4\%}$. Flow through conduits with low contact angles (when $\mathbf{a} \gg \mathbf{h_o}$) can be estimated as Poiseuille flow between two infinite parallel plates. As $\frac{\mathbf{h_0}}{\mathbf{a}}$ increases, however, the numerical solution (which doesn't make geometrical simplifications) begins to deviate from the analytical solution which is formulated assuming the conduit half width is always much greater than the conduit centre height. As expected in accordance with the Young Laplace Equation (see Equation 7), a conduits maximum Laplace pressure is experienced when $\frac{\mathbf{h_0}}{\mathbf{a}} = \mathbf{1}$ according to the numerical solution.

A conduit can only withstand a certain volumetric flow rate ($\mathbf{Q_{max}}$) before reaching capillary instability [67] and rupturing. Capillary instability occurs when the conduit's contact

angle $\boldsymbol{\theta}$ (defined as $\boldsymbol{\sin^{-1}\left(\frac{2ah_0}{a^2+h_0^2}\right)}$ according to the cross-sectional geometry in Figure 6c) reaches 90°. In other words, instability occurs when the conduit's half width equals the conduit's maximum height ($\boldsymbol{a = h_{0,x}}$) producing a perfect half-circle cross section when gravity is negligible (refer to when $\boldsymbol{\frac{h_0}{a} = 1}$ in Figure 22 above).

Flow through a conduit relies on a negative pressure gradient in the direction of flow. Since the maximum pressure a flexible-walled conduit can withstand occurs when a local cross-section achieves $\boldsymbol{\theta} = 90°$, flow further upstream begins to pool creating a bulging conduit where $\boldsymbol{\theta} > 90°$; this phenomenon soon leads to pinning line failure. Using the simplified analytical solution derived in Equation 45, the following equations can be deduced when applying the instability criterion $\boldsymbol{a = h_{0,x}}$:

$$\boldsymbol{a = \left(\frac{26.154 Q_{max} \mu a x}{\gamma}\right)^{0.25}} \tag{91}$$

$$\boldsymbol{Q_{max} \geq \frac{\gamma a^3}{26.154 \mu L}} \tag{92}$$

Recall, however, the analytical solution relies on the assumption that $\boldsymbol{a \gg h_0}$ so conduits can be modeled as parallel plates. The largest half width to height ratio considered during the analytical derivation (see Figure 8) is only 0.2 which is far before capillary instability occurs ($\boldsymbol{\theta} = 90°$) occurs. Additionally, the analytical solution provides an unrealistic expectation for conduit pressure versus $\boldsymbol{\frac{h_0}{a}}$ (see green line in Figure 22); due to geometrical simplifications made in Equation 37, pressure increases proportionally with conduit height:

$$\boldsymbol{R \approx \frac{a^2}{2h_0} \rightarrow P = \frac{2\gamma h_0}{a^2} \rightarrow P \propto h_0} \tag{93a-c}$$

Conversely, the numerical solution (see blue curve in Figure 22) makes no geometrical simplifications and thus provides a more accurate estimate of conduit failure at larger contact angles:

$$\mathbf{R = \frac{a^2 + h_0^2}{2h_0} \;\rightarrow\; P = \frac{2\gamma h_0}{a^2 + h_0^2} \;\rightarrow\; P \propto \frac{h_0}{1 + \left(\frac{h_0}{a}\right)^2}} \qquad \textbf{(94a-c)}$$

This, of course, does not mean the analytical solution is inadequate in prediction flows through flexible-walled conduits; it merely highlights conduit $\frac{\mathbf{h_o}}{\mathbf{a}}$ ratios where the analytical solution can be reliably utilized. For $\frac{\mathbf{h_o}}{\mathbf{a}} \leq 0.2$ for instance, the percent error between the numerical and analytical solution is $\leq 4\%$.

Numerical Solution Conduit Height Predictions

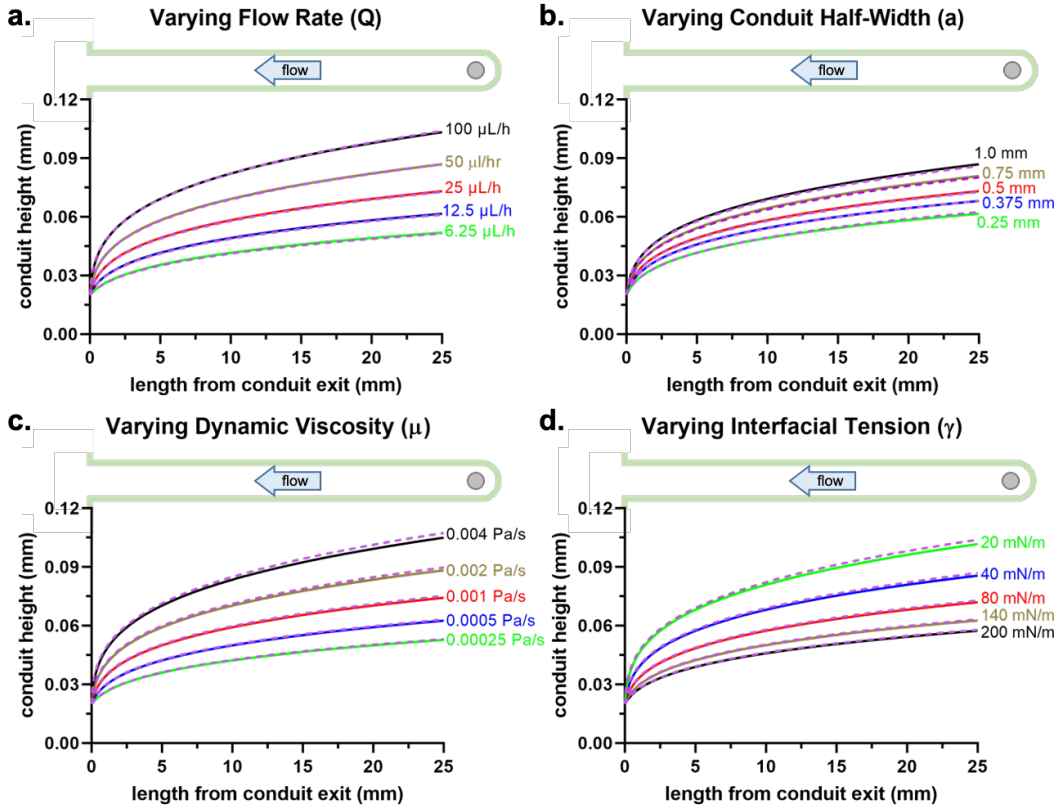

Figure 23. Numerical (dotted) vs. Analytical (bold) predictions of fluid-walled conduit height profiles while experiencing steady state active flow. Varying volumetric flow rate (top left), conduit half width (top right), or liquid characteristics such as dynamic viscosity (bottom left) and interfacial tension (bottom right) change predicted conduit height profiles. While one of the four variables is being changed above, all other variables are held constant at the following reference values ($\mathbf{Q_{ref}} = 25$ µL/h, $\mathbf{a_{ref}} = 0.5$ mm, $\boldsymbol{\mu_{ref}} = 0.001$ Pa·s, and $\boldsymbol{\gamma_{ref}} = 80$ mN/m). When $\mathbf{a} \gg \mathbf{h_{0,x}}$ there is strong agreement between the numerical and analytical solutions.

Agreement between numerical and analytical solutions is strong for conduit centre to half width heights investigated in Figure 23 above. While theoretical projections from the analytical solution can be collapsed onto a reference curve $\mathbf{h_{0,x\,(ref)}}$ by raising $\mathbf{Q}$, $\mathbf{a}$, and $\boldsymbol{\mu}$ to the 0.25 power and $\boldsymbol{\gamma}$ to the -0.25 power (see Equation 42), the numerical solution collapses using the following relationship:

$$\frac{\mathbf{h_{0,x}}}{\mathbf{h_{0,x\,(ref)}}} = \left(\frac{\mathbf{Q}}{\mathbf{Q_{(ref)}}}\right)^{0.2503} \left(\frac{\mathbf{a}}{\mathbf{a_{(ref)}}}\right)^{0.2355} \left(\frac{\boldsymbol{\mu}}{\boldsymbol{\mu_{(ref)}}}\right)^{0.251} \left(\frac{\boldsymbol{\gamma}}{\boldsymbol{\gamma_{(ref)}}}\right)^{-0.252} \quad \textbf{(95)}$$

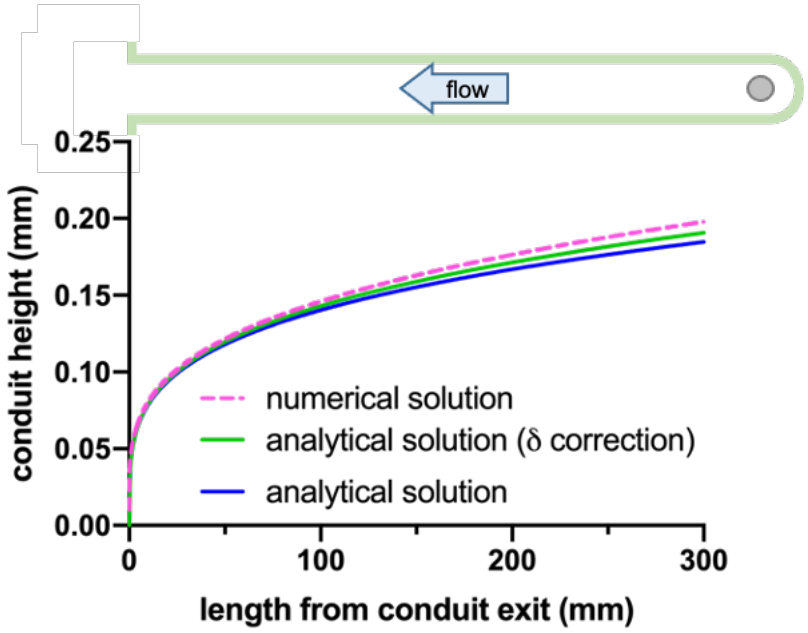

Figure 24. Comparing analytical and numerical predictions for long conduits which no longer abide by $\mathbf{a} \gg \mathbf{h_0}$. Using the $\boldsymbol{\delta}$ corrected analytical solution from Equation 46 decreases the percent error from the numerical predictions from 7.8% to 4.3% at $\frac{\mathbf{h_0}}{\mathbf{a}} = 0.4$ ($\mathbf{Q} = 25$ µL/h, $\mathbf{a} =$ 0.5 mm, $\boldsymbol{\mu} = 0.001$ Pa·s, and $\boldsymbol{\gamma} = 22$ mN/m).

Conduit Height Error Propagation

Recalling the simplified analytical solution for predicting flexible-walled conduit centre heights from Equation 45:

$$\mathbf{h_{0,x}} = \left(\frac{26.154\mathbf{Q\mu ax}}{\boldsymbol{\gamma}}\right)^{\frac{1}{4}} \tag{96}$$

In order to determine if measured conduit heights agree with theoretical predictions within an acceptable margin of error, the Root Sum of the Squares (RSS) error propagation method was implemented. The calculated expanded uncertainty ($\mathbf{U_{calc,h_{0,x}}}$) of conduit heights according to RSS method is as follows:

$$\mathbf{U_{calc,h_{0,x}}} = \sqrt{\left(\frac{\partial \mathbf{h_{0,x}}}{\partial \mathbf{Q}}\boldsymbol{\sigma}_{\mathbf{Q}}\right)^2 + \left(\frac{\partial \mathbf{h_{0,x}}}{\partial \boldsymbol{\mu}}\boldsymbol{\sigma}_{\boldsymbol{\mu}}\right)^2 + \left(\frac{\partial \mathbf{h_{0,x}}}{\partial \mathbf{a}}\boldsymbol{\sigma}_{\mathbf{a}}\right)^2 + \left(\frac{\partial \mathbf{h_{0,x}}}{\partial \mathbf{x}}\boldsymbol{\sigma}_{\mathbf{x}}\right)^2 + \left(\frac{\partial \mathbf{h_{0,x}}}{\partial \boldsymbol{\gamma}}\boldsymbol{\sigma}_{\boldsymbol{\gamma}}\right)^2} \tag{97}$$

Using u-substitution, the partial derivatives above (also known as the sensitivity factors) can be computed as follows:

$$\frac{\partial \mathbf{h_{0,x}}}{\partial \mathbf{Q}} = \frac{\mathbf{26.154\mu ax}}{\mathbf{4\gamma}\left(\frac{\mathbf{26.154Q\mu ax}}{\boldsymbol{\gamma}}\right)^{\frac{3}{4}}} \tag{98}$$

$$\frac{\partial \mathbf{h_{0,x}}}{\partial \boldsymbol{\mu}} = \frac{\mathbf{26.154Qax}}{\mathbf{4\gamma}\left(\frac{\mathbf{26.154Q\mu ax}}{\boldsymbol{\gamma}}\right)^{\frac{3}{4}}} \tag{99}$$

$$\frac{\partial \mathbf{h_{0,x}}}{\partial \boldsymbol{\mu}} = \frac{\mathbf{26.154Qax}}{\mathbf{4\gamma}\left(\frac{\mathbf{26.154Q\mu ax}}{\boldsymbol{\gamma}}\right)^{\frac{3}{4}}} \tag{100}$$

$$\frac{\partial \mathbf{h_{0,x}}}{\partial \mathbf{a}} = \frac{\mathbf{26.154Q\mu x}}{\mathbf{4\gamma}\left(\frac{\mathbf{26.154Q\mu ax}}{\boldsymbol{\gamma}}\right)^{\frac{3}{4}}} \tag{101}$$

$$\frac{\partial h_{0,x}}{\partial x} = \frac{26.154 Q \mu a}{4\gamma \left(\frac{26.154 Q \mu a x}{\gamma}\right)^{\frac{3}{4}}} \quad (102)$$

$$\frac{\partial h_{0,x}}{\partial \gamma} = -\frac{26.154 Q \mu a x}{4\gamma^2 \left(\frac{26.154 Q \mu a x}{\gamma}\right)^{\frac{3}{4}}} \quad (103)$$

The uncertainty of each individual variable ($\boldsymbol{\sigma}$) are determined in the following manner:

1. $\boldsymbol{\sigma_Q}$ is the transducer uncertainty of the Harvard PhD Ultra Syringe Pump and is quoted from the user manual; the pump's flow rate accuracy is $\pm$ 0.25%. [$\boldsymbol{\sigma_Q} = 0.0025\mathbf{Q}$ µL/h]
2. $\boldsymbol{\sigma_\mu}$ is the standard deviation of dynamic viscosities taken from 10 separate solutions of DMEM + 10% FBS measured with a Hydramotion Viscolite 700 portable viscometer. [$\boldsymbol{\sigma_\mu} = 0.05$ mPa·s]
3. $\boldsymbol{\sigma_a}$ is the standard deviation of a conduit's half width along its 25 mm length (i.e., error associated with SIM-printing technique); each conduit's width is measured at 35 distinct locations along its length. [$\boldsymbol{\sigma_a} = 8$ µm]
4. $\boldsymbol{\sigma_x}$ is determined by the microscope's specifications; the microscope (and its analogue coordinate readout) in the *x*-direction is accurate to $\pm$ 1 µm. [$\boldsymbol{\sigma_x} = 1$ µm]
5. $\boldsymbol{\sigma_\gamma}$ is fundamentally unknown since interfacial tension is determined from fitting experimental data to the analytical solution and thus is set to 0; error in interfacial tension is not included.

Finally, error due to experimental uncertainty of direct conduit height measurements via beads ($\mathbf{U_{bead,h_{0,x}}}$) must be included. Experimental uncertainty includes both acquisition error from experimentalist ($\boldsymbol{\sigma_{meas}}$) and two times the diameter of the beads used for height measurements ($2\mathbf{d_{bead}}$):

$$\mathbf{U_{meas,h_0,x}} = \sqrt{\boldsymbol{\sigma}_{\mathbf{bead}}^2 + 2\mathbf{d}_{\mathbf{bead}}^2} \quad (104)$$

To measure acquisition error, the distance between a single pair of beads (one on the surface of the Petri dish and the other imbedded in a conduit's media-fluorocarbon interface) were

measured 15 times and a standard deviation between subsequent tests was calculated ($\boldsymbol{\sigma_{meas}} =$ 0.9 μm). Unlike the calculated expanded sensitivity $\mathbf{U_{calc,h_{0,x}}}$ which is dependent on location along a conduit's length (i.e., expected error increases as distance from a conduit's exit increases), $\mathbf{U_{meas,h_{0,x}}}$ is applied along the entirety of the conduit's length such that the total propagated error is:

$$\mathbf{U_{tot}} = \sqrt{\mathbf{U^2_{calc,h_{0,x}}} + \mathbf{U^2_{meas,h_{0,x}}}} \tag{105}$$

Additional error can be attributed to the microscope's focal length, which can distort a bead's location in the *z*-direction while taking measurements. This error becomes more apparent for conduits with smaller height profiles such as the 6.25 μL/h test below; the microscope's focal length (a fixed constant throughout all tests) has a more significant percent error for smaller conduits and can thus lead to more outliers in a given data set.

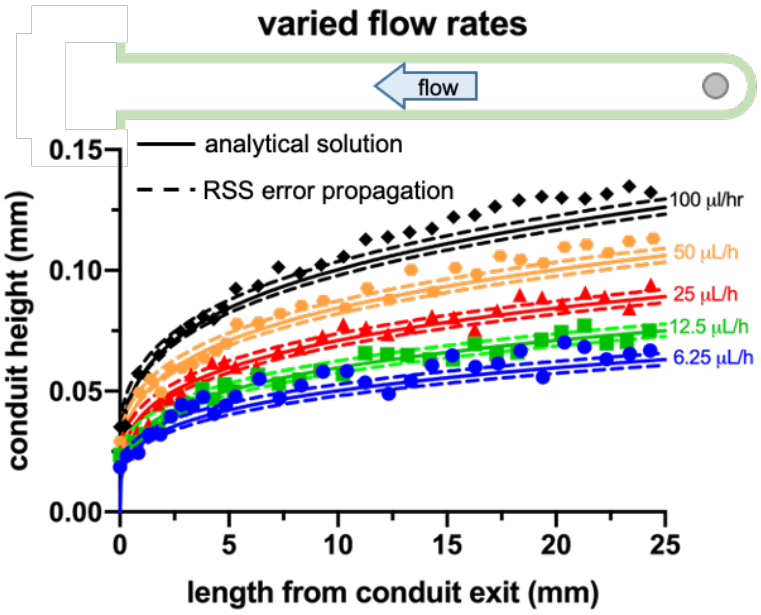

Figure 25. Height measurements of a 30 mm long conduit ($\mathbf{a} = 0.325$ mm) flowing at varying volumetric flow rates (same data displayed in Figure 18) overlayed with predictions from the analytical solution from Equation 42 (bold curves). Dotted curves above and below each bold prediction curve represent the total propagated error ($\mathbf{U_{tot}}$) associated with experimental data acquisition.

Passive Pumping Conduits

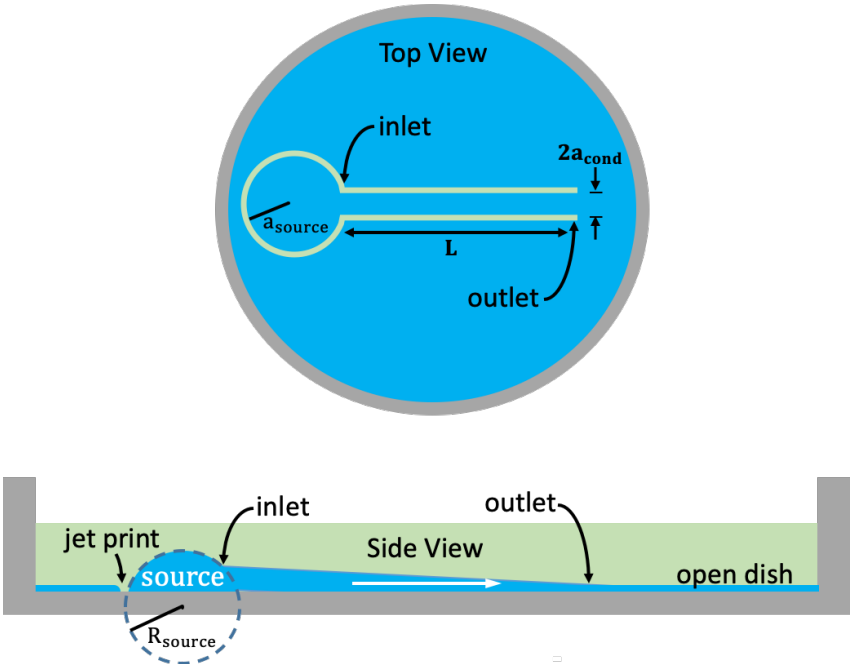

Figure 26. Top and side view of passive pumping conduit connecting circular droplet (source) to open wetted dish surface (sink). A droplet of circular footprint $\mathbf{a_{source}}$ can be filled with media to create a pressure gradient between the source $\left(\mathbf{P_{L,source}} = \frac{\gamma}{\mathbf{R_{source}}}\right)$ and the sink ($\mathbf{P_{L,sink}} \approx 0$) to drive flow.

Flow physics of passive pumping systems (Figure 26) are more difficult to accurately characterize compared to active pumping theory (Chapter 4.3) since volumetric flow rate (**Q**) through a passively pumped conduit is no longer a user-defined constant[26], [27], [68]. Instead, media is pumped from a source droplet to an open dish at a decelerating rate until the source and the open dish have equal Laplace pressure (and thus radii of curvatures). When $\mathbf{R_{source}} = \mathbf{R_{dish}} \approx \infty$, the system reaches equilibrium and remains static until external agitation (i.e., more volume is added to the source to reintroduce a pressure gradient). The following assumption can be made at the inlet and exit of the conduit which connects the source and the rest of the open dish:

$$\mathbf{P_{source}} = \frac{\mathbf{2\gamma}}{\mathbf{R_{source}}} \approx \mathbf{P_{in}} \tag{106}$$

$$\mathbf{P_{dish}} = \frac{\mathbf{2\gamma}}{\mathbf{R_{dish}}} \approx \mathbf{0} \tag{107}$$

Recall the analytically derived equation for pressure drop ($\mathbf{P_x}$) along the length of a flexible walled conduit:

$$\mathbf{P_x} = \left(\frac{\mathbf{418.464Q\mu\gamma^3 x}}{\mathbf{a_c^7}} + \mathbf{P_0^4}\right)^{\mathbf{0.25}} \tag{108}$$

Assuming the Laplace pressure in the dish is zero and the conduit is of a known length **L**, the governing equation above can be written as follows in terms of the source droplet's radii of curvature:

$$\frac{\mathbf{2\gamma}}{\mathbf{R_{source}}(t)} = \left(\frac{\mathbf{418.464Q}(t)\mathbf{\mu\gamma^3 L}}{\mathbf{a_{cond}^7}}\right)^{\mathbf{0.25}} \tag{109}$$

Notice for passive pumping systems, the source's radius of curvature $\mathbf{R_{source}}(t)$ and the volumetric flow rate $\mathbf{Q}(t)$ are functions of time. Solving for $\mathbf{Q}(t)$ we get the following solution:

$$\mathbf{Q}(t) = \frac{\mathbf{16a_{cond}^7\gamma}}{\mathbf{418.464\mu L}}\left(\frac{\mathbf{1}}{\mathbf{R_{source}}(t)^{\mathbf{4}}}\right) \tag{110}$$

Volumetric flow rate $\mathbf{Q}(t)$ passively pumped through the conduit is simply the rate of change of the sink's volume ($\mathbf{V_{source}}$) with respect to time (t):

$$\mathbf{Q}(t) = -\frac{\mathrm{d}\mathbf{V_{source}}}{\mathrm{d}t} \tag{111}$$

where the volume of the cap of a sphere in terms of the source droplet's maximum height $\mathbf{h_{source}}(t)$ and footprint's half width $\mathbf{a_{source}}$ is as follows:

$$\mathbf{V_{source}} = \frac{\boldsymbol{\pi}\mathbf{h_{source}}(t)}{\mathbf{6}}(\mathbf{3a_{source}^2} + \mathbf{h_{source}}(t)^{\mathbf{2}}) \tag{112}$$

Thus, the following relationship can be deduced regarding the system's volumetric flow rate:

$$\frac{\mathrm{d}\mathbf{V_{source}}}{\mathrm{d}t} = \frac{\boldsymbol{\pi}}{\mathbf{2}}\frac{\mathrm{d}\mathbf{h_{source}}}{\mathrm{d}t}(\mathbf{a_{source}^2} + \mathbf{h_{source}}(t)^{\mathbf{2}}) \tag{113}$$

$$\mathbf{Q}(t) = -\frac{\boldsymbol{\pi}}{\mathbf{2}}\frac{\mathrm{d}\mathbf{h_{source}}}{\mathrm{d}t}(\mathbf{a_{source}^2} + \mathbf{h_{source}}(t)^{\mathbf{2}}) \tag{114}$$

Recall the radii of curvature of the spherical source can also be written in terms of the source's height and half width:

$$\mathbf{R_{source}}(t) = \frac{\mathbf{h}(t)_{\mathbf{source}}{}^{\mathbf{2}} + \mathbf{a_{source}^2}}{\mathbf{2h}(t)_{\mathbf{source}}} \tag{115}$$

Plugging both the relationships derived for volumetric flow rate and the source's radii of curvature into the highlighted governing equation we are left with the following solution:

$$-\frac{\boldsymbol{\pi}}{\mathbf{2}}\frac{\mathrm{d}\mathbf{h_{source}}}{\mathrm{d}t}(\mathbf{a_{source}^2} + \mathbf{h_{source}^2}) = \frac{\mathbf{16a_{cond}^7}\boldsymbol{\gamma}}{\mathbf{418.464\mu L}}\left(\frac{\mathbf{16h_{source}^4}}{(\mathbf{h_{source}^2} + \mathbf{a_{source}^2})^{\mathbf{4}}}\right) \tag{116}$$

$$\frac{\mathrm{d}\mathbf{h_{source}}}{\mathrm{d}t} = -\frac{\mathbf{1.224a_{cond}^7}\boldsymbol{\gamma}}{\boldsymbol{\pi}\boldsymbol{\mu}\mathbf{L}}\left(\frac{\mathbf{h_{source}^4}}{(\mathbf{h_{source}^2} + \mathbf{a_{source}^2})^{\mathbf{5}}}\right) \tag{117}$$

Equation 117 expresses the change of source droplet height with respect to time. This differential equation, however, cannot be solved analytically. Instead, a numerical approach can be applied if the source droplet's height at $t = 0$ is known ($\mathbf{h_{source,0}}$)**.** The change in source droplet height over an infinitesimally small time period ($t = \mathrm{d}t$) can be calculated as follows:

$$\mathbf{h_{source,1}} = \frac{\mathrm{d}\mathbf{h_{source,0}}}{\mathrm{d}t}\,\mathrm{d}t \tag{118}$$

At $t = \mathrm{d}t$, the rate of change of source height $\left(\frac{\mathbf{dh_{source,1}}}{\mathrm{d}t}\right)$ can be solver for by plugging in $\mathbf{h_{source}} = \mathbf{h_{source,1}}$ into Equation 117**.** Equation 117-118 can be iterated in the following way until $\frac{\mathbf{dh_{source,n}}}{\mathrm{d}t} = \mathbf{0}$, at which point the source droplet is no longer pumping fluid through the conduit.

$$\frac{\mathrm{d}\mathbf{h_{source,n}}}{\mathrm{d}t} = -\frac{\mathbf{1.224a_{cond}^{7}\gamma}}{\boldsymbol{\pi\mu L}}\left(\frac{\mathbf{h_{source,n}^{4}}}{\left(\mathbf{h_{source,n}^{2}} + \mathbf{a_{source}^{2}}\right)^{5}}\right) \tag{119}$$

$$\mathbf{h_{source,n+1}} = \frac{\mathrm{d}\mathbf{h_{source,n}}}{\mathrm{d}t}\,\mathrm{d}t \tag{120}$$

Appendix 2: Supplemental Experiments

Dish Wetting Thickness

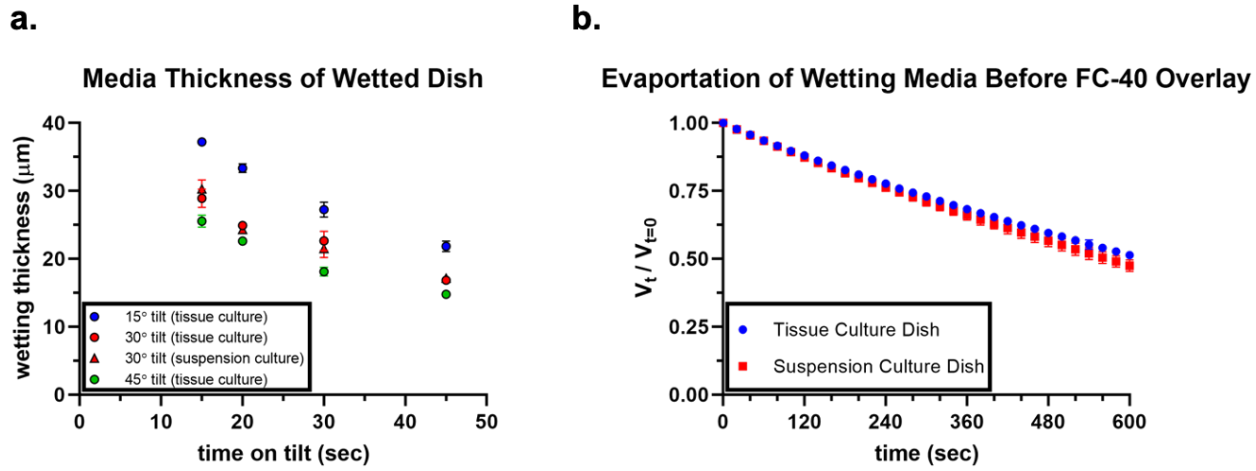

Figure 27. Average DMEM + 10% FBS wetting thickness while preparing 6 cm Petri dishes for SIM-printing (see Chapter 5.1.1 for full dish preparation procedure). Measurements are made using an electronic scale by first weighing virgin Petri dishes, and then weighing the dish after various tilts. Wetting thickness is calculated assuming the surface of each Petri dish is perfectly flat. Each datum above is averaged between 5 subsequent tests; standard deviations between tests is represented by error bars. **a.** Wetting thickness decreases with increased dish tilt angle and increased time media is extracted from dish. Using Petri dishes with different surface treatments (i.e., tissue culture or suspension culture dishes) has little effect regarding average wetting thicknesses. **b.** Before 1 mL of FC-40 is deposited on top of the thin layer of dish-wetting DMEM + 10% FBS in a Petri dish, media evaporates. Again, little difference between dishes with different surface treatments is experienced. Once media is over-laid with FC-40, evaporation on dish preparation time scale (i.e, seconds) is insignificant (see Figure 28).

Test Matrix for SIM-Printing Resolution Experiments

Due to the size constraint of 6 cm Petri dishes, SIM-printing resolution capability experiments had to be conducted in regimes. Each individual parameter below was tested three times in a single dish, and each regime was repeated three times, providing for a total of nine distinct measurements for each datum point below; standard deviations between subsequent tests are represented by the error bars in Figure 15.

Table 3

Arm Speed Regime	**Traverse Arm Velocity (mm/s)**
1	0.5, 1, 2, 3, 4
2	5, 6, 7, 8, 9
3	10, 15, 20, 25, 30, 35, 40
Flow Rate Regime	**Volumetric Flow Rate (µL/s)**
1	6, 7, 8, 9, 10, 11, 12
2	13, 14, 15, 16, 17
3	18, 19, 20
Jet Height Regime	**Jet Height Above Substrate (mm)**
1	0.2, 0.3, 0.4, 0.5
2	0.6, 0.7, 0.8, 1.0

Media Evaporation in SIM-Printed Devices

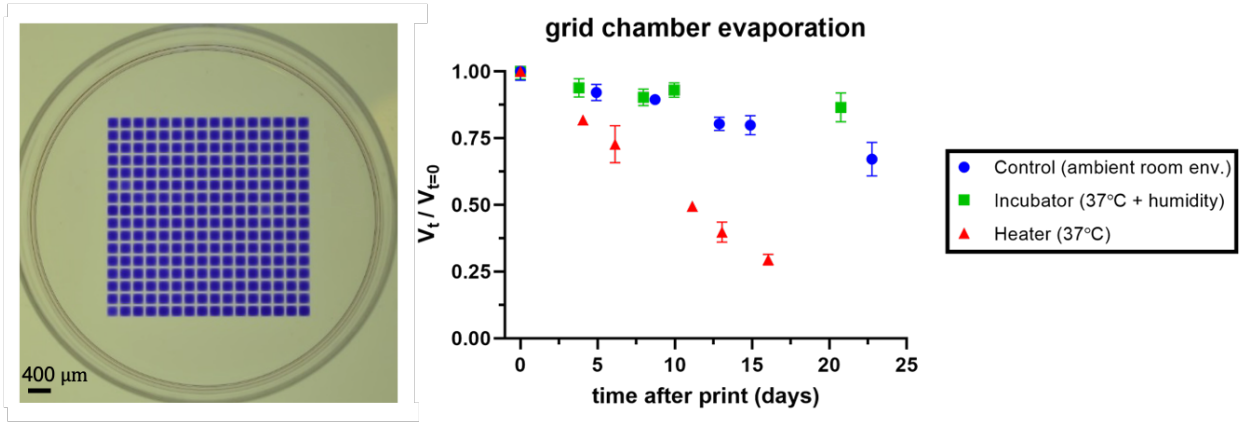

Figure 28. SIM-printed 16x16 cell assay grid of DMEM + 10% FBS (1.9 mm distance between the centres of adjacent square chambers) covered by 1 mL of FC-40. Blue dye was added to grid (left) only to increase visibility; no dye was added to experiments in plot (right). For experiments, all chambers in 3 different SIM-printed 16x16 grids are initially infused to a total volume of 0.9 µL of DMEM + 10% FBS and placed in different environments. One dish is places in an incubator, one is placed in a heater, and the last is left on a lab bench in ambient conditions. At each time interval in the plot, the volume from 5 chambers in each of the three environments are measured and averaged; the error bars above represent the standard deviation between neighboring chambers in the same dish.

SIM-Printed Wall Widths of Common Media Solutions

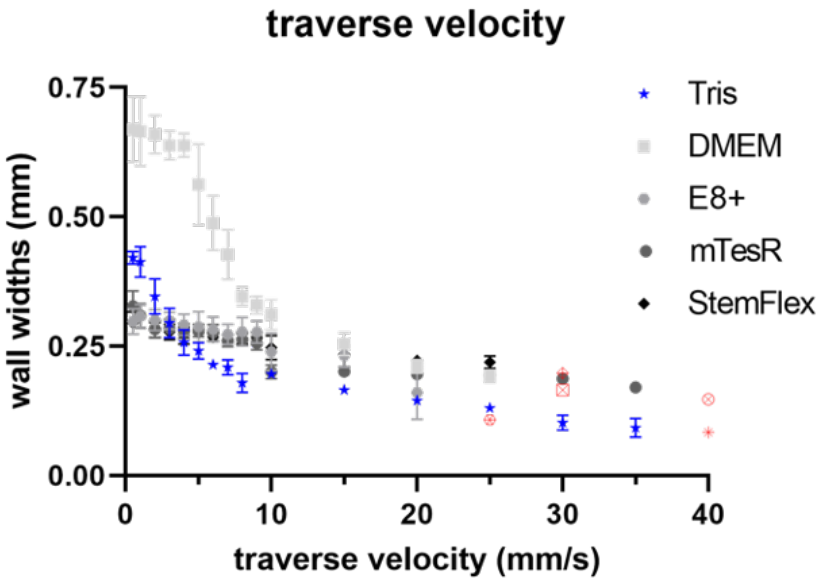

Figure 29. Widths of fluid FC-40 walls created by SIM-printing over a range of traverse velocities. Various media solutions commonly used in cell biology, as well as a blue dye solution (not suitable for cell culture) are compared. Walls were printed with a 70 µm jet whose volumetric flow rate and height above dish were 10 µL/s and 0.5 mm respectively. For each wetting solution, increasing the jet's traversing velocity decreases widths and each solution experience print-failure by $\mathbf{V_{jet}} = 40$ mm/s.

Petri Dish Surface Curvature

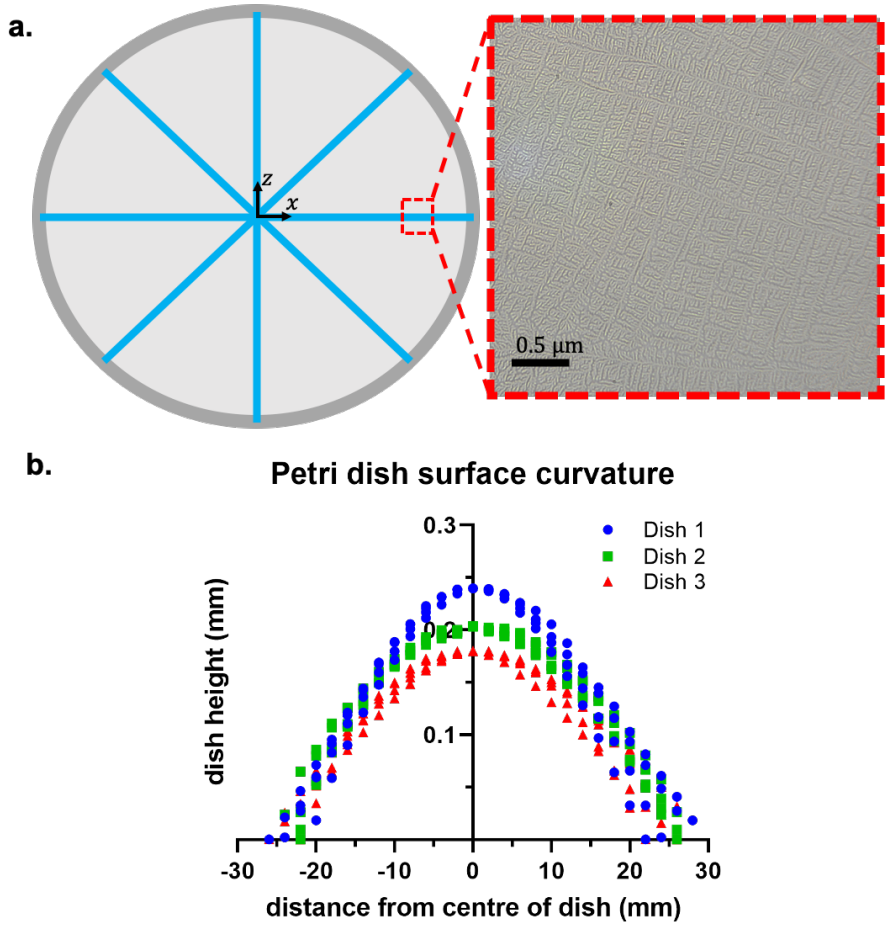

Figure 30. Petri dish surface concavity. **a.** To measure Petri dish surface curvature, four lines of DMEM + 10% FBS were infused across tissue culture Petri dishes through their centre points (left) and then let dry. The dried DMEM + 10% FBS crystalizes into a thin layer (right) which follows the dish's curvature. Focusing on the crystalized media with a microscope and recording the *z* coordinate results in accurate curvature measurements. **b.** Measurements from three different tissue culture Petri dishes show the variation between dish surface geometry.

Conduit Flows Over Time and with Various Fluids

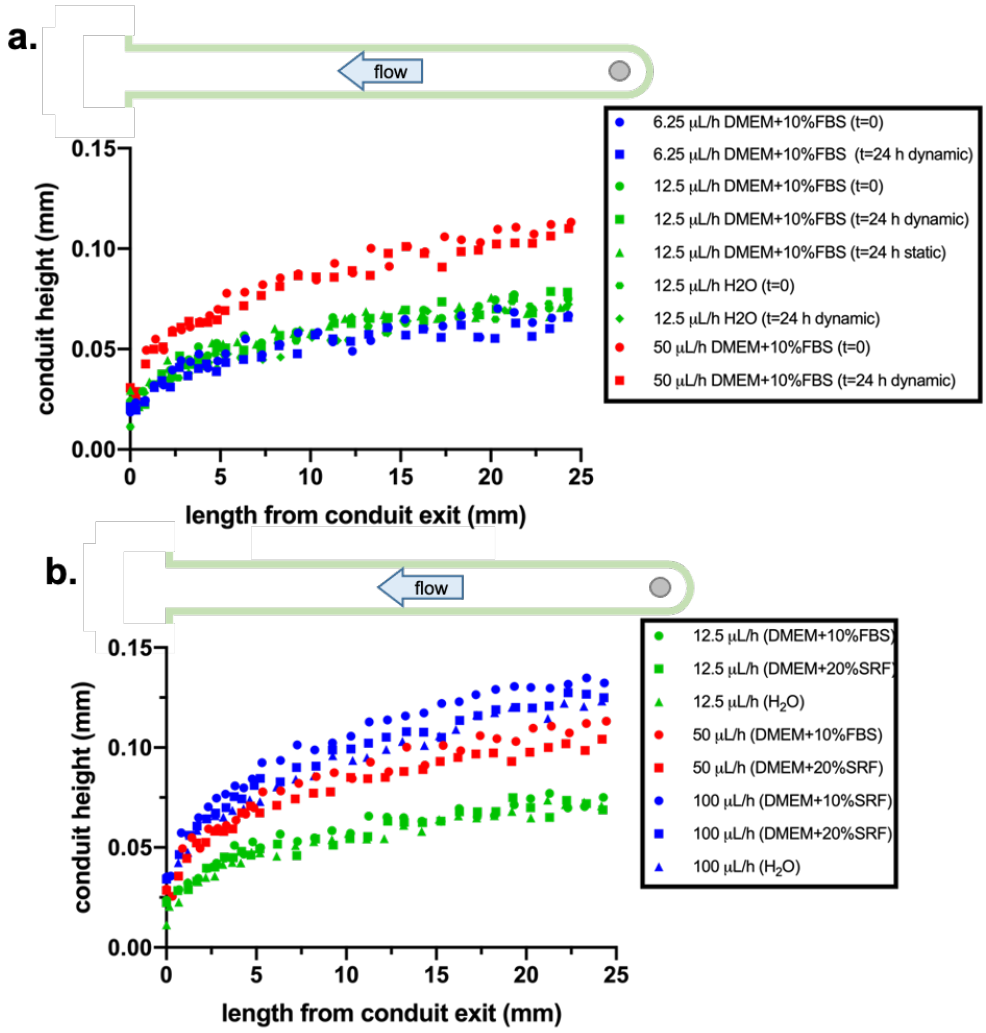

Figure 31. The effect of flow on the centre height, $\mathbf{h_0}$, along the length of an open-ended conduit with flexible walls. 30 mm long conduits were SIM-printed using DMEM + 10% FBS in 6 cm Petri dishes. Infusing needles were inserted at the closed end of the conduit and DMEM + 10% FBS with fluorescent 0.5 µm diameter beads solution was actively pumped via an external syringe pump. Top: schematic of conduit. Bottom: in plots, symbols represent measured heights. **a.** Conduits that were actively pumped for 24 h, or left static for 24 h and then pumped until steady state, show negligible changes in centre heights from original measurements at $t = 0$. **b.** Fluids of similar densities pumped at equal flow rates produce similar conduit height profiles.

Bibliography

[1] G. M. Whitesides, "The origins and the future of microfluidics," *Nature*, vol. 442, no. 7101, pp. 368–373, Jul. 2006, doi: 10.1038/nature05058.

[2] N. Convery and N. Gadegaard, "30 years of microfluidics," *Micro and Nano Engineering*, vol. 2, pp. 76–91, Mar. 2019, doi: 10.1016/j.mne.2019.01.003.

[3] G. Luka *et al.*, "Microfluidics Integrated Biosensors: A Leading Technology towards Lab-on-a-Chip and Sensing Applications," *Sensors*, vol. 15, no. 12, pp. 30011–30031, Dec. 2015, doi: 10.3390/s151229783.

[4] S. Wang, Y. Yin, C. Hu, and P. Rezai, "3D Integrated Circuit Cooling with Microfluidics," *Micromachines*, vol. 9, no. 6, p. 287, Jun. 2018, doi: 10.3390/mi9060287.

[5] K. M. Horsman, J. M. Bienvenue, K. R. Blasier, and J. P. Landers, "Forensic DNA Analysis on Microfluidic Devices: A Review," *Journal of Forensic Sciences*, vol. 52, no. 4, pp. 784–799, Jul. 2007, doi: 10.1111/j.1556-4029.2007.00468.x.

[6] E. K. Sackmann, A. L. Fulton, and D. J. Beebe, "The present and future role of microfluidics in biomedical research," *Nature*, vol. 507, no. 7491, pp. 181–189, Mar. 2014, doi: 10.1038/nature13118.

[7] M. D. Tarn and N. Pamme, *Reference Module in Chemistry, Molecular Sciences and Engineering*. Elsevier, 2014.

[8] R. G. Sweet, "High Frequency Recording with Electrostatically Deflected Ink Jets," *Review of Scientific Instruments*, vol. 36, no. 2, pp. 131–136, Feb. 1965, doi: 10.1063/1.1719502.

[9] Lord Rayleigh, "VI. On the capillary phenomena of jets," *Proceedings of the Royal Society of London*, vol. 29, no. 196–199, pp. 71–97, Dec. 1879, doi: 10.1098/rspl.1879.0015.

[10] J. Eggers and E. Villermaux, "Physics of liquid jets," *Reports on Progress in Physics*, vol. 71, no. 3, p. 036601, Mar. 2008, doi: 10.1088/0034-4885/71/3/036601.

[11] A. Manz, N. Graber, and H. M. Widmer, "Miniaturized total chemical analysis systems: A novel concept for chemical sensing," *Sensors and Actuators B: Chemical*, vol. 1, no. 1–6, pp. 244–248, Jan. 1990, doi: 10.1016/0925-4005(90)80209-I.

[12] Y. Xia and G. M. Whitesides, "Soft Lithography," *Annual Review of Materials Science*, vol. 28, no. 1, pp. 153–184, Aug. 1998, doi: 10.1146/annurev.matsci.28.1.153.

[13] J. El-Ali, P. K. Sorger, and K. F. Jensen, "Cells on chips," *Nature*, vol. 442, no. 7101, pp. 403–411, Jul. 2006, doi: 10.1038/nature05063.

[14] S. Torino, B. Corrado, M. Iodice, and G. Coppola, "PDMS-Based Microfluidic Devices for Cell Culture," *Inventions*, vol. 3, no. 3, p. 65, Sep. 2018, doi: 10.3390/inventions3030065.

[15] C.-P. Segeritz and L. Vallier, *Basic Science Methods for Clinical Researchers*. Elsevier, 2017.

[16] H. Kimura, T. Yamamoto, H. Sakai, Y. Sakai, and T. Fujii, "An integrated microfluidic system for long-term perfusion culture and on-line monitoring of intestinal tissue models," *Lab on a Chip*, vol. 8, no. 5, p. 741, 2008, doi: 10.1039/b717091b.

[17] D. Huh, B. D. Matthews, A. Mammoto, M. Montoya-Zavala, H. Y. Hsin, and D. E. Ingber, "Reconstituting Organ-Level Lung Functions on a Chip," *Science*, vol. 328, no. 5986, pp. 1662–1668, Jun. 2010, doi: 10.1126/science.1188302.

[18] K.-J. Jang and K.-Y. Suh, “A multi-layer microfluidic device for efficient culture and analysis of renal tubular cells,” *Lab Chip*, vol. 10, no. 1, pp. 36–42, 2010, doi: 10.1039/B907515A.
[19] M. Tsai *et al.*, “In vitro modeling of the microvascular occlusion and thrombosis that occur in hematologic diseases using microfluidic technology,” *Journal of Clinical Investigation*, vol. 122, no. 1, pp. 408–418, Jan. 2012, doi: 10.1172/JCI58753.
[20] U. Marx *et al.*, “‘Human-on-a-chip’ Developments: A Translational Cutting-edge Alternative to Systemic Safety Assessment and Efficiency Evaluation of Substances in Laboratory Animals and Man?,” *Alternatives to Laboratory Animals*, vol. 40, no. 5, pp. 235–257, Oct. 2012, doi: 10.1177/026119291204000504.
[21] D. Huh, G. A. Hamilton, and D. E. Ingber, “From 3D cell culture to organs-on-chips,” *Trends in Cell Biology*, vol. 21, no. 12, pp. 745–754, Dec. 2011, doi: 10.1016/j.tcb.2011.09.005.
[22] E. Berthier, E. W. K. Young, and D. Beebe, “Engineers are from PDMS-land, Biologists are from Polystyrenia,” *Lab on a Chip*, vol. 12, no. 7, p. 1224, 2012, doi: 10.1039/c2lc20982a.
[23] K. J. Regehr *et al.*, “Biological implications of polydimethylsiloxane-based microfluidic cell culture,” *Lab on a Chip*, vol. 9, no. 15, p. 2132, 2009, doi: 10.1039/b903043c.
[24] Y. S. Heo *et al.*, “Characterization and Resolution of Evaporation-Mediated Osmolality Shifts That Constrain Microfluidic Cell Culture in Poly(dimethylsiloxane) Devices,” *Analytical Chemistry*, vol. 79, no. 3, pp. 1126–1134, Feb. 2007, doi: 10.1021/ac061990v.
[25] J. Berthier, K. A. Brakke, and E. Berthier, *Open Microfluidics*. Wiley, 2016.
[26] C. Li *et al.*, “Under oil open-channel microfluidics empowered by exclusive liquid repellency,” *Science Advances*, vol. 6, no. 16, p. eaay9919, Apr. 2020, doi: 10.1126/sciadv.aay9919.
[27] E. J. Walsh *et al.*, “Microfluidics with fluid walls,” *Nature Communications*, vol. 8, no. 1, p. 816, Dec. 2017, doi: 10.1038/s41467-017-00846-4.
[28] C. Soitu *et al.*, “Microfluidic chambers using fluid walls for cell biology,” *Proceedings of the National Academy of Sciences*, vol. 115, no. 26, pp. E5926–E5933, Jun. 2018, doi: 10.1073/pnas.1805449115.
[29] A. J. Robinson and E. Schnitzler, “An experimental investigation of free and submerged miniature liquid jet array impingement heat transfer,” *Experimental Thermal and Fluid Science*, vol. 32, no. 1, pp. 1–13, Oct. 2007, doi: 10.1016/j.expthermflusci.2006.12.006.
[30] D. Burfoot and K. Middleton, “Effects of operating conditions of high pressure washing on the removal of biofilms from stainless steel surfaces,” *Journal of Food Engineering*, vol. 90, no. 3, pp. 350–357, Feb. 2009, doi: 10.1016/j.jfoodeng.2008.07.006.
[31] J. Lu, C. M. Corvalan, and J. Huang, “Deformation and removal of viscous thin film by submerged jet impingement,” *AIChE Journal*, vol. 66, no. 1, Jan. 2020, doi: 10.1002/aic.16745.
[32] C. W. Visser, M. V. Gielen, Z. Hao, S. Le Gac, D. Lohse, and C. Sun, “Quantifying Cell Adhesion through Impingement of a Controlled Microjet,” *Biophysical Journal*, vol. 108, no. 1, pp. 23–31, Jan. 2015, doi: 10.1016/j.bpj.2014.10.071.
[33] M. Bieber, R. Kneer, and W. Rohlfs, “Self-similarity of heat transfer characteristics in laminar submerged and free-surface slot jet impingement,” *International Journal of Heat and Mass Transfer*, vol. 104, pp. 1341–1352, Jan. 2017, doi: 10.1016/j.ijheatmasstransfer.2016.08.104.

[34] B. R. Munson, T. H. Okiishi, W. W. Huebsch, and A. P. Rothmayer, *Fundamentals of Fluid Mechanics*, 7th ed. John Wiley & Sons, Inc., 2013.
[35] M. D. Deshpande and R. N. Vaishnav, "Submerged laminar jet impingement on a plane," *Journal of Fluid Mechanics*, vol. 114, no. 1, p. 213, Jan. 1982, doi: 10.1017/S0022112082000111.
[36] J. H. Lienhard and J. H. Lienhard, "Velocity Coefficients For Free Jets From Sharp-Edged Orifices," *Journal of Fluids Engineering*, vol. 106, no. 1, pp. 13–17, Mar. 1984, doi: 10.1115/1.3242391.
[37] B. Kashi, E. Weinberg, and H. D. Haustein, "Analytical re-examination of the submerged laminar jet's velocity evolution," *Physics of Fluids*, vol. 30, no. 6, p. 063604, Jun. 2018, doi: 10.1063/1.5028560.
[38] H. W. Glover, T. Brass, R. K. Bhagat, J. F. Davidson, L. Pratt, and D. I. Wilson, "Cleaning of complex soil layers on vertical walls by fixed and moving impinging liquid jets," *Journal of Food Engineering*, vol. 178, pp. 95–109, Jun. 2016, doi: 10.1016/j.jfoodeng.2015.12.021.
[39] A. Yeckel and S. Middleman, "Removal of a viscous film from a rigid plan surface by an impinging liquid jet," *Chemical Engineering Communications*, vol. 50, no. 1–6, pp. 165–175, Feb. 1987, doi: 10.1080/00986448708911823.
[40] A. Yeckel, L. Strong, and S. Middleman, "Viscous film flow in the stagnation region of the jet impinging on planar surface," *AIChE Journal*, vol. 40, no. 10, pp. 1611–1617, Oct. 1994, doi: 10.1002/aic.690401003.
[41] S. Kesavan, "The Isoperimetric inequality," *Resonance*, vol. 7, no. 9, pp. 8–18, Sep. 2002, doi: 10.1007/BF02836181.
[42] R. H. Sabersky and A. J. Acosta, *Fluid Flow, A First Course in Fluid Mechanics*, 4th ed. 2001.
[43] J. Berthier and K. A. Brakke, *The Physics of Microdroplets*. Hoboken, NJ, USA: John Wiley & Sons, Inc., 2012.
[44] M. J. Rosen and J. T. Kunjappu, *Surfactants and Interfacial Phenomena*. Hoboken, NJ, USA: John Wiley & Sons, Inc., 2012.
[45] J.-C. Baret, "Surfactants in droplet-based microfluidics," *Lab Chip*, vol. 12, no. 3, pp. 422–433, 2012, doi: 10.1039/C1LC20582J.
[46] L. Wilhelmy, "Ueber die Abhängigkeit der Capillaritäts-Constanten des Alkohols von Substanz und Gestalt des benetzten festen Körpers," *Annalen der Physik und Chemie*, vol. 195, no. 6, pp. 177–217, 1863, doi: 10.1002/andp.18631950602.
[47] P. L. du Noüy, "A new apparatus for measuring surface tension," *Journal of General Physiology*, vol. 1, no. 5, pp. 521–524, May 1919, doi: 10.1085/jgp.1.5.521.
[48] S. Sugden, "The determination of surface tension from the maximum pressure in bubbles," *J. Chem. Soc., Trans.*, vol. 121, pp. 858–866, 1922, doi: 10.1039/CT9222100858.
[49] C. A. MacLeod and C. J. Radke, "A growing-drop technique for measuring dynamic interfacial tension," Oct. 1993. doi: 10.2172/10192749.
[50] Lord Rayleigh, "On the theory of the capillary tube," *Proceedings of the Royal Society of London. Series A, Containing Papers of a Mathematical and Physical Character*, vol. 92, no. 637, pp. 184–195, Jan. 1916, doi: 10.1098/rspa.1916.0004.

[51] T. Tate, “On the magnitude of a drop of liquid formed under different circumstances,” *The London, Edinburgh, and Dublin Philosophical Magazine and Journal of Science*, vol. 27, no. 181, pp. 176–180, Mar. 1864, doi: 10.1080/14786446408643645.
[52] J. D. Berry, M. J. Neeson, R. R. Dagastine, D. Y. C. Chan, and R. F. Tabor, “Measurement of surface and interfacial tension using pendant drop tensiometry,” *Journal of Colloid and Interface Science*, vol. 454, pp. 226–237, Sep. 2015, doi: 10.1016/j.jcis.2015.05.012.
[53] J. F. Padday and A. R. Pitt, “Surface and interfacial tensions from the profile of a sessile drop,” *Proceedings of the Royal Society of London. A. Mathematical and Physical Sciences*, vol. 329, no. 1579, pp. 421–431, Sep. 1972, doi: 10.1098/rspa.1972.0121.
[54] J. Drelich, C. Fang, and C. L. White, *Encyclopedia of Surface and Colloid Science*. New york: Marcel Dekker Inc., 2002.
[55] C. Gianino, “Measurement of surface tension by the dripping from a needle,” *Physics Education*, vol. 41, no. 5, pp. 440–444, Sep. 2006, doi: 10.1088/0031-9120/41/5/010.
[56] P. Day, A. Manz, and Y. Zhang, *Microdroplet Technology: Principles and Emerging Applications in Biology and Chemistry*. New York: Springer-Verlag , 2012.
[57] L. Mazutis and A. D. Griffiths, “Selective droplet coalescence using microfluidic systems,” *Lab on a Chip*, vol. 12, no. 10, pp. 1800–1806, 2012, doi: 10.1039/c2lc40121e.
[58] E. Bormashenko, R. Pogreb, G. Whyman, and A. Musin, “Surface tension of liquid marbles,” *Colloids and Surfaces A: Physicochemical and Engineering Aspects*, vol. 351, no. 1–3, pp. 78–82, Nov. 2009, doi: 10.1016/j.colsurfa.2009.09.027.
[59] J. Hegemann *et al.*, “Pendant capsule elastometry,” *Journal of Colloid and Interface Science*, vol. 513, pp. 549–565, Mar. 2018, doi: 10.1016/j.jcis.2017.11.048.
[60] R. Wang and X. Li, “On the effective surface tension of powder-derived liquid marbles,” *Powder Technology*, vol. 367, pp. 608–615, May 2020, doi: 10.1016/j.powtec.2020.04.028.
[61] D. Carvajal, E. J. Laprade, K. J. Henderson, and K. R. Shull, “Mechanics of pendant drops and axisymmetric membranes,” *Soft Matter*, vol. 7, no. 22, pp. 10508–10519, 2011, doi: 10.1039/c1sm05703k.
[62] S. Knoche *et al.*, “Elastometry of Deflated Capsules: Elastic Moduli from Shape and Wrinkle Analysis,” *Langmuir*, vol. 29, no. 40, pp. 12463–12471, Oct. 2013, doi: 10.1021/la402322g.
[63] O. Yu. Milyaeva *et al.*, “Dynamic Surface Properties of Mixed Dispersions of Silica Nanoparticles and Lysozyme,” *The Journal of Physical Chemistry B*, vol. 123, no. 22, pp. 4803–4812, Jun. 2019, doi: 10.1021/acs.jpcb.9b03352.
[64] J. Shemesh, I. Jalilian, A. Shi, G. Heng Yeoh, M. L. Knothe Tate, and M. Ebrahimi Warkiani, “Flow-induced stress on adherent cells in microfluidic devices,” *Lab on a Chip*, vol. 15, no. 21, pp. 4114–4127, 2015, doi: 10.1039/C5LC00633C.
[65] S. Varma and J. Voldman, “A cell-based sensor of fluid shear stress for microfluidics,” *Lab on a Chip*, vol. 15, no. 6, pp. 1563–1573, 2015, doi: 10.1039/C4LC01369G.
[66] J.-J. Chiu and S. Chien, “Effects of Disturbed Flow on Vascular Endothelium: Pathophysiological Basis and Clinical Perspectives,” *Physiological Reviews*, vol. 91, no. 1, pp. 327–387, Jan. 2011, doi: 10.1152/physrev.00047.2009.
[67] R. L. Speth and E. Lauga, “Capillary instability on a hydrophilic stripe,” *New Journal of Physics*, vol. 11, no. 7, p. 075024, Jul. 2009, doi: 10.1088/1367-2630/11/7/075024.

[68] M. Hermann, K. Bachus, G. T. T. Gibson, and R. D. Oleschuk, “Open sessile droplet viscometer with low sample consumption,” *Lab on a Chip*, vol. 20, no. 10, pp. 1869–1876, 2020, doi: 10.1039/D0LC00248H.